# Gold and molybdenum metallogeny in the Xiaoqinling region of central China

**Doctoral Thesis**

**(Dissertation)**

to be awarded the degree of

*Doctor rerum naturalium* (Dr. rer. nat.)

submitted by

**Wei Jian**

from Sichuan, China

approved by the Faculty of Energy and Management Science,

Clausthal University of Technology

Date of oral examination

(15, July, 2015)

**Chairperson of the Board of Examiners:** Prof. Dr. Hans-Jürgen Gursky

**Chief Reviewer:** Prof. Dr. Bernd Lehmann

**Reviewer:** Prof. Dr. Kurt Mengel

This dissertation was undertaken at the Mineral Resources Department of the Institute of Disposal Research of the Clausthal University of Technology.

# Abstract

The Qinling-Dabie Orogenic belt in central China is a major gold and molybdenum province. This thesis gives an account of the mineralogy and geochemistry of two typical ore deposits in the Xiaoqinling region of this belt, i.e., the Dahu Au-Mo deposit and the Yangzhaiyu Au deposit.

The quartz-vein style Dahu Au-Mo deposit has proven reserves of 31 t gold (grade: 4.7 g/t Au) and 30,000 t molybdenum (grade: 0.13% Mo), with an annual gold production of about 300 kg and molybdenum production of about 900 t. The Dahu Au-Mo deposit formed in four stages, i.e., an early quartz–K-feldspar stage (I), a pyrite–molybdenite stage (II), a sulfide–telluride–sulfosalt–gold stage (III), and a late carbonate–barite stage (IV). Abundant tellurides and sulfosalts occur in stage III: altaite, tellurobismuthite, buckhornite, hessite, petzite, calaverite, aikinite, kupcikite, lindstromite, salzburgite, wittichenite, and tetradymite. The system is characterized by carbono-aqueous fluids of low to moderate salinity and high oxygen fugacity. Total homogenization temperatures of the $H_2O$-$CO_2$ fluid inclusions in stage I and stage III quartz range from 230 to 440 ℃ and 198 to 320 ℃, respectively. The variation in $CO_2/H_2O$ ratios and microthermometric data of the $H_2O$-$CO_2$ fluid inclusions results from a combination of fluid unmixing and sequential trapping of fluid inclusions, but also from post-entrapment re-equilibration. UV-fs-LA-ICP-MS analysis of $H_2O$-$CO_2$ fluid inclusions reveals that the concentrations of Mo are always below the detection limit of between 0.1 and 1 ppm, while the concentrations of Au are also below the detection limit of between 0.2 and 2 ppm except one fluid inclusion with a suspicious gold concentration value of 1 ppm. Lower detection limits are required to accurately measure the concentrations of Au and Mo in fluid inclusions. Trace element concentrations in the ore fluids of the Dahu deposit are clearly different from those of metamorphic fluids, but show close affinities to ore fluids of magmatic-hydrothermal deposits. Abundant minerals are present as solid phases in $H_2O$-$CO_2$ fluid inclusions in stage I quartz: $Cu_{1.65}S$, covellite, chalcopyrite, bornite, molybdenite, pyrite, colusite, anhydrite, and celestine. $\delta^{18}O_{quartz}$ values of stage I quartz range from 10.2 to 12.0‰, with calculated $\delta^{18}O_{fluid}$ values ranging from 5.6 to 7.4‰. The δD values of fluid inclusion

waters (thermal decrepitation) in stage I quartz range from -117 to -54‰. The low and scattered δD values reflect a mixture of ore-forming fluids trapped by the $H_2O$-$CO_2$ fluid inclusions at deep crustal levels, and post-mineralization fluids, possibly meteoric waters, trapped by secondary aqueous fluid inclusions at higher crustal levels during uplift of the Xiaoqinling core complex. Four molybdenite samples yield an Re-Os isochron age of 206.4 ± 3.9 Ma (MSWD = 0.88), suggesting ore formation in the Late Triassic. Metal signature, mineral association, fluid characteristics, and isotope data of the Dahu deposit, together with the tectono-magmatic setting, imply that the ore-forming fluids were derived from an unexposed and oxidized igneous system, which likely stems from partial melting of enriched lithospheric mantle beneath the North China Craton in a post-collisional extensional setting.

The Yangzhaiyu Au deposit is one of the largest gold deposits in the Xiaoqinling region, with a proven reserve of 34 t Au (grade: 11.4 g/t Au). The ore-mineral assemblage of the Yangzhaiyu Au deposit consists of pyrite, chalcopyrite, galena, bornite, sphalerite, gold, and native tellurium together with a wide variety of tellurides and Bi-sulfosalts. The telluride mineral assemblage comprises Phase A, sylvanite, hessite, petzite, calaverite, stützite, rucklidgeite, altaite, volynskite, tellurobismuthite, tetradymite, and buckhornite. The Bi-sulfosalts are Phase B, aikinite, felbertalite, and wittichenite. The telluride and gold mineralization took place at or below about 220 ℃ and evolved towards decreasing $f_{Te2}$. There are two unnamed phases: Phase A and Phase B. Phase A, with the empirical formula of $AgTe_3$, occurs in small intergrowth aggregates with sylvanite and chalcopyrite, and locally with bornite, galena, and altaite. Phase A and its associated minerals occur along healed micro-fractures in pyrite. Phase A has a distinctly golden reflection color, without discernable reflectance pleochroism or anisotropy. $AgTe_3$ was synthesized in 1982, but its natural occurrence has not been reported so far. Phase A is stable at low pressure, different from synthetic $AgTe_3$, which was reported to rapidly decompose below 0.4 GPa. The EBSD patterns of Phase A do not match the structure of the synthetic $AgTe_3$. Therefore, Phase A observed at the Yangzhaiyu Au deposit might be a low-pressure polymorph of the synthetic $AgTe_3$. Phase B, with the empirical formula of $Cu_{20}FePb_{11}Bi_9S_{37}$, was observed in an intergrowth aggregate together with hessite, galena, chalcopyrite, bornite, and buckhornite. It has pinkish grey reflection color, without discernable reflectance pleochroism or anisotropy. Although formed

about 80 Ma after the Dahu Au-Mo deposit, the metal signature (e.g., anomalous enrichment of Bi and Te) and ore-mineral assemblage (e.g., bornite, tellurides, Bi-sulfosalts) of the Yangzhaiyu deposit also suggests a magmatic-hydrothermal origin. Similar to the Dahu deposit, the parent magma most likely results from partial melting of the upper mantle. The mineralization of the Yangzhaiyu Au deposit is related to lithospheric thinning in eastern China during the Early Cretaceous.

The mineralization of the Dahu and Yangzhaiyu deposits, and by analogy the Late Triassic and the Early Cretaceous Au-Mo mineralization events in the Xiaoqinling region, are both related to and coeval with large-scale magmatism. The critical fundamental control on Au-Mo metallogeny in the Xiaoqinling region is probably the presence of a metasomatised upper mantle, which is produced by early subduction-related processes before the final collision between the North China Craton and the Yangtze Craton and becomes a long-term source of mineralization-associated magma and hydrothermal fluid components.

**Keywords:** Central China, Xiaoqinling region, Dahu Au-Mo deposit, Yangzhaiyu Au deposit, vein style, tellurides, sulfosalts, $AgTe_3$, fluid inclusions, stable isotopes, Re-Os dating, magmatic-hydrothermal origin

# Acknowledgments

First and foremost, I would like to express my special thanks to my supervisor Prof. Dr. Bernd Lehmann for his constant support and guidance. His enthusiasm and dedication to economic geology has always been a source of motivation for me as a young geologist. His in-depth knowledge on a broad spectrum of geosciences has extremely inspired me. “A single conversation across the table with a wise man is worth a month's study of books.” –Chinese proverb. I thank him for giving me the opportunity to study at Clausthal University of Technology, offering me invaluable advice, and guiding me in the right direction.

I would like to thank my former postgraduate supervisor Prof. Dr. Jingwen Mao from Chinese Academy of Geological Sciences, for helping me to start my doctoral study in Germany, and for his caring, support, and invaluable advice during my doctoral study.

I am very grateful to Prof. Dr. Kurt Mengel for consenting to be the reviewer of this dissertation.

I want to thank the many present and former members from the Institute für Endlagerforschung: I am particularly thankful to Klaus Herrmann for his meticulous assistance in the electron-microprobe analysis. I thank Dr. Eike Gierth for his assistance in ore microscopy. I thank Ulf Hemmerling for preparing excellent polished sections. I thank Fred Türck for his computer assistance. I thank Elvira Schulze, our secretary, for her assistance. I am very thankful to Dr. Lingang Xu for kindly helping me to start my life and study in Germany, and he has always been a source of friendship, good advice, and collaboration. I am very grateful to Dr. Alexandre Raphael Cabral for many insightful suggestions and discussions. I thank Stephanie Lohmeier and Stefan Halder for their kindness, support, friendship, and help in many things that a foreigner has to face in Germany, as well as for introduction to some nice and interesting people. I thank Dr. Jasmi Hafiz Abdul Aziz and Dr. Rongqing Zhang for their support and many constructive discussions.

I thank Dr. Huishou Ye and Dr. Maohong Chen from Chinese Academy of Geological Sciences for being my guarantors. Dr. Huishou Ye is also greatly thanked for his encouragement and support during my doctoral study, as well as providing funding for my flied

work.

I thank Ingmar Ratschinski from Institut für Nichtmetallische Werkstoffe, TU Clausthal for his assistance with the scanning electron microscope analysis. I thank Moritz Albrecht from University of Hannover for his assistance with the UV-fs-LA-ICP-MS analysis of fluid inclusions. I thank Dr. Roman Skála from Geological Institute of the Academy of Sciences of the Czech Republic and Dr. Anna Vymazalova from Czech Geological Survey for their discussions and suggestions of the EBSD data. I am thankful to Chao Li for discussions of the Re-Os molybdenite data.

I am very thankful to staff from the Jinyuan Mining Industry Company for allowing me to get access to the deposits and providing help and support during my filed work: Zongyan Li, Xiaoming Zhang, Jinge Zhang, Hai Zhang, Jiangwei Feng, Haijiang He, Yongzhe Ye, Weilong Li, Kangning Liu, Hongbin Xue, and Zhiqiang Cui.

I also thank my friends for all the emotional support, entertainment, and caring they provided: Jin Chai, Xiaosong Wang, Yue Yu, Xiaoying Liu, Zichen Yu, Yang Zhao, and Xu Xing.

This research project was funded by the Chinese Scholarship Council, the Geological Survey Project of China (1212011220869), the National Natural Science Foundation of China (No. 41272104), and Institute für Endlagerforschung, TU Clausthal.

Lastly, I wish to thank my parents, Ming Jian and Jingfang Wang, and my grandmother, Changxiu Ma. They raised me, taught me, loved me, and encouraged me at every stage of my life. To them I dedicate this thesis.

# Contents

# Chapter 1

# Introduction

## 1.1 Background

The Xiaoqinling region is a 135-km-long and 70-km-wide area bounded by the Taiyao fault to the north and the Luanchuan fault to the south (Figs. 1.1, 1.2; Hu et al., 1994). This region is located in the southern margin of the North China Craton, and belongs to the Qinling–Dabie Orogen.

The Xiaoqinling region has a proven gold reserve of more than 630 tonnes (Wu, 2012; Liu, 2013), with an annual gold production of 9 tonnes. Gold is mainly hosted in more than 1200 gold-bearing quartz veins (Li et al., 1996), which also show a very pronounced tellurium signature. Tellurium concentration in the gold ores is typically in the range of tens to hundreds of ppm, with estimated tellurium resources in excess of 1000 tonnes (Luan et al., 1985, 1991, Xue et al., 2004). Gold mining in the Xiaoqinling region dates back to the Song Dynasty (1096 A.D.), and large scale mining activities started in the Ming Dynasty (1450 A.D.) (Li et al., 1996). In the early 1960s, the Bureau of Geology and Mineral Resources (BGMR) of Henan province initiated a geological survey in the Xiaoqinling region. Subsequent gold exploration was conducted by the No.1 Geological Team of BGMR of Henan province, the No.6 Geological Team of BGMR of Shaanxi province, and the Chinese People's Military Police Troops (Mao et al., 2002).

The Xiaoqinling region also constitutes a part of the East Qinling–Dabie Mo metallogenic belt, which has a proven molybdenum reserve of 8.43 million tonnes (Mao et al., 2011). Most of the Mo deposits belong to porphyry or porphyry-skarn type, such as the giant Jinduicheng porphyry Mo deposit (1 million tonnes of Mo grading at 0.099 g/t Mo; Mao et al., 2011). Recently, however, economic Mo concentration was also found in gold-bearing quartz veins at the Dahu deposit and its adjacent area.

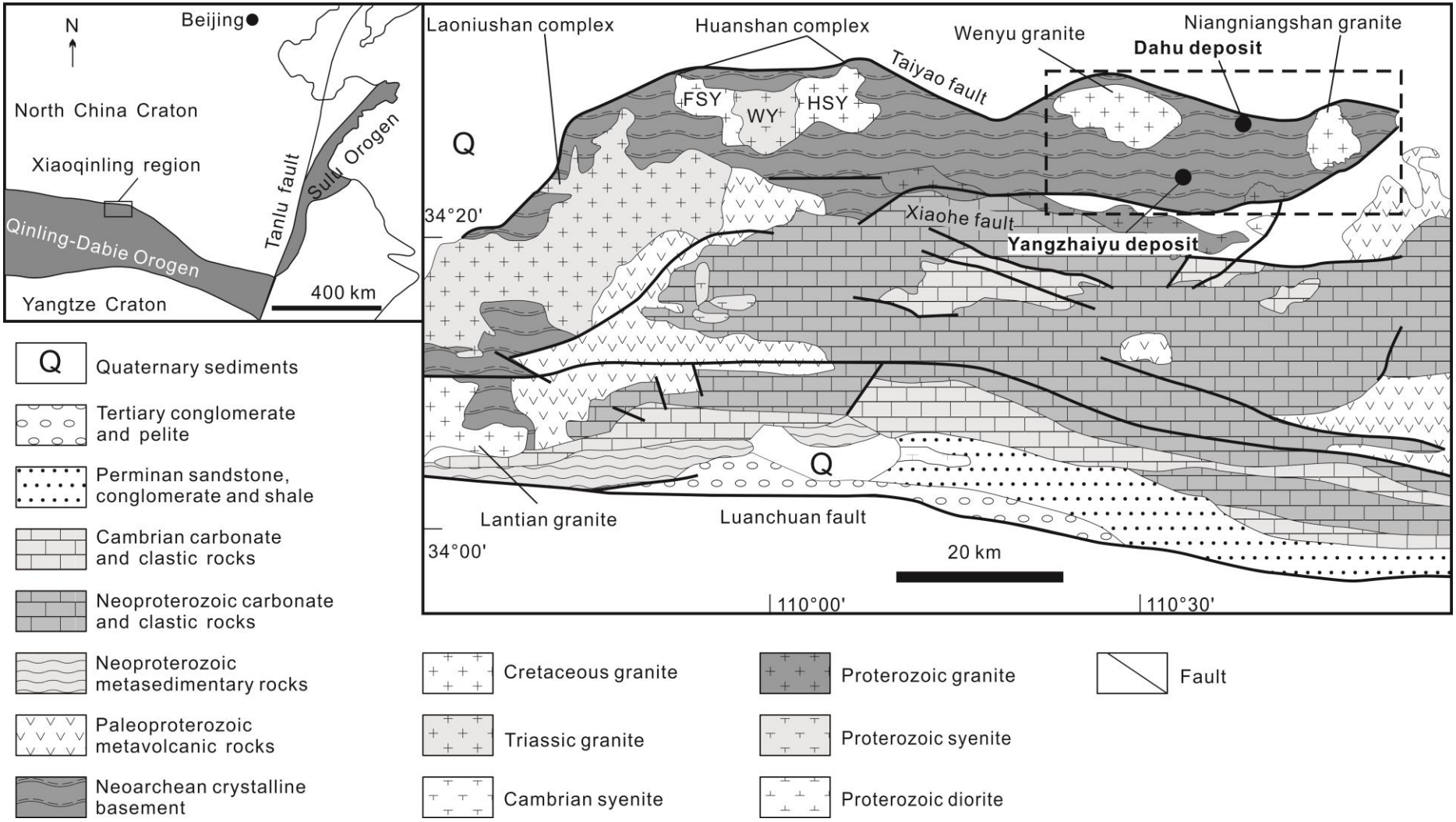


FIG. 1.1. Geologic map of the Xiaoqinling region (compiled from Mao et al., 2002; Hu ZG et al., 1994; Hu J et al., 2012) and its position in China (map of the North China Craton and adjacent area modified from Zhang et al., 2009), the rectangular area marked by dashed lines is detailed in Figure 1.2. Abbreviations: FSY = Fangshanyu biotite monzogranite, WY = Wengyu amphibole monzogranite, HSY = Huashanyu biotite monzogranite.

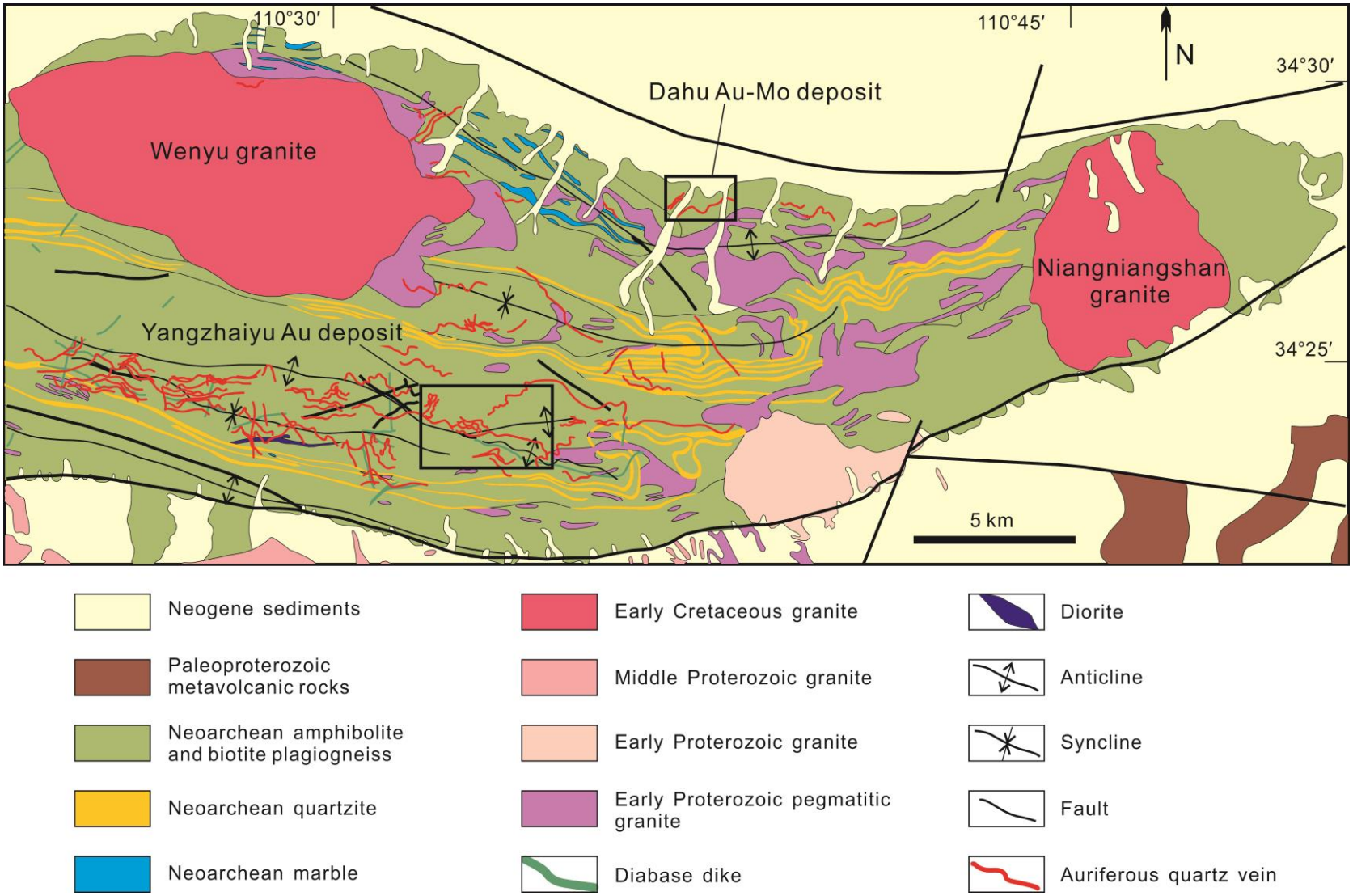


FIG. 1.2. Geologic map of the Xiaoqinling gold district (Henan province part; compiled from Cai and Su, 1985; Li et al., 2006). The rectangular areas marked by black lines are detailed in Figure 3.1 and Figure 4.1.

## 1.2 Previous studies and objectives of this study

Gold-bearing quartz veins in the Xiaoqinling region are mainly controlled by a series of shallow to moderate dipping (mostly between 25° and 45°) faults which dominantly strike E–W. They typically vary in strike length and width from hundreds of meters to several kilometers and tens of centimeters to several meters, respectively. Vein minerals mainly consist of quartz (70–90 vol.%), sulfides (5–10 vol.%), and carbonates (<5 vol.%) (Luan et al., 1985). Luan et al. (1985) divided the mineralization of the gold-bearing quartz veins into four stages: an initial quartz–pyrite stage characterized by milky white quartz and minor coarse-grained euhedral pyrite, a pyrite-dominated stage characterized by fine-grained pyrite and small amounts of gold, a base-metal sulfide stage characterized by abundant galena and chalcopyrite, and accessory gold, tellurides, and Bi-sulfosalts, and a final barren carbonate-dominated stage. This four stage mineralization model has been widely accepted and is the basis for understanding the mineral paragenesis in the Xiaoqinling region. Since then, extensive publications have appeared. Hu et al. (1994) gave a detailed work on ore-controlling structures. Li et al. (1996) presented a detailed study on vein geometry, occurrence, and mineralogy. Many studies (Luan et al., 1985, 1990; Cao et al., 1989, Zhu et al., 1989, Luo et al., 1992; Tian et al., 1994; Fang 1996; Li et al., 1996; Wang et al., 1998) also concentrated on telluride and Bi-sulfosalt mineralogy. Abundant tellurides and Bi-sulfosalts, such as altaite [PbTe], calaverite [$AuTe_2$], krennerite [$AuTe_2$], tellurobismuthite [$Bi_2Te_3$], volynskite [$AgBiTe_2$], tetradymite [$Bi_2Te_2S$], aikinite [$PbCuBiS_3$], hammarite [$Pb_2Cu_2Bi_4S_9$], and krupkaite [$PbCuBi_3S_6$], have been reported. Fluid inclusion microthermometric studies (Xie et al., 1998; Jiang et al., 1999, 2000) recognized that low to moderate salinity $H_2O$-$CO_2$ fluid inclusions dominate in gold-bearing quartz veins. Based on a review of previous studies, Mao et al. (2002) summarized the geology and distribution of the gold deposits in the Xiaoqinling region and attributed them to the class of orogenic gold deposits.

Recent studies in the Xiaoqinling region focused on geochronology (e.g., Xu et al., 1998., Wang et al., 2002, 2010., Li HM et al., 2007a, b., Li N et al., 2008, 2011., Li JW et al., 2012a, b), isotopic tracing (e.g., Nie et al., 2001; Lu et al., 2004; Xu et al., 2004; Wang et al., 2005; Qi et al., 2006; Ni et al., 2009), and fluid inclusion microthermometry (e.g., Fan et al., 2000, 2003; Ni et al., 2008; Wu et al., 2012), with few studies (e.g., Bi et al., 2011a; Zhao et al., 2011a, b) putting emphasis on the mineralogy aspect. However, improved micro-analytical resolution in recent years has assisted the identification of less common minerals or previously

unreported phases, even when present as very small grains, which have been overlooked during precious studies but can provide valuable information on ore genesis. More importantly, the discovery of economic molybdenum concentration at the Late Triassic Dahu Au-Mo deposit bring a new challenge to the understanding of the mineralogy and mineral paragenesis of the gold-bearing quartz veins. Although mine geology studies (Zhang et al., 2012), fluid inclusion work (Ni et al., 2008), Pb-Sr-Nd isotopic tracing (Ni et al., 2012), and a number of geochronological studies (Li HM et al., 2007a; Li N et al., 2008, 2011) have been carried out for the Dahu Au-Mo deposit, the mineralogy and mineral paragenesis, especially the temporal and spatial relations between gold and molybdenum mineralization are still poorly understood.

A large number of $^{40}Ar/^{39}Ar$ mica ages and Re-Os molybdenite ages from the gold-bearing quartz veins in the Xiaoqinling region cluster in the Late Jurassic–Early Cretaceous (154–119 Ma: Xu et al., 1998; Wang et al., 2002; Li et al., 2012a, b). Recently, more and more age data suggest that the Triassic is another important Au-Mo mineralization period in the Xiaoqinling region and the Qinling–Dabie Orogen, aside from the large-scale Au-Mo mineralization during the Late Jurassic–Early Cretaceous (e.g., Mao et al., 2005, 2008, 2011; Ye et al., 2008; Jiang et al., 2009; Zhang et al., 2010; Bi et al., 2011a; Li et al., 2012a, b). The Late Jurassic–Early Cretaceous Au-Mo mineralization is related to tectonic reactivation and lithospheric thinning of eastern China induced by underthrusting of the Paleo-Pacific plate beneath the eastern China continent (e.g., Mao et al., 2008; Li et al., 2012a), while the Triassic Au-Mo mineralization is related to final collision between the North China Craton and the Yangtze Craton, and the subsequent post-collisional extensional process (Mao et al., 2012). Triassic quartz-vein style Au deposits (e.g., Liba Au deposit, ~216 Ma: Zeng et al., 2012; Liziyuan Au deposit, ~229 Ma: Yang et al., 2013), quartz-vein style Au-Mo deposits (e.g., Majiawa Au-Mo deposit, 232 ± 11 Ma: Wang et al., 2010; Dahu Au-Mo deposit), quartz-vein style Mo deposits (e.g., Qianfangling Mo deposit (239 ± 13 Ma) and a number of Mo occurrences in the Songxian County: Gao et al., 2010), carbonatite-related vein style Mo deposits (e.g, Huanglongpu Mo deposit, 221.5 ± 0.3 Ma: Stein et al., 1997), and porphyry Mo deposits (e.g., Wenquan Mo deposit, 214.4 ± 7.1 Ma: Zhu et al., 2011) have all been reported. However, compared with the Late Jurassic–Early Cretaceous Au-Mo mineralization, studies on the Triassic Au-Mo mineralization have been lagging behind, and in-depth discussions on ore genesis for individual deposits are hitherto lacking.

Further, the Triassic quartz vein style Au-Mo/Mo deposits represent an unusual type of Mo mineralization, because causative intrusions are missing within individual mining areas, although Mo deposits are commonly of a magmatic-hydrothermal origin (e.g., porphyry

deposits, skarn deposits, greisen deposits, pegmatite deposits: White et al., 1981). The Triassic quartz vein style Au-Mo/Mo deposits share common features such as strong structural control of mineralization, thick quartz vein systems (often >1 m), intense K-feldspar alteration, $CO_2$-rich fluid inclusions, and widespread presence of hypogene sulfate. Their common features and similar time of mineralization imply a possible genetic link, and a well-constrained genetic model would be a valuable exploration tool, but current genetic models are preliminary and conflicting.

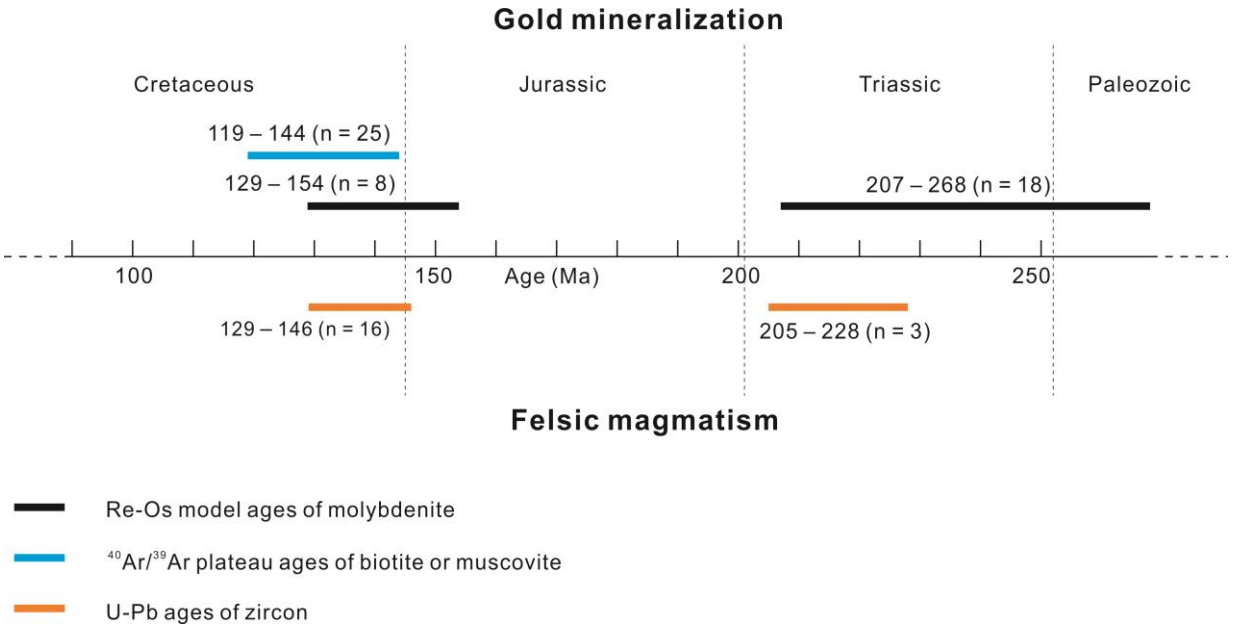


Fig. 1.3. Age distribution of gold deposits and granitic intrusions in the Xiaoqinling region. Age data are from Guo et al. (2009), Li HM et al. (2007a), Mao et al. (2010), Wang et al. (2002, 2010), Ding et al. (2011), Hu et al. (2012), Li JW et al. (2012a, b), Xu et al. (1998), Zhao et al. (2012) and this study.

This research focuses on the Dahu Au-Mo deposit and the Yangzhaiyu Au deposit in the Xiaoqinling region and aims:

(1) to better understand the mineralogy of the Dahu Au-Mo deposit and the Yangzhaiyu Au deposit by ore microscopy, electron microprobe analysis, scanning electron microscope analysis, and electron backscatter diffraction analysis;

(2) to constrain the fluid composition of the Dahu Au-Mo deposit by fluid inclusion petrography, microthermometry, Raman spectroscopic analysis, and Uv-Fs-LA-ICP-MS (Ultraviolet femtosecond laser ablation-inductively coupled plasma-mass spectrometry) analysis;

(3) to add some stable isotope and geochronological data to better constrain the fluid source and timing of mineralization for the Dahu Au-Mo deposit;

(4) to add some arguments on the origin of the Dahu Au-Mo deposit and the Yangzhaiyu Au deposit from the mineralogy perspective;

(5) to establish metallogenic models for the Late Triassic Dahu Au-Mo deposit and the Early Cretaceous Yangzhaiyu Au deposit based on the above research results and previous studies.

Fig. 1.4. Xiaoqinling mountain range.


Fig. 1.5. Road to the mining area.

Fig. 1.6. Mining activities along a valley. Several pitheads of underground mining projects are located along the valley.


Fig. 1.7. Pithead of an underground mining project.

# Chapter 2
# Regional Geology

## 2.1 Mesozoic tectono-magmatic evolution of the Qinling–Dabie Orogen

The west-northwest trending Qinling–Dabie Orogen marks the boundary between the North China and Yangtze Cratons (Fig. 1.1). This composite fold-and-thrust belt formed by multi-stage collision between the North China Craton and the Yangtze Craton, and the final collision between the two cratons occurred during the Triassic (e.g., Ames et al., 1993; Hacker et al., 1998; Zhang et al., 2001; Ratschbacher et al., 2003; Wu et al., 2006; Mao et al., 2008; Dong et al., 2011), probably between 242 and 227 Ma (Wu et al., 2006).

During the Late Triassic, the Qinling–Dabie Orogen evolved into a post-collisional extensional domain (Mao et al., 2008; Dong et al., 2011), which is indicated by emplacement of many post-collisional intrusions, including lamprophyre dikes (219 ± 2 Ma, Wang et al., 2007a), rapakivi-textured granitoids (i.e., Shahewan pluton: 209 ± 2 Ma, Wang et al., 2011a; Laojunshan pluton: 214 ± 3 Ma, Lu et al., 1999; Qinlngliang pluton: 212 ± 2 Ma, Wang et al., 2011a; Taibailiang pluton: 216 ± 1 Ma, Zhang et al., 2006), and granitic rocks with mafic microgranular enclaves (e.g., Yangba pluton: 208 ± 2 to 207 ± 2 Ma, Qin et al., 2010). The post-collisional magmatism was probably related to break-off of the subducted slab (Wang et al., 2007a; Qin et al., 2010; Ding et al., 2011; Hu et al., 2012). Slab break-off caused asthenospheric upwelling, which in turn led to partial melting of an ancient enriched lithospheric mantle and the lower crust beneath the southern margin of the North China Craton and the North Qinling Belt, thus resulting in the formation of voluminous mafic and felsic magmas. The lithospheric mantle enrichment is probably produced by early subduction-related processes (Wang XX et al., 2007a; Wang F et al., 2007b; Hu et al., 2012).

The Early Jurassic represents a phase of quiescence after the assembly of the North China Craton, South China block, and Indo-China block. There was no granitic magmatism throughout the major part of the East China continental margin (Mao et al., 2010). Since the Middle Jurassic, eastern China, including the eastern part of the Qinling–Dabie Orogen, became a part of the circum-Pacific tectonic regime, resulting from underthrusting of the Izanagi plate (or Paleo-Pacific plate) beneath the Eurasian continental margin. Prior to ~135 Ma, the Izanagi plate underwent orthogonal convergence with the Eurasian continental margin, and subducted at a shallow angle or as a flat slab. Abundant felsic magmatism developed in

back-arc extensional zones and parallel to the continental margin. After ~135 Ma, the Izanagi plate motion changed, and became parallel to the continental margin at ~115 Ma (Goldfarb et al., 2007; Mao et al., 2010). Between ~134 and 108 Ma, widespread magmatism was induced by the change in the Izanagi plate motion, and the tectonic regime of lithospheric thinning, asthenospheric upwelling, and partial melting of the lower crust (Mao et al., 2010).

### 2.2 Geology of the Xiaoqinling region

The Xiaoqinling region is a 135-km-long and 70-km-wide area bounded by the Taiyao fault to the north and the Luanchuan fault to the south (Figs. 1.1, 1.2; Hu et al., 1994). This region is located in the southern margin of the North China Craton, and belongs to the Qinling–Dabie Orogen. The southern margin of the North China Craton was originally a part of the North China Craton, but was involved in Mesozoic–Cenozoic intra-continental orogenic deformation and has become a part of the Qinling–Dabie Orogen (Zhang et al., 2001; Dong et al., 2011).

The strata exposed in the Xiaoqinling region include Archean amphibolite-facies metamorphic rocks of the Taihua Group, Paleoproterozoic metavolcanic rocks of the Xiong'er Group, Neoproterozoic metasedimentary rocks, Cambrian carbonate and clastic rocks, Permian sandstone, conglomerate, and shale, and Cenozoic cover (Luan et al., 1991; Mao et al., 2002; Zhao et al., 2004). Gold deposits are mainly hosted within the Archean amphibolite-facies metamorphic rocks, which consist of biotite plagiogneiss, amphibole plagiogneiss, amphibolite, quartzite, and marble (Cai and Su, 1985). These rocks probably formed in the Neoarchean, and have been subjected to amphibolite-facies metamorphism in the Paleoproterozoic (Zhou et al., 1998; Ni et al., 2003; Li et al., 2007b).

The Archean rocks were intruded by pegmatite sills and dikes in the Paleoproterozoic (1955 ± 30 Ma: Li et al. , 2007b), mafic dikes in the Paleoproterozoic (1851 ± 18 to 1719 ± 21 Ma: Wang et al., 2008; Bi et al., 2011; Li et al., 2012b) and the Early Cretaceous (130 ± 4 to 126 ± 1 Ma: Wang et al., 2008; Zhao et al., 2010; Li et al., 2012b), and granitic plutons in the Proterozoic and Mesozoic. Mesozoic granitic intrusions formed during the Late Triassic and the Early Cretaceous, and are widely exposed in the Xiaoqinling region.

Late Triassic plutons (Fig. 1.1) include the Laoniushan granitic complex (zircon LA-ICP-MS U-Pb age, 228 ± 1 to 215 ± 4 Ma: Ding et al., 2011) and the Wengyu amphibole monzogranite (zircon LA-ICP-MS U-Pb age, 205 ± 2 Ma: Hu et al., 2012) within the Huashan granitic complex (i.e., not the Early Cretaceous Wenyu granite in figure 1.2). The Laoniushan granitic complex consists of four intrusive units, from early to late, biotite monzogranite (20–30% quartz, 40% K-feldspar, 30% plagioclase, 3–5% biotite), quartz diorite (70%

plagioclase, 20–25% K-feldspar, 10% quartz, 3–4% amphibole, 1–2% biotite), quartz monzonite (50% plagioclase, 30% K-feldspar, 5–10% quartz, 3–5% amphibole, <5% biotite), and hornblende monzonite (Ding et al., 2011). The biotite monzogranite is similar to potassium-rich adakite, whereas the other three units have a shoshonitic affinity. Both the adakitic and shoshonitic rocks contain abundant mafic microgranular enclaves (Ding et al., 2011). The Wengyu amphibole monzogranite lies in the central section of the Huashan granitic complex (Fig. 1.1). It consists of quartz (30–35%), plagioclase (25–30%), K-feldspar (30–35%), amphibole (4%), biotite (1%), accessory apatite, magnetite, sphene, zircon, and allanite, and mafic microgranular enclaves (Li et al., 1993; Hu et al., 2012). The Wengyu amphibole monzogranite has high $SiO_2$ contents, total alkali contents, and $FeO^{total}/(FeO^{total} + MgO)$ ratios. It is strongly enriched in large-ion lithophile elements (especially Sr and Ba) and light rare earth elements, and depleted in high field strength elements and heavy rare earth elements, displaying geochemical characteristics of high-Ba–Sr granites (Hu et al., 2012). The Laoniushan granitic complex and the Wengyu amphibole monzogranite were produced mainly by partial melting of lower continental crust of the North China Craton; the latter contains minor enriched lithospheric mantle components. They are both emplaced in a post-collisional extensional setting of the Qinling–Dabie Orogen and related to break-off of the subducted slab (Ding et al., 2011; Hu et al., 2012).

Early Cretaceous plutons (Figs. 1.1, 1.2) include the Lantian monzogranite (zircon LA-ICP-MS U-Pb age, 133 ± 1 Ma: Wang et al., 2011b), the Wenyu biotite monzogranite (zircon LA-ICP-MS U-Pb age, 141 ± 2 to 136 ± 3 Ma: Li et al., 2012; zircon LA-ICP-MS U-Pb age, 131 ± 1 Ma: Zhao et al., 2012), the Niangniangshan biotite monzogranite (zircon SHRIMP U-Pb age, 142 ± 3 Ma: Wang et al., 2010; zircon LA-ICP-MS U-Pb age, 134 ± 1 Ma: Zhao et al., 2012), and the Huashanyu biotite monzogranite (zircon SHRIMP U-Pb age, 146 ± 2: Mao et al., 2010) and Fangshanyu biotite monzogranite (zircon LA-ICP-MS U-Pb age, 132 ± 1 Ma: Hu et al., 2012) within the Huashan granitic complex. The Early Cretaceous rocks were mainly derived from partial melting of the Archean Taihua rocks (Wang YT et al., 2010; Wang XX et al., 2011b; Zhao et al., 2012; Hu et al., 2012).

Three large E–W-striking faults represent the major structures of the Xiaoqinling region. They are, from south to north, the Luanchuan fault, the Xiaohe fault, and the Taiyao fault. The Taiyao and Xiaohe detachment faults define the northern and southern boundaries of the Xiaoqinling metamorphic core complex, which mainly consists of Archean amphibolite-facies metamorphic rocks and younger granite plutons. Within the Xiaoqinling metamorphic core complex, the area to the east of the Huanshan complex hosts most of the gold deposits, and

thus is known as the Xiaoqinling gold district. Gold-bearing quartz veins concentrate along the axes of several E–W-striking folds, and are controlled by small to medium size E–W-striking faults, which are generally concordant with the host-rock foliations. These ore-controlling faults probably formed after the two large detachment faults (Li et al., 1996).

# Chapter 3

# Mineralogy, fluid characteristics, and Re-Os age of the Dahu Au-Mo deposit: evidence for a magmatic-hydrothermal origin

## 3.1 Deposit geology

The quartz-vein style Dahu Au-Mo deposit has proven reserves of 31 t gold (grade: 4.7 g/t Au) and 30,000 t molybdenum (grade: 0.13% Mo) (Feng et al., 2011), with an annual gold production of about 300 kg and molybdenum production of about 900 t. It was discovered by the No.1 Geological Team of BGMR (Bureau of Geology and Mineral Resources) of Henan province in 1981 (Yang et al., 1995; Feng et al., 2011). A high concentration of molybdenite in gold orebodies has long been recognized, but it was only in 2005 when the molybdenum resources were evaluated due to the high price of molybdenum at that time.

The Dahu Au-Mo deposit is located on the northern side of the Wulicun anticline, and hosted by biotite plagiogneiss, amphibole plagiogneiss and amphibolite of the Archean Taihua Group (Figs. 3.1, 3.2). The Taihua Group was intruded by mafic dikes and granite porphyries.

More than 50 mafic dikes are present, and they dominantly strike NW, dip NE, and vary in strike length and width from 10–1100 m and 0.5–50 m, respectively (Yang et al., 1995). Bi et al. (2011b) reported a zircon LA-ICP-MS U-Pb age of 1816 ± 14 Ma for a mafic dike. Several granite porphyry dikes are present. They strike NW, dip NE, and vary in strike length and width from 10–1100 m and 3–6 m, respectively (Yang et al., 1995). These rocks are locally cut by mineralized quartz veins, but their exact age is unknown. The major structures at the Dahu deposit are E–W-, NW-, and NE-striking faults. The NW- and NE-striking faults are mainly filled by mafic and granite porphyry dikes, whereas the E–W-striking faults, from north to south, F1, F8, F7, F35, F5, and F6, control the mineralized quartz veins. The F5 fault zone (8 km long and 10–150 m wide) is the largest ore-bearing structure and possesses a curvi-planar geometry. It varies in strike from WNW–ESE to ENE–WSW, but is generally north dipping (Figs. 3.1, 3.2).

Mineralized quartz veins dip to NW at shallow to moderate angles (23–52 °). Individual veins are parallel or slightly oblique to each other and the host structures. Gold and molybdenum orebodies are defined by a cut-off grade of 1 g/t Au and 0.03% Mo, respectively. Gold orebodies and molybdenum orebodies usually contain sub-economic concentrations of

molybdenum and gold, respectively, and molybdenite is widespread in gold orebodies. They occur in different veins or in different parts of the same vein, and locally overlap. Within individual faults, gold orebodies are more developed in the higher levels, while molybdenum orebodies are more developed in the lower levels (e.g., Fig. 3.2).

Twenty-five gold orebodies extend from 1012 m (surface) to -196 m in elevation. The No. 19 orebody, the largest gold orebody, has a gold reserve of 14 tonnes (6.6 g/t), with significant enrichment of Cu (0.3%), Pb (1%), Mo (0.04%), Bi (103 ppm), and Te (32 ppm, Yang et al., 1995). It dips to NW at 33 °, and varies in thickness from 0.5 to 17.4 m (average 2.0 m), with a vertical extension from 1012 to 72 m NN, and a strike length of about 1490 m, with pinch and swell domains, and branches.

Ten molybdenum orebodies are all blind with respect to the surface, and extend from 750 to -40 m in elevation. The F5-up2 orebody, the largest molybdenum orebody, has a molybdenum reserve of 12000 tonnes (grade: 0.12% Mo). It dips to NW at 29 °, and varies in thickness from 0.7 to 38.2 m (average 8.9 m). It extends from 600 to -40 m in elevation, and continues along strike for 1660 m. We analyzed 32 molybdenum ore samples from different molybdenum orebodies. They show an average molybdenum grade of 0.5% and an average gold grade of 0.1 g/t, and also show significant enrichment of Pb (3000 ppm) and Bi (20 ppm, Table 3.1).

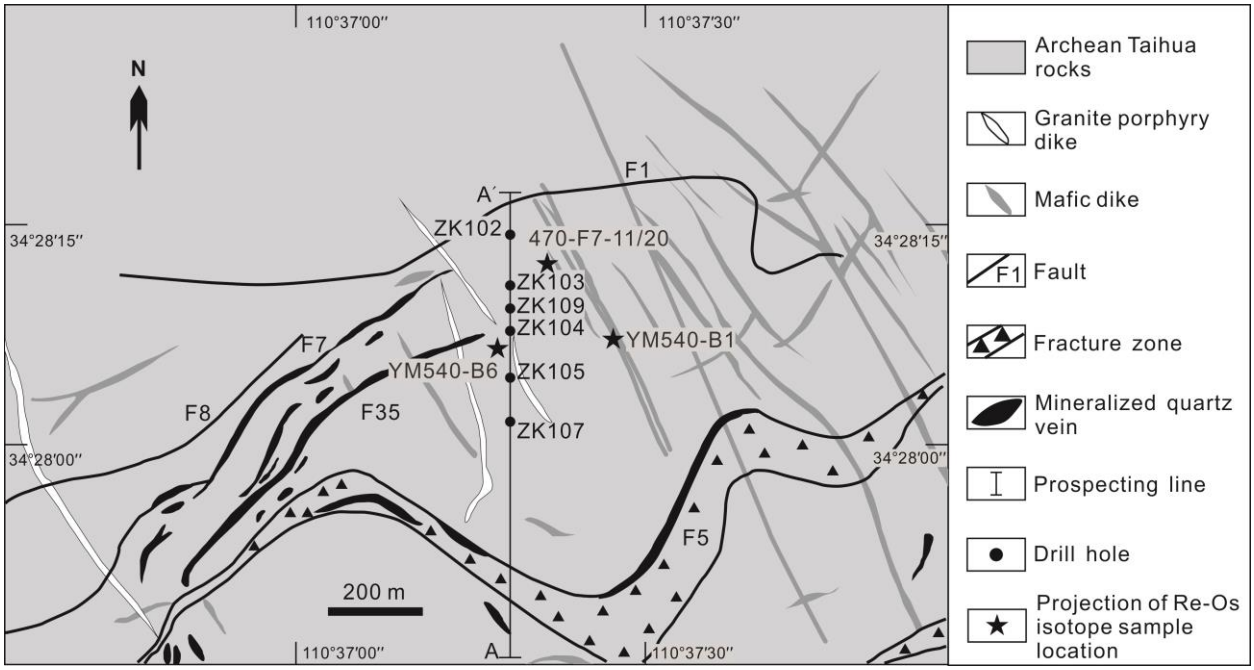


FIG. 3.1. Geologic map of the Dahu Au-Mo deposit (modified from Yang et al., 1995).

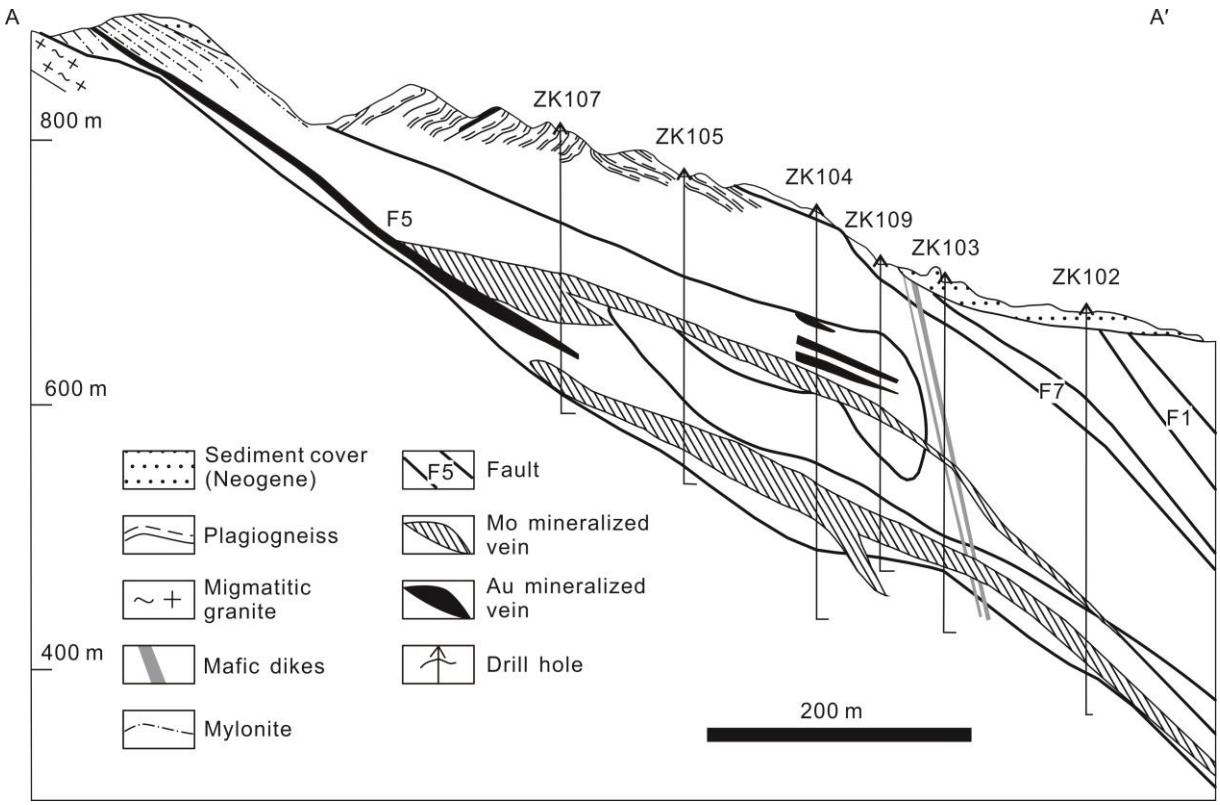


FIG. 3.2. Cross section of A–A' at the Dahu Au-Mo deposit (modified from Yang et al., 1995).

Hydrothermal alteration and vein mineralogy were studied in about 55 polished thin sections and 14 polished sections by microscopy. Ore microscopy was accompanied by electron microprobe analysis, which was carried out at Clausthal University of Technology, Germany, using a Cameca SX100 electron microprobe. Analytical conditions, standards and X-ray emission lines for electron microprobe analysis are given in the table notes.

### *3.1.1 Hydrothermal alteration*

Ore-related hydrothermal alteration includes K-feldspathization, biotitization, chloritization, sericitization, silicification, and carbonatization. An inner alteration zone and an outer alteration zone are distinguished.

*Inner alteration zone:* All of the molybdenum mineralized quartz veins and some gold mineralized quartz veins are surrounded by a K-feldspar-rich inner alteration zone characterized by its reddish appearance. The width of this alteration zone is less than the width of the vein, and varies from several millimeters to several meters (Fig. 3.3A, B, 3.4A). Wall-rock plagioclase and biotite have been extensively (>50 %) altered, while amphibole has been virtually obliterated. Alteration minerals mainly consist of K-feldspar, sericite, carbonates, and quartz. K-feldspar is the most abundant alteration mineral and formed by replacement of

plagioclase. K-feldspar is an early alteration mineral subsequently altered to calcite, sericite, and quartz in small amounts (Fig. 3.3C). Molybdenum mineralization is always related to intense K-feldspathization of the wall rocks. Sericite formed by replacement of plagioclase, biotite, and K-feldspar (Fig. 3.3C). Carbonates, mainly calcite, occur as veinlets (Fig. 3.3C) or clusters replacing all other silicate minerals. Carbonates range from sparse to widespread, and are more abundant in amphibolite and amphibole plagiogneiss than in biotite plagiogneiss. Sulfides including pyrite, chalcopyrite, galena, and molybdenite often occur as disseminations. Some gold mineralized quartz veins lack a K-feldspar-rich inner alteration zone, and are surrounded by an inner alteration zone characterized by the alteration assemblage of sericite + quartz + pyrite (in biotite plagiogneiss) or sericite + carbonates + pyrite (in amphibole plagiogneiss and amphibolite).

*Outer alteration zone:* Away from the veins, the inner alteration zone gradually gives way to an alteration zone characterized by sericitization of plagioclase and chloritization of biotite and amphibole. Plagioclase has been extensively (>30%) altered to sericite (Fig. 3.3D). Amphibole has been extensively (>20%) altered to biotite and chlorite. Primary biotite has been extensively (>20%) altered to chlorite (Fig. 3.3E), muscovite, epidote, and calcite. Chlorite, in turn, has been partially altered to muscovite (Fig. 3.3E) and calcite. Calcite has also been observed to replace muscovite. Chlorite contains many inclusions of rutile and other Fe-Ti oxides. This alteration zone can extend tens of meters away from the veins, but its exact width is hard to evaluate. All the examined rock samples from the Dahu mining area show extensive alteration of plagioclase, biotite, and amphibole. It is worth to note that the Archean Taihua rocks have underwent pervasive Neoproterozoic retrograde greenschist facies metamorphism. However, regional metamorphism-related alterations are much weaker than the ore-related hydrothermal alteration features (e.g., Fig. 3.3F).

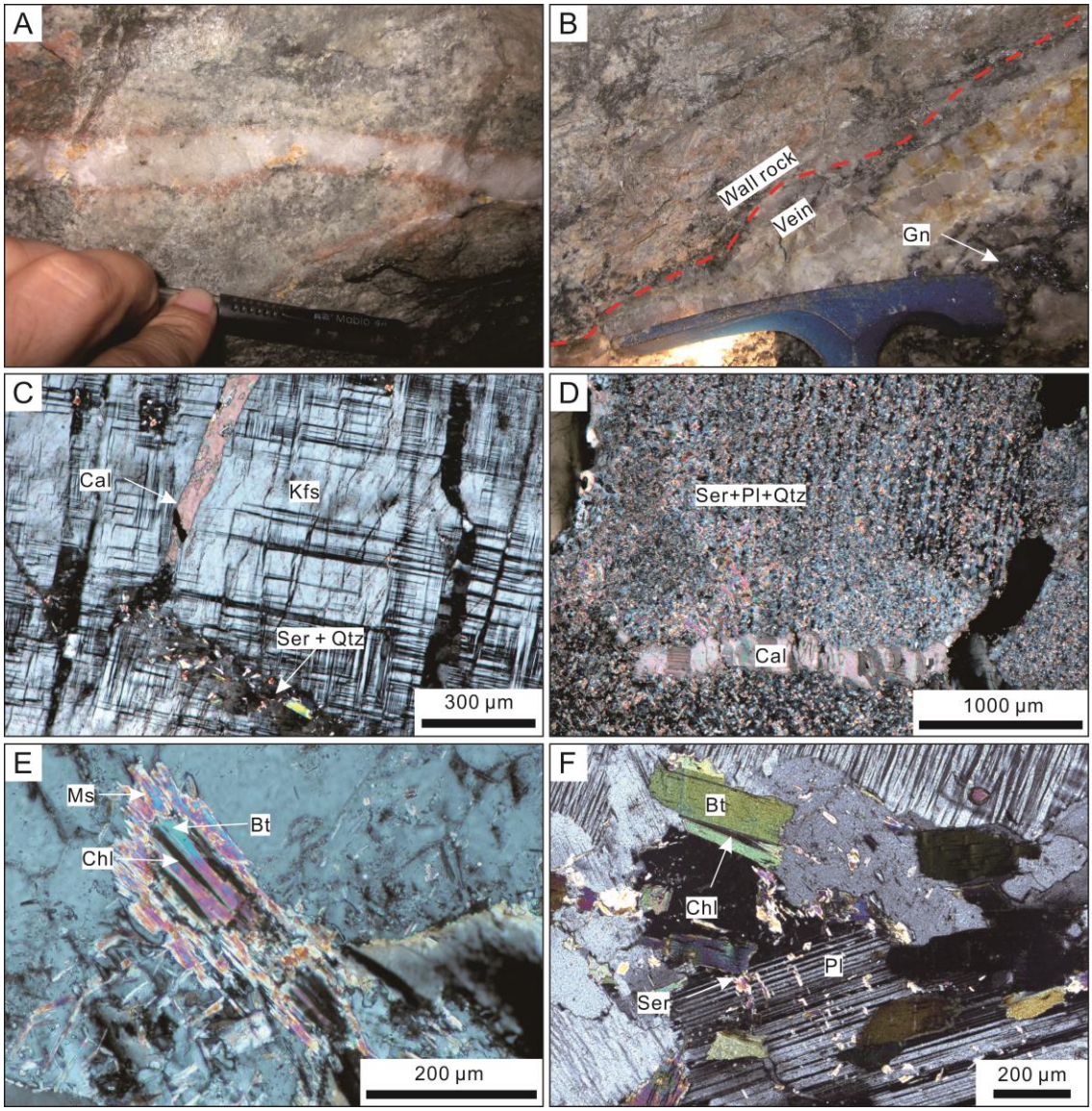


FIG. 3.3. Photographs (A, B) and photomicrographs (C–F) of ore-related hydrothermal alteration and regional metamorphism-related alterations. **A**. Mo mineralized quartz veinlet enclosed by narrow K-feldspar-rich selvages. F5/505 m. **B**. Gold mineralized quartz vein and wall rocks with intense K-feldspathization. F5/540 m. **C**. K-feldspar weakly altered to calcite, sericite, and quartz within a K-feldspar-rich inner alteration zone. This wall rock sample is about 6 meters away from a Mo mineralized quartz vein. Sample 505-10/505m, double-polarized transmitted light. **D**. Plagioclase extensively altered to the assemblage of sericite + quartz and cut by a calcite veinlet within an outer alteration zone. This wall rock sample is about 11 meters away from a Mo mineralized quartz vein. Sample 505-1/505 m, double-polarized transmitted light. **E**. Biotite extensively altered to chlorite and muscovite within an outer alteration zone. This wall rock sample is about 2 meters away from a Mo mineralized quartz vein. Sample 505-B35/505 m, double-polarized transmitted light. **F**. Biotite plagiogneiss away from mining areas showing weak chloritization and sericitization. Sample XQL-B10, double-polarized transmitted light. Abbreviations: Bt = biotite, Cal = calcite, Chl = chlorite, Gn = galena, Kfs = K-feldspar, Qtz = quartz, Pl = plagioclase, Ser = sericite, Ms = muscovite.

TABLE 3.1. Element concentrations (Au in ppb, others in ppm) in Mo ores

| Sample No. | Mn | Co | Ni | Cu | Zn | As | Mo | Ag | Sn | Sb | W | Au | Hg | Pb | Bi |
|---|---|---|---|---|---|---|---|---|---|---|---|---|---|---|---|
| 540-CD6-H4 | 873 | 18 | 20 | 916 | 128 | 1.2 | 4760 | 11 | 30 | 0.5 | 2.9 | 25 | 0.1 | 7995 | 11 |
| 540-CD6-H6 | 698 | 6.4 | 4.9 | 20 | 93 | 1.8 | 10440 | 0.2 | 4.2 | 0.7 | 1.0 | 110 | 0.4 | 111 | 4.9 |
| 540-YD12-H7 | 403 | 13 | 4.9 | 11 | 41 | 1.3 | 10600 | 0.2 | 21 | 1.3 | 0.9 | 110 | 0.4 | 76 | 8.5 |
| 540-YD12-H8 | 281 | 15 | 6.8 | 23 | 29 | 1.5 | 8040 | 0.2 | 18 | 0.7 | 0.9 | 40 | 0.3 | 63 | 9.7 |
| 540-CD9-H11 | 221 | 18 | 11 | 88 | 20 | 1.2 | 1200 | 0.2 | 4.4 | 0.4 | 17 | 680 | 0.1 | 84 | 48 |
| 540-CD9-H13 | 253 | 10 | 7.8 | 65 | 20 | 1.0 | 4480 | 0.2 | 8.2 | 0.7 | 1.9 | 110 | 0.1 | 6131 | 0.4 |
| 540-CD9-H14 | 154 | 4.9 | 4.5 | 43 | 19 | 1.4 | 2640 | 0.2 | 2.8 | 0.3 | 2.2 | 110 | 0.3 | 295 | 6.8 |
| 540-CD5-H1 | 330 | 1.0 | 4.5 | 14 | 19 | 5.2 | 260.0 | 0.2 | 1.9 | 0.3 | 7.9 | 6.0 | 0.2 | 12 | 0.5 |
| 540-CD5-H2 | 518 | 7.5 | 4.9 | 9.0 | 23 | 1.3 | 3600 | 0.2 | 5.8 | 0.4 | 2.3 | 110 | 0.1 | 95 | 4.7 |
| 540-CD5-H4 | 238 | 13 | 4.6 | 17 | 20 | 1.4 | 2320 | 0.2 | 3.5 | 0.3 | 2.4 | 100 | 0.4 | 72 | 69 |
| 540-CD5-H6 | 222 | 14 | 4.8 | 20 | 20 | 1.1 | 5280 | 0.2 | 8.4 | 0.3 | 8.0 | 20 | 0.2 | 125 | 80 |
| 540-CD5-H8 | 624 | 11 | 5.0 | 30 | 18 | 0.9 | 3400 | 0.2 | 9.9 | 0.4 | 1.0 | 80 | 0.5 | 1848 | 30 |
| 540-CD5-H9 | 205 | 1.0 | 4.9 | 22 | 18 | 1.5 | 1000 | 0.2 | 1.8 | 0.5 | 1.0 | 4.0 | 0.2 | 17 | 1.3 |
| 540-CD5-H11 | 974 | 2.5 | 4.8 | 48 | 26 | 1.4 | 2400 | 0.2 | 3.0 | 0.4 | 0.9 | 20 | 0.3 | 62 | 163 |
| 540-CD5-H12 | 683 | 16 | 18 | 40 | 18 | 1.5 | 2280 | 0.2 | 22 | 0.3 | 0.8 | 25 | 0.5 | 2087 | 26 |
| 540-CD9-H1 | 29 | 1.8 | 4.7 | 45 | 18 | 1.0 | 1080 | 0.1 | 2.0 | 0.3 | 8.0 | 100 | 0.5 | 63 | 1.9 |
| 540-CD9-H2 | 29 | 11 | 42 | 1069 | 16 | 0.9 | 9600 | 185 | 18 | 21 | 0.9 | 230 | 0.5 | 68246 | 73 |
| 540-CD9-H4 | 98 | 14 | 4.6 | 103 | 16 | 1.0 | 19640 | 0.4 | 25 | 1.1 | 1.0 | 40 | 0.2 | 323 | 13 |
| 540-CD9-H5 | 500 | 5.2 | 4.8 | 150 | 17 | 0.9 | 2800 | 0.1 | 2.8 | 0.3 | 1.0 | 40 | 0.2 | 63 | 2.9 |
| 540-CD9-H6 | 132 | 2.8 | 5.0 | 142 | 17 | 0.9 | 640 | 0.1 | 2.0 | 0.3 | 4.0 | 80 | 0.3 | 63 | 1.8 |
| 540-CD9-H7 | 994 | 3.8 | 4.6 | 797 | 20 | 0.9 | 1200 | 0.1 | 1.9 | 0.3 | 4.0 | 100 | 0.4 | 20 | 1.6 |
| 540-CD9-H8 | 27 | 2.4 | 4.8 | 178 | 19 | 0.9 | 1160 | 0.1 | 1.8 | 0.3 | 5.1 | 60 | 0.4 | 57 | 0.8 |
| 540-CD9-H10 | 935 | 1.6 | 4.8 | 29 | 27 | 1.0 | 1800 | 0.05 | 1.8 | 0.3 | 6.5 | 40 | 0.3 | 52 | 0.5 |
| 400-B26 | 87 | 12 | 5.8 | 16 | 19 | 1.1 | 550 | 0.1 | 2.9 | 0.3 | 1.2 | 60 | 0.6 | 19 | 3.7 |
| 505-B2-2 | 464 | 11 | 16 | 12 | 18 | 1.0 | 2360 | 0.4 | 4.7 | 0.3 | 1.9 | 60 | 0.5 | 90 | 1.5 |
| 505-B1-3 | 253 | 19 | 25 | 100 | 20 | 0.9 | 5640 | 3.5 | 11 | 0.3 | 27 | 32 | 0.4 | 5841 | 12 |
| 505-B1-5 | 270 | 18 | 8.6 | 36 | 47 | 1.0 | 9600 | 0.9 | 11 | 0.7 | 2.6 | 50 | 0.4 | 1012 | 9.2 |
| 505-B31 | 99 | 2.0 | 4.9 | 714 | 20 | 0.9 | 4600 | 0.05 | 1.9 | 0.4 | 1.0 | 38 | 0.5 | 55 | 2.6 |
| 505-B32 | 33 | 22 | 9.5 | 163 | 16 | 1.5 | 4920 | 0.1 | 6.1 | 0.4 | 17 | 230 | 0.5 | 93 | 15 |
| 505-B33 | 25 | 62 | 28 | 23 | 16 | 1.0 | 15000 | 0.8 | 33 | 0.7 | 15 | 230 | 0.4 | 177 | 17 |
| 505-B34-A | 85 | 2.7 | 4.7 | 882 | 18 | 1.1 | 1760 | 0.1 | 1.8 | 0.3 | 8.0 | 100 | 0.6 | 123 | 1.8 |
| 470-B402 | 33 | 3.4 | 4.5 | 23 | 18 | 1.1 | 3520 | 0.2 | 3.2 | 0.3 | 2.0 | 40 | 0.3 | 292 | 6.1 |
| Sample Avg. | 337 | 11 | 9.2 | 183 | 27 | 1.3 | 4643 | 6.4 | 8.6 | 1.1 | 4.9 | 96 | 0.3 | 2989 | 20 |
| Crustal Avg. | 8000 | 27 | 59 | 27 | 72 | 2.5 | 0.8 | 0.06 | 1.7 | 0.2 | 1.0 | 1.3 | 0.03 | 11 | 0.2 |

Crustal abundance of elements is from Rudnick and Gao (2003).

*3.1.2 Vein mineralogy and paragenesis*

The mineralized quartz veins mainly consist of quartz and sulfides, with the width typically varying from tens of centimeters to several meters (Figs. 3.3, 3.4). Quartz is the dominant gangue mineral, and makes up more than 80% of the vein volume. Sulfides make up less than 10% of the vein volume. Pyrite, molybdenite, chalcopyrite, and galena are the dominant sulfides. Gold and molybdenite often appear together on the hand specimen scale, but a direct contact of gold and molybdenite has not been observed under the microscope. Other commonly observed vein minerals are K-feldspar, covellite, bornite, anhydrite, celestine, barite, calcite, ankerite, monazite, and biotite.

Four mineralization stages are recognized (Fig. 3.8). They are, from early to late, quartz–K-feldspar stage (I), pyrite–molybdenite stage (II), sulfide–telluride–sulfosalt–gold stage (III), and carbonate–barite stage (IV). Stage I and II are molybdenite deposition stages, while stage III is the gold deposition stage.

*Quartz–K-feldspar stage (I):* The quartz-K-feldspar stage is the earliest recognized hydrothermal alteration stage (Fig. 3.8). Compact milky white quartz makes up more than 80% of the entire vein volume. Quartz shows well-developed superimposed textures, such as deformation texture (e.g., undulose extinction, subgrains, and deformation lamellae), breccia texture (Fig. 3.4C, 3.5B, C), and recrystallization texture (e.g., grain-boundary migration recrystallization, Fig. 3.6K). Rarely, stage I quartz crystals are relatively well preserved in some small cavities and unsealed veinlets. They are coarse-grained (>5 mm), sub-transparent (Fig. 3.5A), and with rough crystal faces (i.e., with many hillocks on crystal faces). Abundant minerals occur as solid phases in $H_2O$-$CO_2$ fluid inclusions in stage I quartz. They are: $Cu_{1.65}S$, covellite, chalcopyrite, bornite, molybdenite, pyrite, colusite, anhydrite, and celestine (discussed in more detail below). Except colusite, all the minerals have also been observed as mineral inclusions in stage I quartz (e.g., Fig. 3.6B) or as anhedral aggregates in stage I quartz micro-fractures (Fig. 3.6A). K-feldspar is the second most abundant gangue mineral. Aggregates of coarse-grained (>5 mm) K-feldspar occur disseminated in the veins, and are most abundant at the vein margins (Fig. 3.4A, B). Green biotite rarely occurs as fine-grained flakes (0.1–1mm) in quartz (Fig. 3.6D). Pyrite is the dominant metallic mineral. It occurs as coarse-grained cubes (>5 mm, Fig. 3.4B), which are often fractured, and subsequently filled by ore minerals of later stages (Figs. 3.6E, 3.8C, I, J). Black rutile aggregates (up to 2 mm in diameter) occur within quartz or K-feldspar. Rutile is often intergrown with molybdenite (Fig. 3.6H), and locally intergrown with monazite (Fig. 3.6C). Rutile is compositionally

inhomogeneous. It shows both patchy and oscillatory zoning (Fig. 3.6H) caused by high but variable niobium content (up to 15 wt.%).

TABLE 3.2. Selected electron microprobe data of rutile

| wt.% | $TiO_2$ | FeO[a] | $Cr_2O_3$ | $V_2O_3$ | $Nb_2O_5$ | Total |
|---|---|---|---|---|---|---|
| 1 | 70.88 | 5.72 | 0.28 | 4.35 | 19.05 | 100.28 |
| 2 | 74.76 | 4.95 | 0.16 | 4.03 | 16.03 | 99.93 |
| 3 | 80.26 | 3.47 | 0.69 | 3.38 | 12.82 | 100.62 |
| 4 | 73.28 | 4.91 | 0.24 | 4.41 | 17.75 | 100.59 |
| 5 | 75.51 | 4.46 | 0.35 | 4.12 | 17.09 | 101.53 |
| 6 | 74.71 | 3.78 | 0.21 | 4.54 | 16.60 | 99.84 |
| 7 | 69.75 | 5.43 | 0.23 | 4.37 | 20.62 | 100.40 |
| 8 | 70.29 | 5.95 | 0.21 | 3.17 | 20.01 | 99.63 |
| 9 | 70.41 | 5.87 | 0.18 | 4.15 | 20.50 | 101.11 |
| 10 | 76.62 | 4.30 | 0.21 | 3.58 | 15.34 | 100.05 |
| 11 | 70.00 | 5.33 | 0.24 | 4.42 | 19.50 | 99.49 |
| 12 | 82.65 | 2.59 | 0.54 | 3.31 | 10.86 | 99.95 |
| 13 | 72.92 | 5.32 | 0.14 | 3.54 | 18.24 | 100.16 |
| 14 | 68.28 | 5.93 | 0.19 | 4.61 | 20.13 | 99.14 |
| 15 | 75.13 | 4.49 | 0.47 | 4.22 | 15.26 | 99.57 |
| 16 | 89.72 | 1.30 | 0.84 | 2.68 | 5.90 | 100.44 |
| 17 | 91.45 | 0.87 | 0.86 | 2.34 | 4.57 | 100.09 |
| 18 | 89.35 | 1.42 | 0.57 | 2.68 | 6.21 | 100.23 |
| 19 | 87.70 | 1.79 | 0.29 | 3.14 | 7.26 | 100.18 |
| 20 | 74.88 | 5.12 | 0.22 | 3.72 | 16.86 | 100.80 |
| 21 | 76.89 | 4.92 | 0.27 | 2.88 | 14.74 | 99.70 |
| 22 | 74.36 | 5.53 | 0.35 | 3.04 | 16.46 | 99.74 |
| 23 | 75.50 | 5.19 | 0.27 | 3.40 | 16.32 | 100.68 |
| 24 | 72.01 | 4.88 | 0.20 | 5.56 | 18.50 | 101.15 |
| 25 | 87.01 | 1.86 | 0.16 | 3.73 | 7.55 | 100.31 |
| 26 | 86.98 | 1.76 | 0.16 | 3.68 | 7.12 | 99.70 |
| 27 | 87.54 | 1.73 | 0.16 | 3.66 | 7.29 | 100.38 |
| 28 | 87.32 | 1.60 | 0.14 | 3.66 | 6.99 | 99.71 |
| 29 | 87.08 | 1.56 | 0.18 | 3.62 | 7.38 | 99.82 |
| 30 | 87.34 | 1.55 | 0.18 | 3.70 | 6.79 | 99.56 |

[a] Total Fe as FeO. Analytical conditions, standards and X-ray emission lines were as follows: 15 kV and 20 nA, and $TiO_2$ for Ti*Kα*, pure metals for Fe*K*α, Cr*Kα*, Mn*Kα*, V*Kα*, W*Mα*, and Nb*Lα*. Tungsten and Mn are below the detection limits of 0.14–0.19 wt.% W and 0.04 wt.% Mn, respectively.

*Pyrite–molybdenite stage (II):* This stage is the major molybdenite deposition stage. Fine to very fine-grained (0.005–1 mm) pyrite and molybdenite fill fractures in stage I quartz (Fig. 3.4C), or occur as stage I quartz-K feldspar-pyrite breccia matrix (Figs. 3.4D, 3.5B, C). Pyrite is characterized by abundant voids and mineral inclusions (Fig. 3.6E, F, G), including molybdenite, anhydrite, celestine, and monazite. Molybdenite is commonly observed in textural equilibrium with pyrite (Fig. 3.6F) and suggests a common mineral paragenesis during

the pyrite-molybdenite stage. Galena, chalcopyrite, and tellurides (e.g., Fig. 3.6E) locally occur as micro-veinlets in stage II pyrite, suggesting that molybdenum mineralization preceded gold mineralization.

*Sulfide–telluride–sulfosalt–gold stage (III)*: The gold deposition stage is characterized by galena, pyrite, and chalcopyrite forming clusters, bands, or veinlets in the early quartz veins (Fig. 3.4E, F). Gangue minerals are rare. Quartz occasionally occurs as coarse-grained (>5mm) crystals enclosed in galena. Compared with stage I quartz crystals, stage III quartz crystals are characterized by smooth crystal surfaces and are more transparent (Fig. 3.5F). Metallic minerals include galena, pyrite, chalcopyrite, minor gold, tellurides, sulfosalts and sphalerite, and rare pyrrhotite. Pyrite occurs as fine-grained subhedral to euhedral cubes (0.1–1 mm). Pyrite of this stage contains no molybdenite inclusions and is intimately associated with gold and chalcopyrite (Fig. 3.7A, B). This distinguishes stage II and III pyrite. Chalcopyrite is intergrown with or replaced by galena (Fig. 3.7C, D), or occurs as anhedral aggregates filling pore spaces between pyrite grains (Fig. 3.7A, B). Gold occurs as free gold aggregates in quartz micro-fractures, in contact with pyrite, chalcopyrite, and galena, or along with sulfosalts and tellurides. Gold fineness ranges from 826 to 988 (Table 3.3). Sulfosalts and tellurides either occur within or marginal to galena, or fill micro-fractures in early pyrite. These minerals are often present in two types of contact assemblages, including a telluride-dominated assemblage (Fig. 3.7D–G) and a sulfosalt-dominated assemblage (Fig. 3.7H–L). Gold, wittichenite ($Cu_3BiS_3$), and tetradymite ($Bi_2Te_2S$) are present in both assemblages. The sulfosalt-dominated assemblage consists of gold, wittichenite ($Cu_3BiS_3$), tetradymite ($Bi_2Te_2S$), aikinite ($PbCuBiS_3$), lindstromite ($Pb_3Cu_3Bi_7S_{15}$), and two rare sulfosalts: kupcikite ($Cu_{3.4}Fe_{0.6}Bi_5S_{10}$) and salzburgite ($Cu_{1.6}Pb_{1.6}Bi_{6.4}S_{12}$). Kupcikite has grey reflection color and shows reflectance pleochroism. It often shows brightness variation in BSE image (Fig. 3.7K, L), resulting from the variation in Cu, Bi, and Fe contents, or the presence of Pb (Table 3.4). The telluride-dominated assemblage consists of gold, wittichenite ($Cu_3BiS_3$), altaite (PbTe), tellurobismuthite ($Bi_2Te_3$), hessite ($Ag_2Te$), petzite ($Ag_3AuTe_2$), tetradymite ($Bi_2Te_2S$), calaverite ($AuTe_2$), and a rare sulfotelluride, buckhornite ($AuPb_2BiTe_2S_3$). Galena in the telluride-dominated assemblage often contains worm-shaped voids (<10 μm, Fig. 3.7D–F), suggesting dissolution of galena under telluride-stable conditions. The most abundant telluride is altaite, followed by tellurobismuthite. Calaverite is rare, with only a few small grains (<10 μm) observed. Buckhornite occurs as anhedral grains or lath-shaped crystals up to 50 μm in length. Petzite is commonly enclosed or rimmed by altaite and tellurobismuthite (Fig. 3.7F).

*Carbonate–barite stage (IV):* This last stage marks either the waning of hydrothermal

activity or a later unrelated supergene episode. It is characterized by the deposition of calcite, ankerite, barite, and alteration products of early sulfides (e.g., cerussite) in unsealed fractures in quartz or in the matrix of porous breccias (Fig. 3.6G). Minerals of this stage are widespread but only microscopically visible in most cases.

TABLE 3.3. Selected electron microprobe data of gold

| | 1 | 2 | 3 | 4 | 5 | 6 | 7 | 8 | 9 | 10 | 11 | 12 |
|---|---|---|---|---|---|---|---|---|---|---|---|---|
| wt.% | | | | | | | | | | | | |
| Au | 83.96 | 87.98 | 94.06 | 93.85 | 98.64 | 98.85 | 99.35 | 99.66 | 96.09 | 94.97 | 95.67 | 95.73 |
| Ag | 14.04 | 10.33 | 5.24 | 5.16 | 0.92 | 0.87 | 0.80 | 0.69 | 4.38 | 4.37 | 4.43 | 4.43 |
| Fe | 1.28 | <0.07 | <0.06 | <0.07 | 0.30 | 0.23 | 0.39 | 0.25 | <0.06 | <0.06 | <0.07 | <0.06 |
| Cu | 2.21 | <0.13 | <0.13 | <0.13 | 0.13 | 0.14 | 0.15 | 0.13 | <0.13 | <0.12 | 0.14 | <0.12 |
| S | 0.17 | 0.16 | <0.09 | <0.09 | 0.14 | <0.09 | 0.12 | 0.09 | <0.09 | <0.09 | 0.11 | <0.09 |
| Bi | <0.63 | <0.66 | <0.68 | <0.70 | <0.72 | <0.71 | <0.75 | <0.71 | <0.73 | <0.77 | <0.71 | <0.72 |
| Hg | <0.58 | <0.58 | <0.58 | <0.59 | <0.59 | <0.61 | <0.59 | <0.62 | <0.60 | <0.59 | <0.59 | <0.60 |
| Te | <0.18 | <0.17 | <0.17 | <0.19 | <0.18 | <0.18 | <0.18 | <0.17 | <0.18 | <0.18 | <0.18 | <0.17 |
| Pb | <0.48 | <0.46 | <0.48 | <0.48 | <0.54 | <0.52 | <0.54 | <0.49 | <0.53 | <0.54 | <0.52 | <0.48 |
| Total | 101.66 | 98.47 | 99.30 | 99.01 | 100.13 | 100.09 | 100.81 | 100.82 | 100.47 | 99.34 | 100.35 | 100.16 |
| Fineness | 826 | 893 | 947 | 948 | 985 | 988 | 986 | 988 | 956 | 956 | 953 | 956 |

*1* gold in contact with chalcopyrite, *2–4* gold occurring as free gold aggregates in quartz micro-fractures, 5–*8* gold in sulfosalt dominated assemblage, *9–12* gold in telluride dominated assemblage. Analytical conditions, standards and X-ray emission lines were as follows: 20 kV and 40 nA, and beam size of 1 μm; pure metals for Bi*Mα*, Ag*Lα*, and Au*Lα*, PbTe for Pb*Mα* and Te*Lα*, HgS for Hg*Lα*, $CuFeS_2$ for Cu*Kα*, Fe*Kα*, and S*Kα*

TABLE 3.4. Selected electron microprobe data of tellurides and sulfosalts

| | 1 | 2 | 3 | 4 | 5 | 6 | 7 | 8 | 9 | 10 | 11 | 12 | 13 | 14 | 15 | 16 | 17 | 18 |
|---|---|---|---|---|---|---|---|---|---|---|---|---|---|---|---|---|---|---|
| wt.% | | | | | | | | | | | | | | | | | | |
| S | 16.49 | <0.07 | 8.10 | <0.08 | 19.5 | 19.12 | 19.00 | 18.38 | 0.06 | 17.29 | <0.07 | <0.07 | 0.44 | 17.48 | 17.54 | <0.06 | 4.63 | 19.07 |
| Bi | 37.00 | 1.07 | 17.12 | <0.45 | 63.3 | 65.94 | 64.05 | 61.95 | <0.29 | 55.60 | <0.36 | <0.36 | <0.42 | 61.71 | 62.21 | 51.59 | 58.34 | 42.16 |
| Ag | <0.19 | <0.18 | <0.19 | 3.28 | <0.19 | <0.21 | <0.20 | <0.21 | 60.62 | <0.20 | 48.48 | 47.89 | 40.5 | <0.21 | <0.02 | <0.18 | <0.19 | 0.73 |
| Cu | 10.53 | <0.12 | <0.12 | 0.15 | 13.43 | 14.05 | 14.23 | 11.83 | <0.13 | 6.39 | <0.13 | <0.12 | <0.13 | 4.71 | 4.56 | <0.13 | <0.12 | 35.51 |
| Te | <0.16 | 38.32 | 22.14 | 58.11 | <0.17 | <0.16 | <0.16 | <0.16 | 39.19 | <0.14 | 32.93 | 32.56 | 32.41 | <0.17 | <0.17 | 47.94 | 36.63 | <0.15 |
| Au | <0.28 | <0.28 | 16.54 | 36.83 | <0.28 | <0.28 | <0.28 | <0.28 | <0.28 | <0.28 | 17.43 | 18.55 | 24.61 | 0.63 | <0.28 | 1.44 | 1.58 | 1.14 |
| Fe | <0.07 | <0.07 | <0.07 | <0.06 | 1.83 | 0.85 | 1.69 | 1.15 | <0.07 | 0.71 | <0.07 | <0.07 | <0.07 | 1.04 | 0.79 | <0.06 | <0.07 | <0.06 |
| Pb | 35.7 | 58.97 | 36.34 | <0.36 | <0.32 | 0.46 | 0.45 | 7.15 | <0.28 | 20.80 | <0.33 | <0.32 | 2.81 | 15.63 | 15.1 | <0.31 | <0.34 | <0.29 |
| Total | 99.72 | 98.36 | 100.24 | 98.37 | 98.06 | 100.42 | 99.42 | 100.46 | 99.87 | 100.79 | 98.84 | 99.00 | 100.77 | 101.20 | 100.20 | 100.97 | 101.18 | 98.61 |
| apfu | | | | | | | | | | | | | | | | | | |
| S | 2.998 | – | 2.963 | – | 10.003 | 9.849 | 9.744 | 9.804 | – | 14.818 | – | – | 0.105 | 11.638 | 11.775 | – | 1.005 | 3.044 |
| Bi | 1.032 | 0.017 | 0.961 | – | 4.982 | 5.212 | 5.040 | 5.070 | – | 7.311 | – | – | – | 6.304 | 6.408 | 1.960 | 1.942 | 1.032 |
| Ag | – | – | – | 0.135 | – | – | – | – | 1.940 | – | 3.388 | 3.358 | 2.882 | – | – | – | – | 0.035 |
| Cu | 0.966 | – | – | 0.010 | 3.476 | 3.652 | 3.682 | 3.184 | – | 2.763 | – | – | – | 1.582 | 1.545 | – | – | 2.860 |
| Te | – | 1.018 | 2.035 | 2.024 | – | – | – | – | 1.060 | – | 1.945 | 1.930 | 1.950 | – | – | 2.982 | 1.997 | – |
| Au | – | – | 0.985 | 0.831 | – | – | – | – | – | – | 0.667 | 0.712 | 0.959 | 0.068 | – | 0.058 | 0.056 | 0.030 |
| Fe | – | – | – | – | 0.539 | 0.251 | 0.498 | 0.352 | – | 0.349 | – | – | – | 0.398 | 0.305 | – | – | – |
| Pb | 1.004 | 0.965 | 2.057 | – | – | 0.037 | 0.036 | 0.590 | – | 2.759 | – | – | 0.104 | 1.610 | 1.569 | – | – | – |
| Total | 6 | 2 | 9 | 3 | 19 | 19 | 19 | 19 | 3 | 28 | 6 | 6 | 6 | 21.6 | 21.6 | 5 | 5 | 7 |

*1* aikinite, *2* altaite, *3* buckhornite, *4* calaverite, *5–8* kupcikite, *9* hessite, *10* lindstromite, *11–13* petzite, *14–15* salzburgite, *16* tellurobismuthite, *17* tetradymite, *18* wittichenite. Petzite analysis gave a lower Au content (17.4–24.6 wt%) than ideal petzite (25.4 wt%), most likely resulting from diffusion of Au away from the electron beam during microprobe analysis (Rucklidge and Stumpfl, 1968). Because petzite has low electrical conductivity, under electron bombardment in the microprobe, it develops an electric filed gradient up which Au diffuses rapidly and is replaced by Ag. Analytical conditions, standards and X-ray emission lines were as follows: 20 kV and 20 nA, and beam size of 1μm; pure metals for Bi*Mα*, Ag*Lα*, Au*Lα*, and Cu*Kα*, PbTe for Pb*Mα* and Te*Lα*, $FeS_2$ for Fe*Kα* and S*Kα*. Abbrevation: apfu = atoms per formula unit

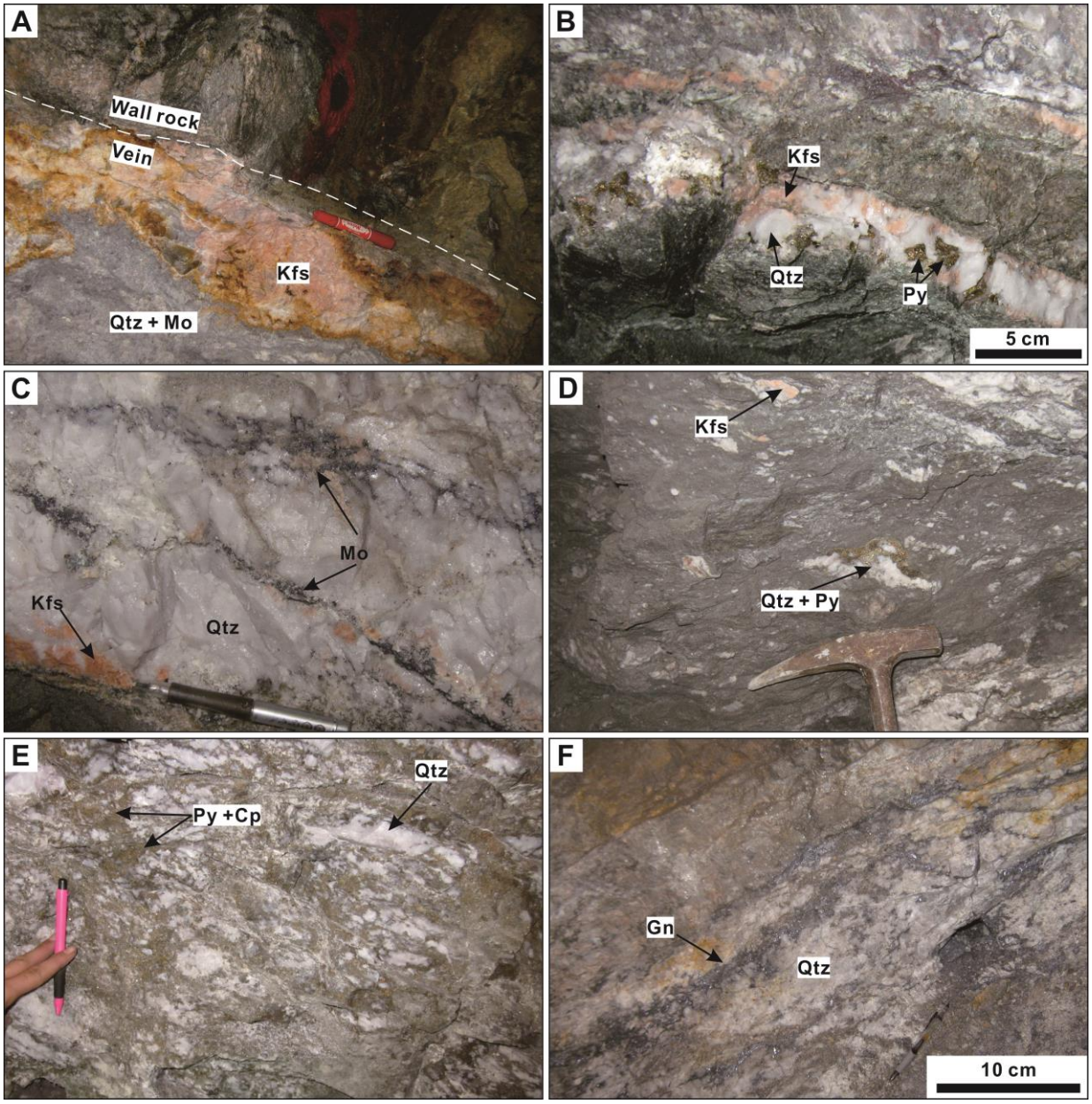


FIG. 3.4. Photos of underground exposures showing vein mineralogy and fabrics. **A**. Molybdenum mineralized thick quartz–K-feldspar vein with abundant K-feldspar in the vein margin. F35/470 m. **B**. Molybdenum mineralized quartz–K-feldspar veinlet with coarse-grained stage I pyrite cubes. F7/540 m. **C**. Molybdenite filling fractures in stage I quartz. F35/505 m. **D**. Molybdenum ore with breccia texture. Fragments consist of stage I quartz, pyrite, and K-feldspar. Matrix is composed of stage II pyrite and molybdenite, smaller stage I quartz fragments, recrystallized quartz, and stage IV carbonates and barite. F7/470 m. **E**. Gold mineralized quartz vein composed of stage I quartz, and clusters of stage III pyrite and chalcopyrite. F7/365 m. **F**. Gold mineralized quartz vein composed of stage I quartz, and galena dominated bands and veinlets (stage III). F5/540 m. Abbreviations: Cp = chalcopyrite, Gn = galena, Kfs = K-feldspar, Mo = molybdenite, Py = pyrite, Qtz = quartz.

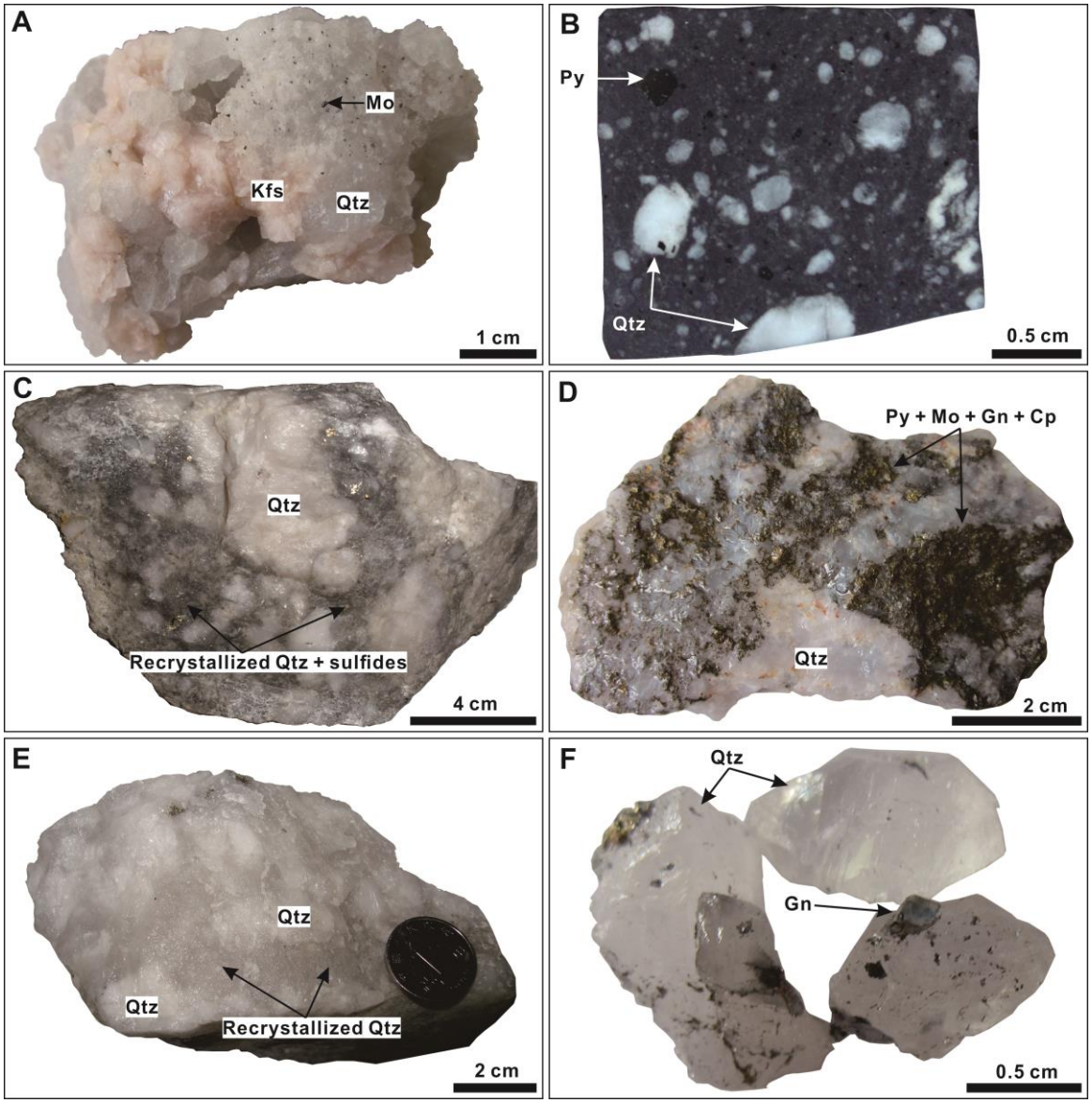


FIG. 3.5. Photos of hand specimens showing vein mineralogy and fabrics. **A**. Contact assemblage of K-feldspar and weakly deformed stage I quartz. Note abundant molybdenite disseminations both within and at the surface of quartz crystals. Sample DH-540-2/540 m. **B**. Brecciated molybdenum ore. Fragments consist of stage I quartz. Matrix is composed of stage II pyrite and molybdenite, smaller stage I quartz fragments, recrystallized quartz, and stage IV carbonates and barite. Sample 505-B18/505 m, cf. Figure 3.6 E, G as back-scattered electron (BSE) image. **C**. Brecciated molybdenum ore composed of stage I quartz fragments and glassy grey matrix consisting of recrystallized quartz and very fine-grained pyrite and molybdenite. Sample 505-B1-4/505 m, cf. Figure 3.6 F, K as photomicrograph. **D**. Gold-molybdenum ore composed of stage I quartz, pyrite, molybdenite, chalcopyrite, galena, and minor gold. **E**. Quartz aggregate in gold ore composed of stage I quartz fragments and recrystallized quartz. Note recrystallized quartz is cleaner and more transparent than larger quartz fragments. Sample 540-CD9-B2/540 m, cf. Figure 3.6J as photomicrograph. **F**. Stage III quartz crystals in contact with galena. Sample 470-f7-13/470 m. Abbreviations: Cp = chalcopyrite, Gn = galena, Kfs = K-feldspar, Mo = molybdenite, Py = pyrite, Qtz = quartz.

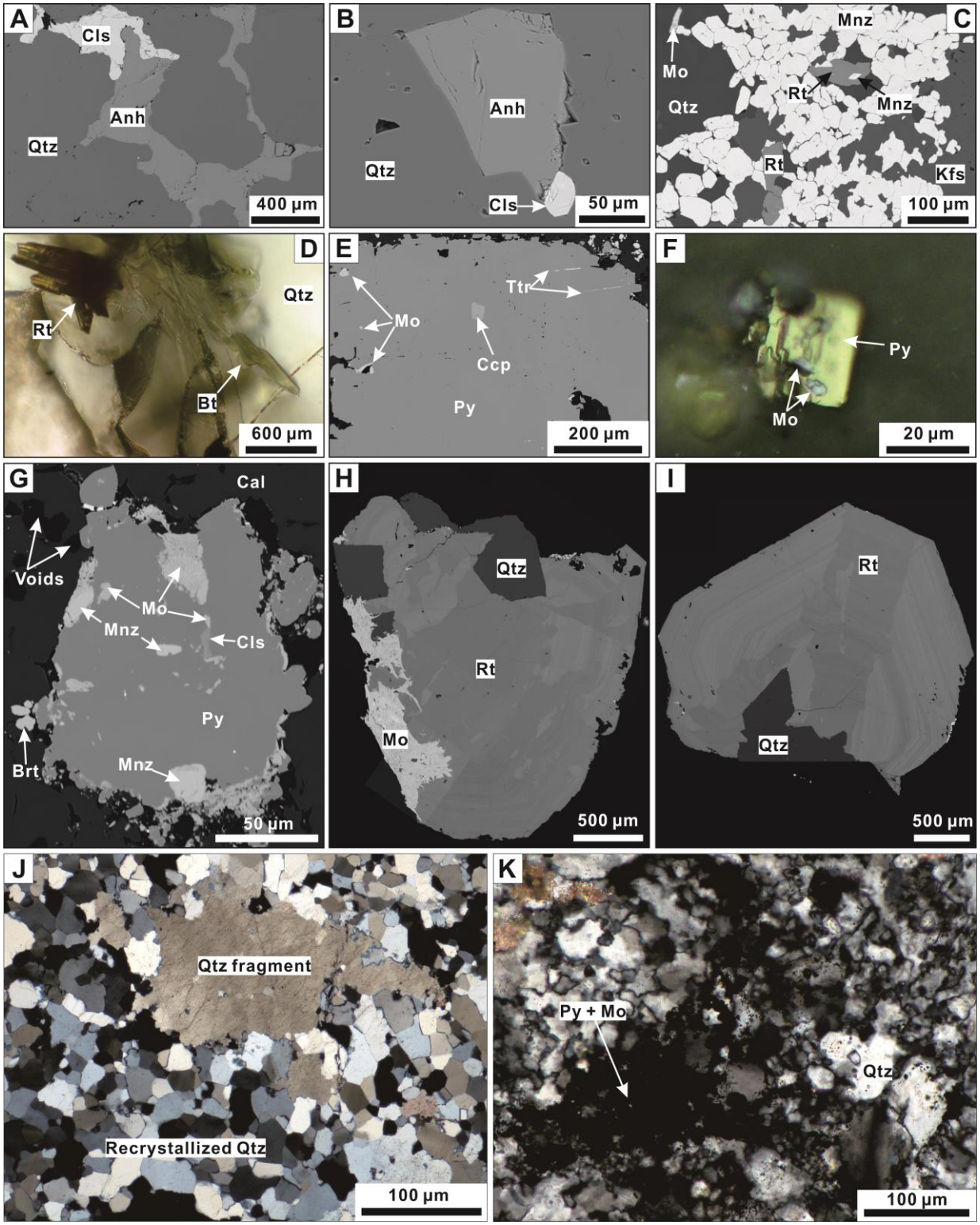


FIG. 3.6. Photomicrographs and BSE images of vein minerals and molybdenum ores. **A**. Aggregate of anhydrite and celestine in stage I quartz micro-fracture. Sample LS-540-3/540 m, BSE image. **B**. Anhydrite and celestine occurring as mineral inclusions in stage I quartz. Sample LS-540-3/540 m, BSE image. **C**. Monazite, rutile, and molybdenite in stage I quartz. Sample YM-540-B7/540 m, BSE image. **D**. Rutile and green biotite in stage I quartz. Sample DH-540-3/540 m, plane-polarized transmitted light. **E**. Stage II pyrite in the matrix of breccia molybdenum ore. Pyrite contains molybdenite inclusions, and

is cut by later tetradymite. Sample 505-B18/505 m, BSE image, cf. Figure 3.5B as hand specimen. **F**. Molybdenite flakes enclosed by stage II pyrite. Sample 505-B1-4/505 m, plane-polarized reflected light, oil immersion, cf. Figure 3.5C as hand specimen. **G**. Stage II pyrite in the matrix of breccia Mo ore. Pyrite contains inclusions of molybdenite, monazite, and celestine, and is enclosed by later calcite and barite. Sample 505-B18/505 m, BSE image, cf. Figure 3.5B as hand specimen. **H**. Intergrowth of rutile and molybdenite. Rutile is compositionally inhomogeneous and shows patchy and oscillatory zoning. Sample LS-505-9/505 m, BSE image. **I**. Rutile grain shows distinct oscillatory zoning. Sample LS-505-9/505 m, BSE image. **J**. Quartz dominated matrix of breccia molybdenum ore. The matrix is composed of recrystallized quartz with highly serrated grain boundaries, and very fine-grained pyrite and molybdenite. Sample 505-B1-4/505 m, plane-polarized transmitted light, cf. Figure 6I as hand specimen. **K**. Quartz aggregate in gold ore composed of stage I quartz fragments and recrystallized quartz. Note the large quartz fragment in the central top has a dirty appearance caused by abundant tiny fluid inclusions, while recrystallized quartz shows a much cleaner appearance. Sample 540-CD9-B2/540 m, plane-polarized transmitted light, cf. Figure 3.5E as hand specimen. Abbreviations: Anh = anhydrite, Brt = barite, Bt = biotite, Cal = calcite, Cls = celestine, Cp = chalcopyrite, Kfs = K-feldspar, Mnz = monazite, Mo = molybdenite, Py = pyrite, Qtz = quartz, Rt = Rutile, Ttr = tetradymite.

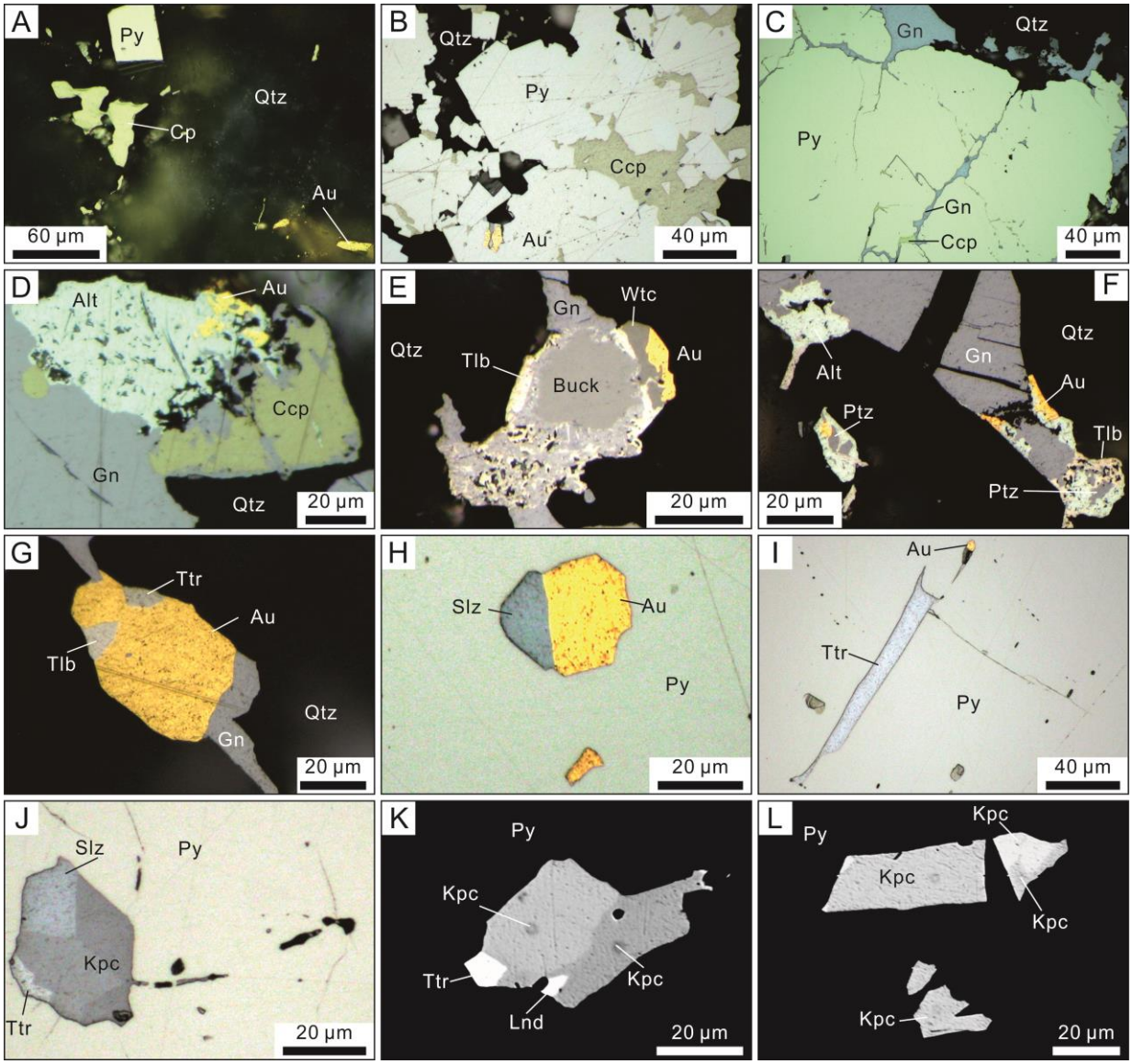


FIG. 3.7. Photomicrographs (A–J, plane-polarized reflected light, oil immersion) and BSE images (K–L) of gold ore samples. **A**. Stage III pyrite, chalcopyrite, and gold in quartz micro-fractures. Sample 400-13-2/400 m. **B**. Anhedral aggregates of chalcopyrite filling pore spaces between stage III pyrite grains. Gold occurs in contact with pyrite. Sample LS-365-1/365 m. **C**. Galena and chalcopyrite filling micro-fractures in stage I pyrite Sample 540-18/540 m. **D**. Porous aggregate of altaite and gold in contact with galena and chalcopyrite. Chalcopyrite is corroded and replaced by galena. Sample 400-10/400 m. **E**. Porous aggregate of buckhornite, wittichenite, tellurobismuthite, and gold. Sample 400-10/400 m. **F**. Porous aggregates of altaite, tellurobismuthite, gold, and petzite. Sample 400-10/400 m. **G**. Aggregate of gold, tellurobismuthite, and tetradymite. Sample 400-10/400 m. **H**. Aggregate of gold and salzburgite in a healed micro-fracture in stage I pyrite. Sample LS-505-10/505 m. **I**. Tetradymite and gold in a micro-fracture in stage I pyrite. Sample LS-505-10/505 m. **J**. Aggregate of kupcikite (with reflectance pleochroism), salzburgite, and tetradymite in a healed micro-fracture in stage I pyrite. Sample LS-505-10/505 m. **K**. Aggregate of kupcikite, tetradymite, and lindstromite. Kupcikite shows contrast brightness. Sample LS-505-10/505 m. **L**. Kupcikite with contrast brightness

in BSE image. Sample LS-505-10/505 m. Abbreviations: Alt = altaite, Au = gold, Buck = buckhornite, Cp = chalcopyrite, Gn = galena, Kpc = kupcikite, Lnd = lindstromite, Ptz = petzite, Py = pyrite, Slz = salzburgite, Tlb = tellurobismuthite, Ttr = tetradymite, Wtc = wittichenite.

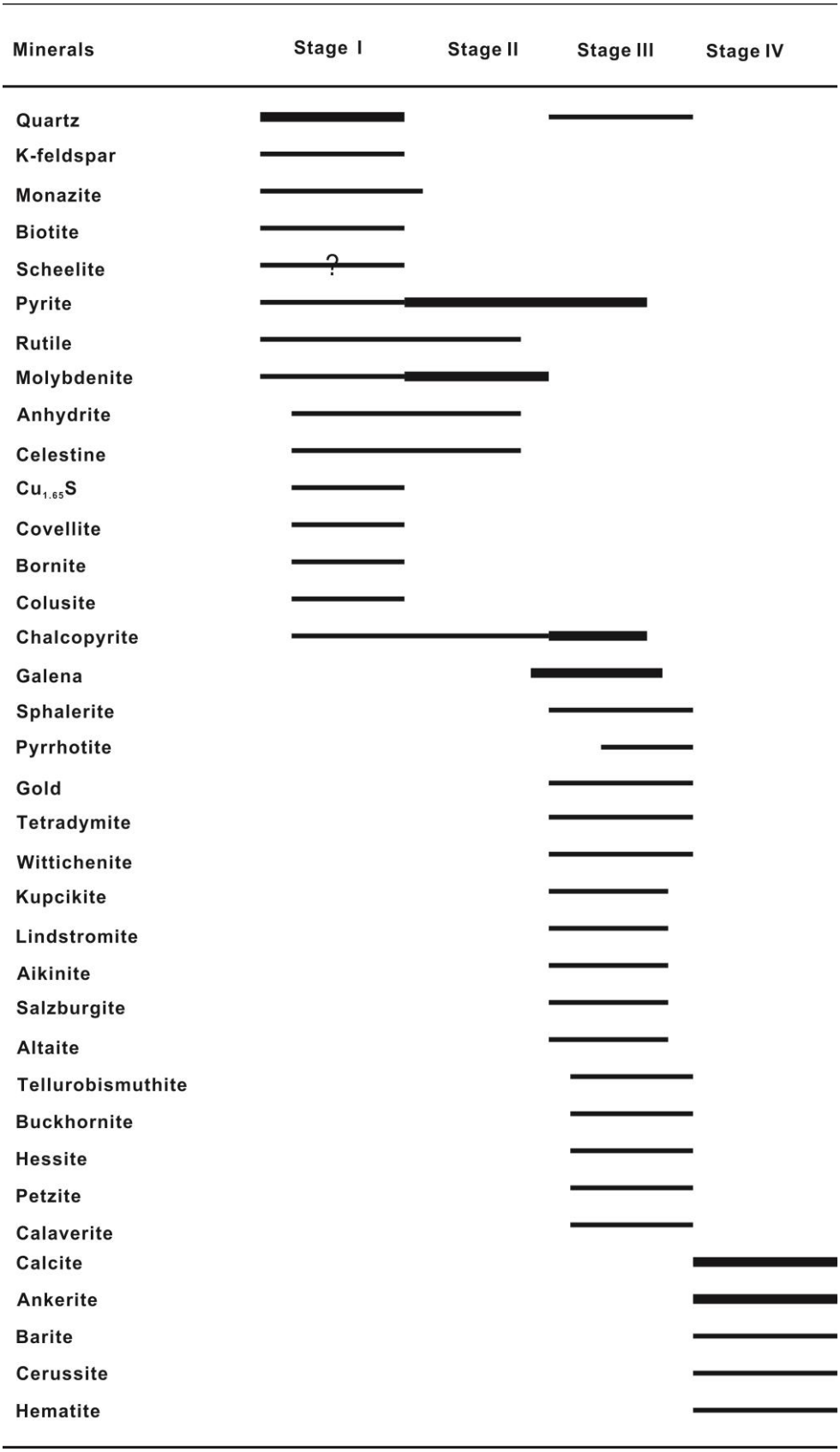


FIG. 3.8. Paragenetic sequence of vein minerals of the Dahu Au-Mo deposit.

## 3.2 Fluid inclusion studies

### *3.2.1 Sample material and analytical techniques*

Quartz from stage I and stage III was collected for fluid inclusion research. Over thirty-two polished thick sections and one polished section were examined under the microscope. Of these, fifteen polished thick sections were selected to carry out microthermometric measurements, eleven polished thick sections were selected to carry out Raman spectroscopic analysis, and three were selected to carry out ultraviolet femtosecond laser ablation-inductively coupled plasma-mass spectrometry (Uv-Fs-LA-ICP-MS) analysis.

Raman spectroscopic analyses were carried out at China University of Geosciences (Beijing). Raman spectroscopic analyses were carried out with a Reinishaw invia Raman scanning spectrometer, operating with an excitation wavelength of $\lambda$ = 514.5 nm. Fluid inclusion microthermometric measurements were carried out at Clausthal University of Technology and China University of Geosciences (Beijing). Fluid inclusion microthermometry data were obtained on a Linkam THMS 600 heating-freezing stage (in Germany) and Linkam MDS 600 heating-freezing stage (in China). The stage enables measurements within the range of -196 to 600 ℃. Freezing and heating runs were undertaken using liquid nitrogen and a thermal resistor, respectively. $CO_2$-$H_2O$ clathrate melting temperatures obtained by microthermometry were used to calculate the NaCl equivalent values, which were subsequently used to calculate Na concentrations in individual fluid inclusions after been corrected for the contributions of KCl. The concentrations of Na were then used as an internal standard to transform the element ratios measured by Uv-fs-LA-ICP-MS into absolute concentrations through the SILLS software (Guillong et al., 2008).

Ultraviolet femtosecond laser ablation-inductively coupled plasma-mass spectrometry (Uv-fs-LA-ICP-MS) was carried out at University of Hannover, Germany. Details on the instrumentation and analytical procedure can be found in Albrecht et al. (2004), and are briefly summarized below. Uv-fs-LA-ICP-MS analysis was processed with an Element XRTM fast scanning sector field inductively coupled plasma mass spectrometer in combination with an in-house built laser ablation system which is based on a Spectra-PhysicsTM femtosecond laser operating in the deep UV at 194 nm. The laser system produces pulse energy of 70–90 μJ in the fourth harmonic. This ultra-short pulsed laser generates a soft ablation with high control and avoids elemental fractionation at the sample site.

Quartz chips and standard reference materials were placed in a modified heating-freezing

stage cell, which enables laser ablation to be performed at low temperature. Fluid inclusions were first quickly frozen to a temperature of -110 ℃, and then laser ablation was performed at -80 ℃, which is below $CO_2$ triple point (-56.6 ℃) and $CO_2$ sublimation point at 1 atm (-78.5 ℃). The selected beam size is bigger than the analyzed fluid inclusion to guarantee that the whole fluid inclusion is ablated and subsequently transported to the ICP-MS. The beam size was held constant during the analysis. The ablation of the standard reference materials (NIST 610) was carried out with a repetition rate of 10 Hz. For fluid inclusions located less than 30 μm beneath sample surface, a repetition rate of 2 to 5 Hz was used. Fluid inclusions deeper than 30 μm were analyzed with 10 Hz for faster drilling. Sample surface is pre-ablation cleaned by a few shots with a repetition rate of 2 Hz.

Seventy-six $H_2O$-$CO_2$ fluid inclusions, covering a size range between 13 and 29 μm and a depth range between 5 and 100 μm, have been successfully analysed. The concentrations of 18 elements (Li, B, Na, K, Mn, Fe, Cu, Zn, Rb, Sr, Mo, Ag, Te, Cs, Ba, Au, Pb, and Bi) were measured in each individual fluid inclusion. Si was used as the matrix-only tracer. Dwell time for Au is 10 ms for sample 470-F7-13A and 470-F7-13D, and 3 ms for sample DH-505-8. For all other elements, dwell time is 3 ms. Sweep time for sample DH-505-8 is 504–505 ms, for sample 470-F7-13A and 470-F7-13D is 532–533 ms.

### *3.2.1 Fluid inclusion types and distributions*

Two different types of fluid inclusions are distinguished: $H_2O$-$CO_2$ fluid inclusions (Type 1) and $H_2O$ fluid inclusions (Type 2) (Figs.3.9–3.11). Volatile components other than $H_2O$ and $CO_2$ were not detected by Raman spectroscopy (Fig. 3.12). Type 1 $H_2O$-$CO_2$ fluid inclusions are the dominant fluid inclusion type in stage I and stage III quartz. They have multiphase composition (liquid $H_2O$ + liquid $CO_2$ ± vapor $CO_2$ ± solids) at room temperature, and vary from negative crystal shape to highly irregular shape (Figs.3.9–3.11). Their $CO_2/(CO_2 + H_2O)$ volume ratios range from 0.05 to >0.9, with the greatest frequency at 0.1 to 0.4. $H_2O$-$CO_2$ fluid inclusions occur as planar groups outlining healed fractures that come to the surface of quartz crystals or terminate within quartz crystals (Figs. 3.9A, 3.10, 3.11) but also in a random, three-dimensional distribution within quartz crystals (Fig. 3.9A). Type 2 fluid inclusions are two phase (liquid $H_2O$ + vapor $H_2O$) aqueous fluid inclusions, with a flat shape and a vapor bubble occupying less than 10% of the fluid inclusion volume (Fig. 3.10A, B). They all occur in planar groups, which locally cut the $H_2O$-$CO_2$ fluid inclusion planes (Fig. 3.10A, B).

*3.2.2 Solid phases in $H_2O$-$CO_2$ fluid inclusions*

Microscopic examination, combined with electron microprobe analysis of solids in opened fluid inclusions, reveals the presence of $Cu_{1.65}S$, covellite, chalcopyrite, bornite, molybdenite, pyrite, colusite, anhydrite, and celestine in $H_2O$-$CO_2$ fluid inclusions in stage I quartz (Figs. 3.9, 3.13). Solids are rare in $H_2O$-$CO_2$ fluid inclusions in stage III quartz; several opaque solids, probably sulfides, were observed (Fig. 3.11C, D). The large solid/fluid ratio, and the occasional rather than universal presence of solids in fluid inclusions, suggest that these solids were accidently trapped together with the fluids, rather than precipitated from the fluids after trapping (i.e., not daughter minerals). For example, based on the current solid/fluid ratio, if the solids present in Figure 3.9 were daughter minerals that precipitated from the fluids after trapping, the fluids would have dissolved several to tens of weight percent of sulfides and/or sulfates during the time of trapping. This is highly unrealistic.

A copper sulfide, $Cu_{1.65}S$, is the most abundant sulfide in opened fluid inclusions. $Cu_{1.65}S$ contains 61–63 atomic % Cu, 37–38 atomic % S, and <1 atomic % Fe, yielding $(Cu,Fe)_{1.65}S$, or simply $Cu_{1.65}S$ (Table 3.5, 3.6). Although the (Cu + Fe)/S ratio is about 0.1 lower than that of digenite, the crystal shape (e.g., Donnay et al., 1958), mineral association (e.g., Barton, 1973; Fleet, 2006; Grguric et al., 2000), and optical properties of $Cu_{1.65}S$ all resemble digenite. $Cu_{1.65}S$ occurs as pseudo-hexagonal flakes or subhedral grains up to 50 μm in diameter. The exposed $Cu_{1.65}S$ shows bluish grey reflection color, without discernible reflectance pleochroism or anisotropy. Its reflectance is higher than covellite, but lower than chalcopyrite. Locally, $Cu_{1.65}S$ is intergrown with covellite (Fig. 3.13F–H), bornite (Fig. 3.13J), or molybdenite (Fig. 3.13C), contains bornite exsolutions (Fig. 3.13I), carries a colusite core (Fig. 3.13K), or occurs in the same fluid inclusion with anhydrite (Figs. 3.13A). Several $Cu_{1.65}S$ grains were partially altered by a deep blue phase (Fig. 3.13L). This phase occurs as small spots or veinlets in $Cu_{1.65}S$, and shows reflectance pleochroism.

Covellite is the second most abundant sulfide in opened fluid inclusions (Figs. 3.13B, E–H). It occurs as euhedral hexagonal flakes up to 50 μm in diameter. Exposed covellite shows strong anisotropy (orange) and distinct reflectance pleochroism, with reflection colors varying from purplish red to light blue in oil, or deep blue to light blue in air. Chalcopyrite is present in several opened fluid inclusions (e.g., Fig. 3.13D). Molybdenite and pyrite only occur in one opened fluid inclusion, respectively. Molybdenite occurs in contact with $Cu_{1.65}S$ and covellite (Fig. 3.13C). Pyrite occurs in contact with a covellite flake (Fig. 3.13E). Colusite ($Cu_{26}V_2(As,Sn,Sb)_6S_{32}$) is the only sulfosalt observed in fluid inclusions. It is yellowish brown

in reflected light, without discernible reflectance pleochroism or anisotropy (Fig. 3.13K).

Sulfates including anhydrite and celestine are common in the fluid inclusions (Fig. 3.13A–B, Table 3.7). They often appear in the same fluid inclusion, with anhydrite occurring as larger cuboids or elongated grains whereas celestine occurs as smaller grains in contact with anhydrite.

TABLE 3.5. Electron microprobe data of sulfides in Figure 3.13

| | 1 | 2 | 3 | 4 | 5 |
|---|---|---|---|---|---|
| wt.% | | | | | |
| S | 23.46 | 22.66 | 23.35 | 33.04 | 26.81 |
| Cu | 74.53 | 74.62 | 76.14 | 65.85 | 61.51 |
| Fe | 0.67 | 0.8 | 0.75 | 0.08 | 10.97 |
| Total | 98.66 | 98.08 | 100.24 | 98.97 | 99.29 |
| apfu | | | | | |
| S | 1.012 | 0.988 | 0.995 | 0.996 | 4.180 |
| Cu | 1.622 | 1.642 | 1.637 | 1.002 | 4.839 |
| Fe | 0.017 | 0.020 | 0.018 | 0.001 | 0.982 |
| Total | 2.65 | 2.65 | 2.65 | 2.00 | 10.00 |

*1–3* $Cu_{1.65}S$, *4* covellite, *5* bornite. Analytical conditions, standards and X-ray emission lines were as follows: 20 kV and 40 nA, and beam size of 1μm; $CuFeS_2$ for Cu*Kα*, Fe*Kα*, and S*Kα*. Abbrevation: apfu = atoms per formula unit

TABLE 3.6. Selected electron microprobe data of $Cu_{1.65}S$

| | Weight% | | | | Atomic ratio | |
|---|---|---|---|---|---|---|
| | S | Fe | Cu | Total | Cu/S | (Cu+Fe)/S |
| 1 | 23.62 | 0.84 | 75.27 | 99.73 | 1.61 | 1.63 |
| 2 | 22.77 | <0.04 | 75.54 | 98.31 | 1.67 | 1.67 |
| 3 | 23.07 | 0.74 | 74.90 | 98.71 | 1.64 | 1.66 |
| 4 | 22.90 | <0.04 | 75.52 | 98.42 | 1.66 | 1.66 |
| 5 | 23.35 | 0.75 | 76.14 | 100.24 | 1.65 | 1.66 |
| 6 | 23.48 | 0.42 | 75.74 | 99.64 | 1.63 | 1.64 |
| 7 | 23.09 | 0.71 | 75.62 | 99.42 | 1.65 | 1.67 |
| 8 | 23.17 | 0.54 | 75.02 | 98.73 | 1.63 | 1.65 |
| 9 | 23.20 | 0.30 | 74.66 | 98.16 | 1.62 | 1.63 |
| 10 | 23.38 | 0.34 | 74.92 | 98.64 | 1.62 | 1.63 |
| 11 | 23.17 | 0.49 | 75.43 | 99.09 | 1.64 | 1.65 |
| 12 | 23.12 | <0.04 | 75.62 | 98.74 | 1.65 | 1.65 |
| 13 | 23.51 | 0.15 | 75.70 | 99.36 | 1.62 | 1.63 |
| 14 | 23.37 | 0.65 | 74.17 | 98.19 | 1.60 | 1.62 |
| 15 | 23.01 | 0.63 | 75.31 | 98.95 | 1.65 | 1.67 |
| 16 | 23.46 | 0.67 | 74.53 | 98.66 | 1.60 | 1.62 |
| 17 | 23.32 | 0.67 | 74.42 | 98.41 | 1.61 | 1.63 |
| 18 | 23.28 | 0.63 | 74.29 | 98.20 | 1.61 | 1.63 |
| 19 | 23.51 | 0.23 | 75.17 | 98.91 | 1.62 | 1.62 |
| 20 | 23.11 | <0.03 | 75.63 | 98.74 | 1.65 | 1.65 |
| 21 | 23.16 | <0.04 | 75.67 | 98.83 | 1.65 | 1.65 |
| 22 | 22.97 | 0.08 | 75.53 | 98.58 | 1.66 | 1.66 |
| 23 | 23.13 | <0.03 | 75.48 | 98.61 | 1.65 | 1.65 |
| 24 | 23.40 | 0.84 | 75.14 | 99.38 | 1.62 | 1.64 |
| 25 | 23.31 | 0.87 | 75.69 | 99.87 | 1.64 | 1.66 |
| 26 | 23.27 | 0.86 | 75.16 | 99.29 | 1.63 | 1.65 |
| 27 | 23.19 | 0.83 | 75.90 | 99.92 | 1.65 | 1.67 |
| 28 | 22.97 | 0.71 | 76.30 | 99.98 | 1.68 | 1.69 |
| 29 | 22.96 | 0.53 | 76.60 | 100.09 | 1.68 | 1.70 |
| 30 | 22.93 | 0.73 | 75.91 | 99.57 | 1.67 | 1.69 |
| 31 | 22.66 | 0.80 | 74.62 | 98.08 | 1.66 | 1.68 |
| 32 | 23.12 | 0.55 | 74.46 | 98.13 | 1.63 | 1.64 |
| 33 | 23.43 | 0.76 | 74.16 | 98.35 | 1.60 | 1.62 |
| 34 | 22.99 | 0.83 | 74.73 | 98.55 | 1.64 | 1.66 |
| avg. | 23.19 | 0.61 | 75.26 | 98.96 | 1.64 | 1.65 |

Analytical conditions, standards and X-ray emission lines were as follows: 20 kV and 40 nA, and beam size of 1μm; $CuFeS_2$ for Cu*Kα*, Fe*Kα*, and S*Kα*

TABLE 3.7. Selected electron microprobe data of anhydrite and celestine

| | 1 | 2 | 3 | 4 | 5 | 6 | 7 | 8 | 9 |
|---|---|---|---|---|---|---|---|---|---|
| wt.% | | | | | | | | | |
| CaO | 39.70 | 42.25 | 43.91 | 0.32 | 0.36 | 0.38 | 0.76 | 0.78 | 0.81 |
| SrO | 2.01 | 1.81 | 1.14 | 49.81 | 46.39 | 48.67 | 57.79 | 37.11 | 55.01 |
| BaO | <0.13 | <0.12 | <0.12 | 9.60 | 12.59 | 10.32 | <0.15 | 22.90 | 1.87 |
| $SO_3$ | 56.61 | 54.43 | 52.99 | 40.38 | 39.20 | 41.10 | 41.48 | 39.38 | 42.22 |
| Total | 98.32 | 98.49 | 98.04 | 100.11 | 98.55 | 100.47 | 100.03 | 100.17 | 99.91 |

*1–3* anhydrite, *4–9* celestine. Analytical conditions, standards and X-ray emission lines were as follows: 15 kV and 20 nA, $BaSO_4$ for Ba*Lα* and S*Kα*, $SrSO_4$ for Sr*Lα* and S*Kα*, $Ca_{10}(PO_4)_6(F)_2$ for Ca*Kα*

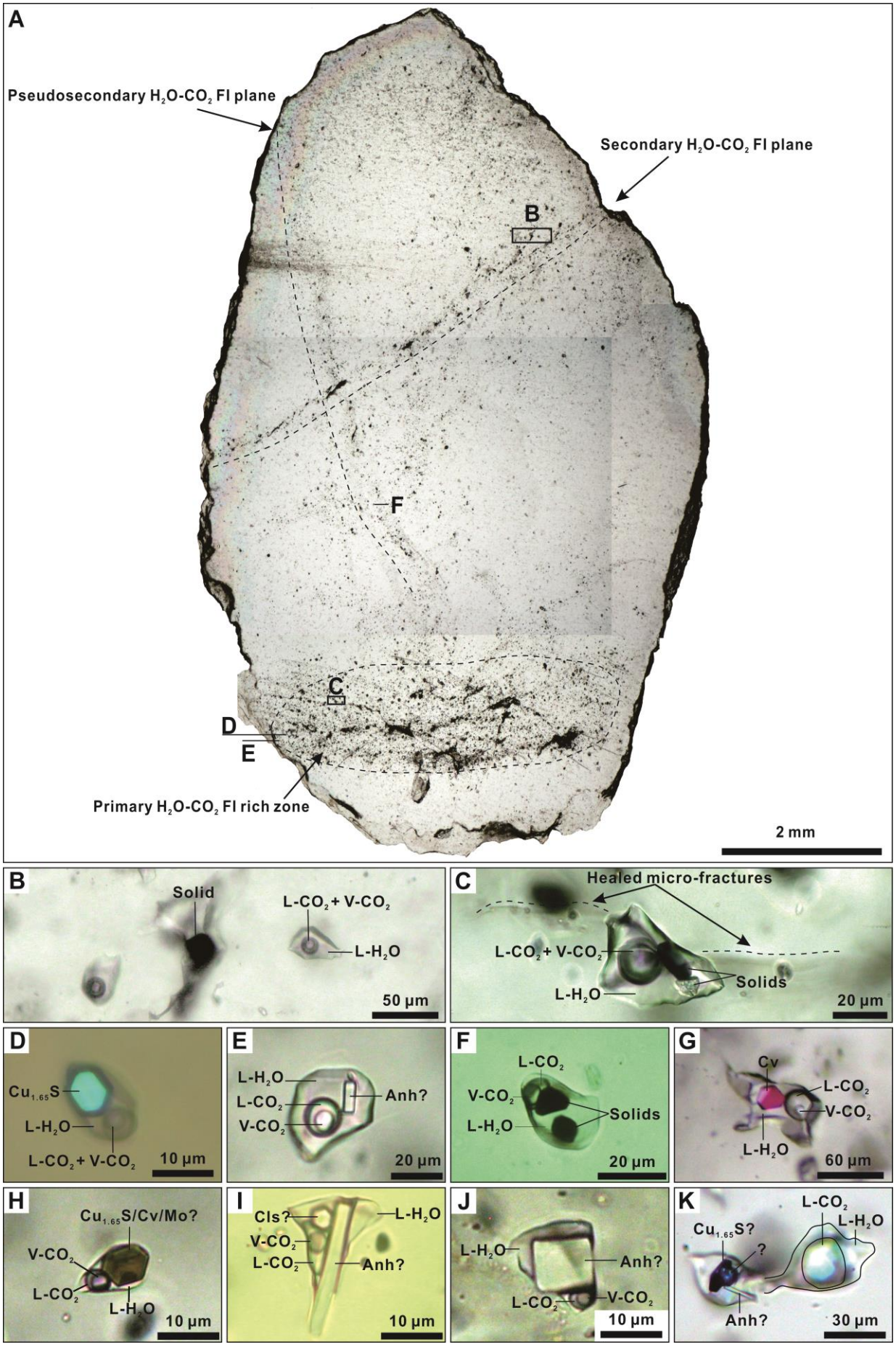
A
Pseudosecondary H2O-CO2 FI plane
Secondary H2O-CO2 FI plane
B
F
C
D
E
Primary H2O-CO2 FI rich zone
2 mm
B
Solid
L-CO2 + V-CO2
L-H2O
50 μm
C
Healed micro-fractures
L-CO2 + V-CO2
L-H2O
Solids
20 μm
D
Cu1.65S
L-H2O
L-CO2 + V-CO2
10 μm
E
L-H2O
L-CO2
V-CO2
Anh?
20 μm
F
L-CO2
V-CO2
L-H2O
Solids
20 μm
G
Cv
L-CO2
V-CO2
L-H2O
60 μm
H
Cu1.65S/Cv/Mo?
V-CO2
L-CO2
L-H2O
10 μm
I
Cls?
L-H2O
V-CO2
L-CO2
Anh?
10 μm
J
L-H2O
Anh?
L-CO2
V-CO2
10 μm
K
L-CO2
L-H2O
Cu1.65S?
?
Anh?
30 μm

FIG. 3.9. Fluid inclusions in stage I quartz. Photomicrograph D, G, and J were taken in double-polarized reflected light with quartz in extinction position; others were taken in plane-polarized transmitted light. **A**. Distribution of fluid inclusions in a stage I quartz crystal. Areas indicated by letters are detailed in B–F. Sample DH-505-8/505 m. **B**. $H_2O$-$CO_2$ fluid inclusions in a secondary fluid inclusion plane. The black spot in the center is an opaque solid in a $H_2O$-$CO_2$ fluid inclusion which is out of focus in this picture. **C**. $H_2O$-$CO_2$ fluid inclusion with re-equilibration texture (i.e., healed micro-fractures, arrowed) containing an opaque solid with hexagonal flake shape, and an angular transparent solid. **D**. $H_2O$-$CO_2$ fluid inclusion containing a bluish opaque solid with hexagonal flake shape. This solid resembles $Cu_{1.65}S$. **E**. $H_2O$-$CO_2$ fluid inclusion containing an elongated transparent solid. This solid resembles the elongated crystal habit of anhydrite. **F**. $H_2O$-$CO_2$ fluid inclusion containing two opaque solids. The two solids display greenish reflection color and triangular cross section in double-polarized reflected light. **G**. $H_2O$-$CO_2$ fluid inclusion containing a pinkish opaque solid with hexagonal flake shape. This solid resembles covellite. Sample LS-540-3/540 m. **H**. $H_2O$-$CO_2$ fluid inclusion containing a translucent greenish brown solid with hexagonal flake shape. It is likely a very thin flake of copper sulfide or molybdenite. Sample DH-540-3/540 m. **I**. $H_2O$-$CO_2$ fluid inclusion containing two transparent solids. Both solids show birefringence in double-polarized transmitted light. The one with hexagonal cross section resembles celestine, and the other resembles the elongated crystal habit of anhydrite. Sample DH-540-3/540 m. **J**. $H_2O$-$CO_2$ fluid inclusion containing a transparent solid with rectangular cross section and birefringence. This solid resembles the orthorhombic crystal shape of anhydrite. Sample DH-540-3/540 m. **K**. $H_2O$-$CO_2$ fluid inclusion containing an opaque solid with hexagonal flake shape, an opaque solid with irregular shape, and a transparent solid with elongated shape. This fluid inclusion shows evidence of necking down, with the left part and the right part (out of focus and indicated by lines) connected by a thin tube. Sample LS-540-3/540 m. Abbreviations: Anh = anhydrite, Cls = celestine, Cv = chalcopyrite, FI = fluid inclusion, Mo = molybdenite.

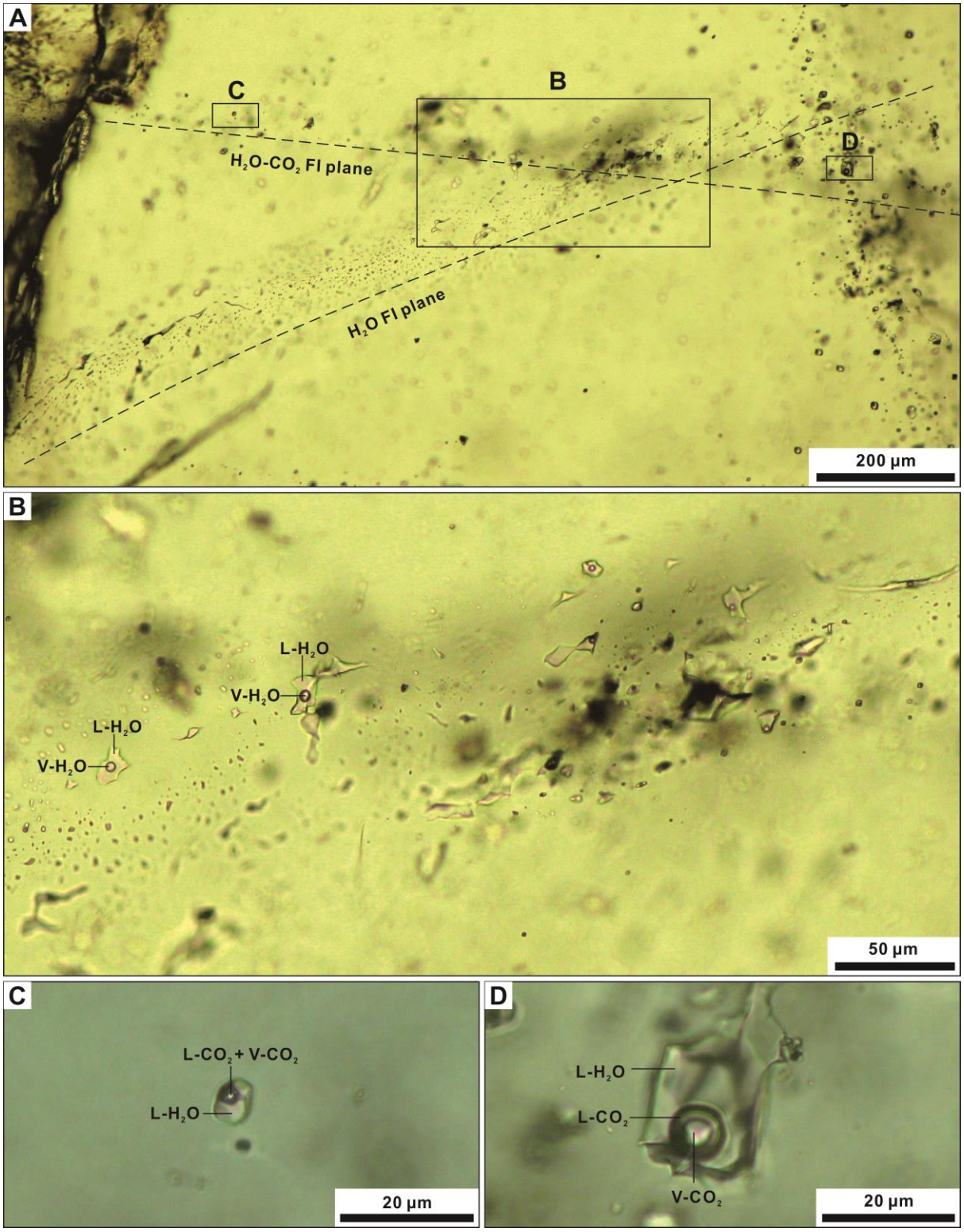


FIG. 3.10. Photomicrographs (plane-polarized transmitted light) showing cross-cutting relation between $H_2O$-$CO_2$ fluid inclusions and $H_2O$ fluid inclusions in stage I quartz. **A**. $H_2O$ fluid inclusion plane cutting a $H_2O$-$CO_2$ fluid inclusion plane at the intersection. Areas indicated by letters are detailed in B–D. Sample DH-540-3/540 m. **B**. Plane of secondary $H_2O$ fluid inclusions. Note $H_2O$ fluid inclusions all have a thin and irregular shape. **C**. Three phase $H_2O$-$CO_2$ fluid inclusion in a $H_2O$-$CO_2$ fluid inclusion plane. **D**. Three phase $H_2O$-$CO_2$ fluid inclusion in a $H_2O$-$CO_2$ fluid inclusion plane.

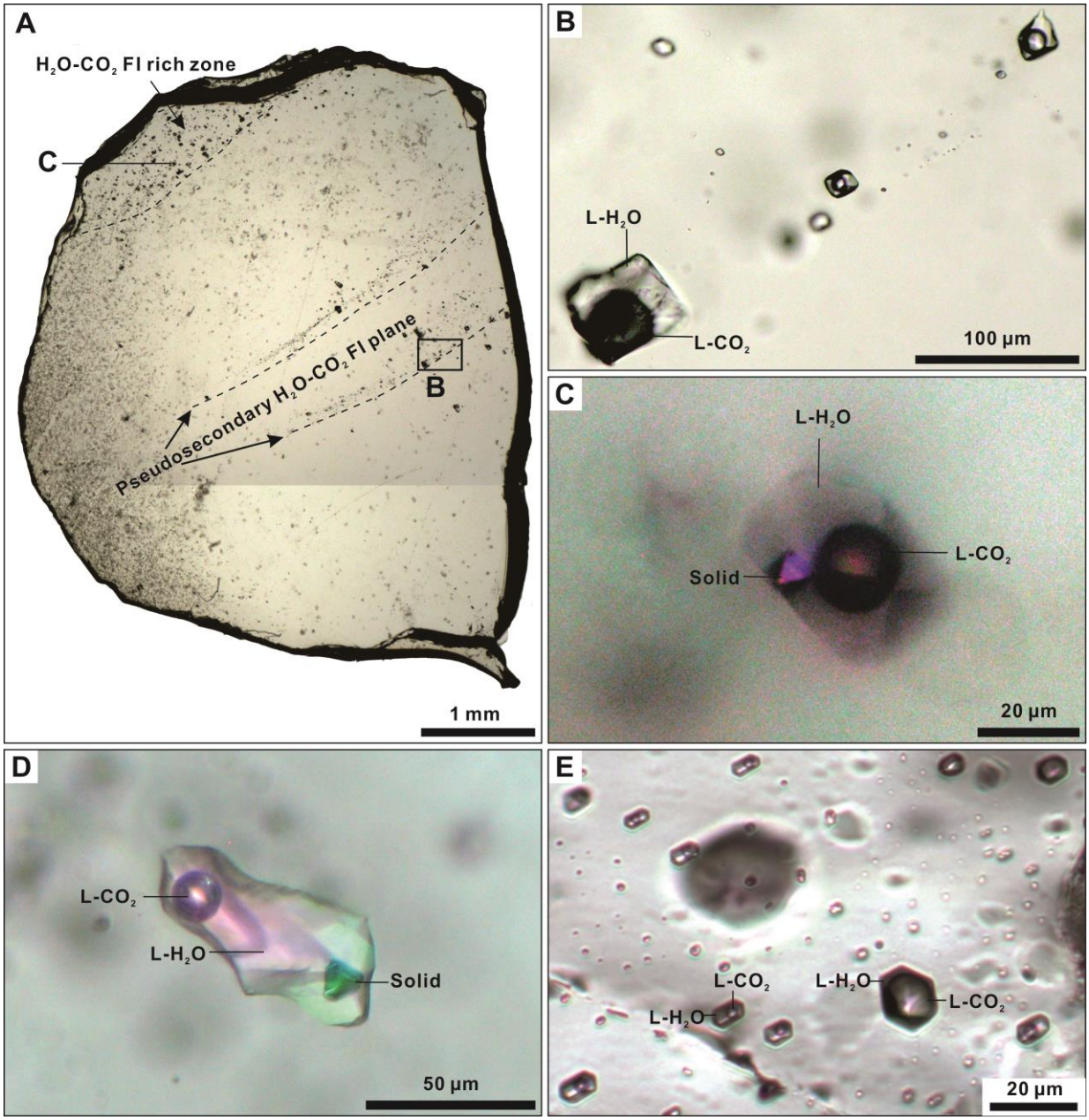


FIG. 3.11. Fluid inclusions in stage III quartz. Photomicrograph C and D were taken in double-polarized reflected light with quartz in extinction position; others were taken in plane-polarized transmitted light. **A**. Distribution of fluid inclusions in a fragment of stage III quartz crystal. Areas indicated by letters are detailed in B and C. Sample 470-F7-13/470 m. **B**. $H_2O$-$CO_2$ fluid inclusions in a pseudosecondary $H_2O$-$CO_2$ fluid inclusion plane. **C**. $H_2O$-$CO_2$ fluid inclusions in a $H_2O$-$CO_2$ fluid inclusion plane. One fluid inclusion contains a pinkish opaque solid. **D**. $H_2O$-$CO_2$ fluid inclusion containing a greenish opaque solid with triangular cross section. Sample 470-F7-13/470 m. E. $H_2O$-$CO_2$ fluid inclusion plane containing both low $CO_2$ fluid inclusions and high $CO_2$ fluid inclusions. Sample 470-F7-13/470 m. Abbreviations: FI = fluid inclusion.

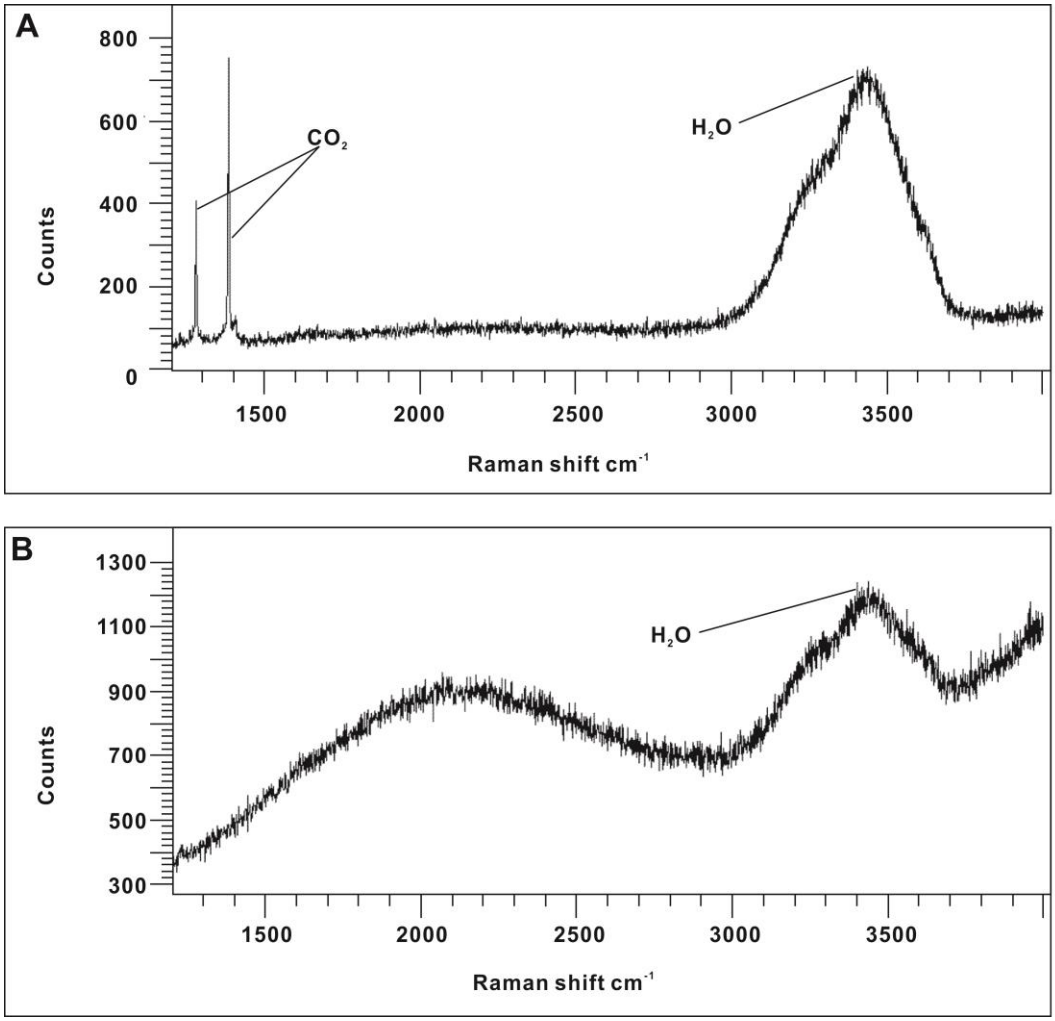


FIG. 3.12. Laser Raman spectra for a $H_2O$-$CO_2$ fluid inclusion (A) and a $H_2O$ fluid inclusion (B).

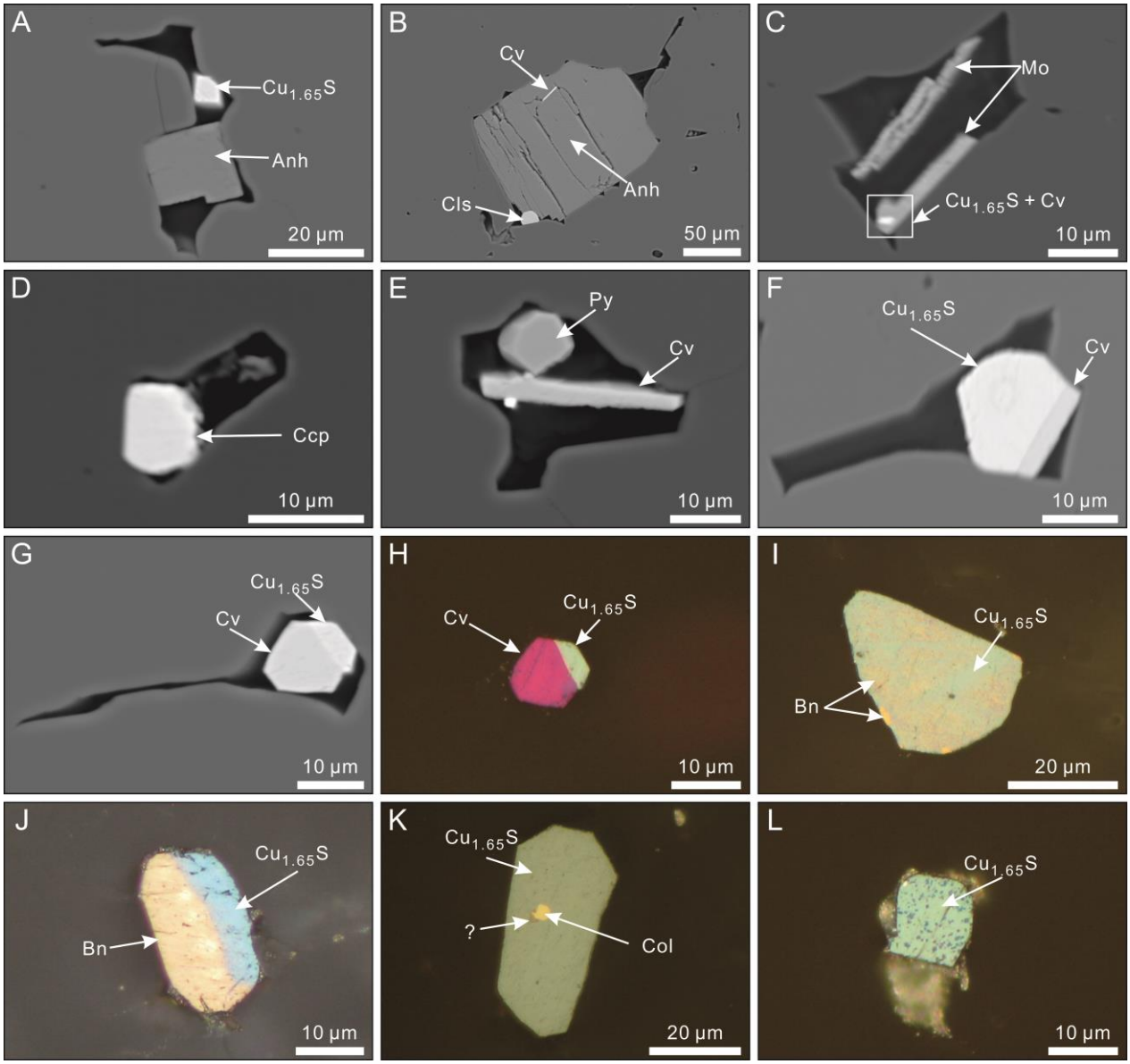


FIG. 3.13. BSE images (A–G) and photomicrographs (H–J) of solids in opened fluid inclusions. **A**. Anhydrite and $Cu_{1.65}S$. Sample LS-540-3/540 m. **B**. Anhydrite, celestine, and a covellite flake enclosed by anhydrite. Sample LS-540-3/540 m. **C**. Intergrowth of $Cu_{1.65}S$, covellite, and molybdenite. Sample LS-540-3/540 m. **D**. Chalcopyrite. Sample DH-540-3/540 m. **E**. Pyrite in contact with a covellite flake. Sample LS-540-3/540 m. **F**. Intergrowth of $Cu_{1.65}S$ and covellite. Sample LS-540-3/540 m. **G, H**. Intergrowth of $Cu_{1.65}S$ and covellite. Sample LS-540-3/540 m. **I**. $Cu_{1.65}S$ with bornite exsolutions. Sample LS-540-3/540 m. **J**. Intergrowth of $Cu_{1.65}S$ and bornite. Sample DH-540-3/540 m. **K**. $Cu_{1.65}S$ containing an colusite core and an unidentified phase. Sample LS-540-3/540 m. **L**. $Cu_{1.65}S$ altered by a deep blue phase. Sample LS-540-3/540 m. Abbreviations: Anh = anhydrite, Bn = bornite, Ccp = chalcopyrite, Cls = celestine, Col = colusite, Cv = covellite, Mo = molybdenite.

*3.2.3 Microthermometric data*

The microthermometric data of fluid inclusions are shown in Figure 3.14, 3.15, and Table 3.8, and are briefly described below.

*Stage I quartz:* For $H_2O$-$CO_2$ fluid inclusions, final melting temperatures of solid $CO_2$ range from -62.1 to -57.3 ℃, with 85% at between -58.5 and -57.3 ℃. $CO_2$-clathrate final melting is between 0.5 and 8.5 ℃, corresponding to salinities of 3.0 to 15.0 weight percent NaCl equivalent (Collins, 1979), with a mean of 7.9 wt.% NaCl equivalent. Total homogenization temperatures of $CO_2$ phases (i.e., $CO_2$ vapor and liquid) vary significantly, from 0.9 to 31.0 ℃. $H_2O$-$CO_2$ fluid inclusions finally homogenized at between 230 and 440 ℃, with a mean of 314 ℃. Most homogenized into the aqueous liquid phase, and a few homogenized by $CO_2$ bubble expansion or showing critical phenomena. $H_2O$ fluid inclusions all homogenized to the aqueous liquid phase at between 143 and 159 ℃. Final melting temperatures of ice range from -1.7 to -0.8 ℃, corresponding to salinities of 1.4 to 2.9 wt.% NaCl equivalent (Bodnar, 1993).

*Stage III quartz:* For $H_2O$-$CO_2$ fluid inclusions, final melting temperatures of solid $CO_2$ vary from -61.1 to -57.4 ℃. $CO_2$-clathrate finally melted at between 1.0 and 6.1 ℃, corresponding to salinities of 7.2 to 14.4 wt.% NaCl equivalent (Collins 1979), with a mean of 10.7 wt.% NaCl equivalent. Total homogenization temperatures of $CO_2$ phases (i.e., $CO_2$ vapor and liquid) vary significantly, from 2.8 to 30.6 ℃. $H_2O$-$CO_2$ fluid inclusions finally homogenized at between 198 and 320 ℃, with a mean of 262 ℃. Most homogenized into the aqueous liquid phase, and a few homogenized by $CO_2$ bubble expansion or showing critical phenomena. $H_2O$ fluid inclusions all homogenized to the aqueous liquid phase at between 149 and 204 ℃. Final melting temperatures of ice range from -17.0 to -0.6 ℃, corresponding to salinities of 1.1 to 20.2 wt.% NaCl equivalent (Bodnar, 1993).

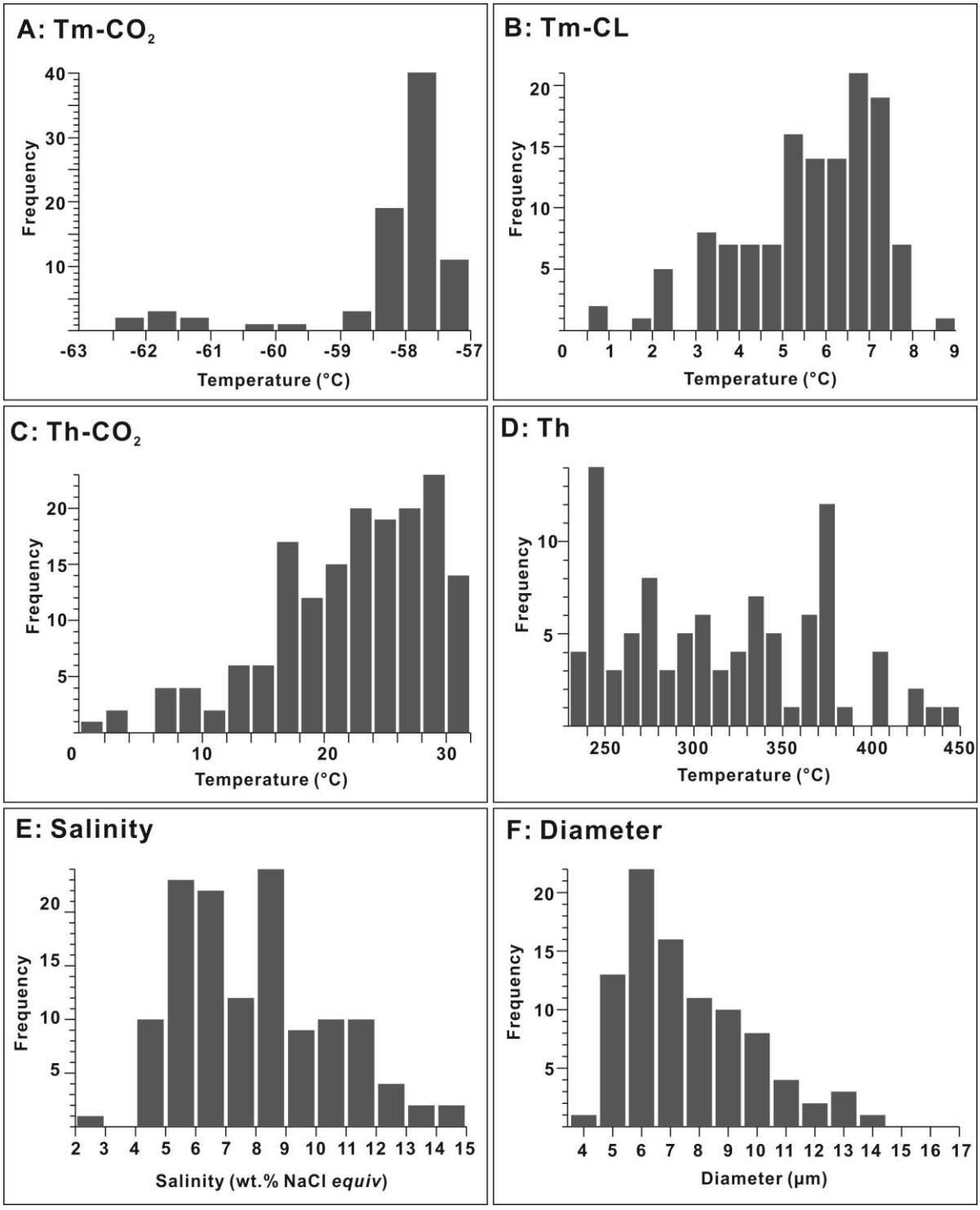


FIG. 3.14. Frequency histograms of microthermometric data for $H_2O$-$CO_2$ fluid inclusions in stage I quartz. **A**. Final melting temperatures of solid $CO_2$. **B**. Final melting temperatures of $CO_2$–$H_2O$ clathrate. **C**. Homogenization temperatures of the $CO_2$ phases. **D**. Total homogenization temperatures of $H_2O$-$CO_2$ fluid inclusions. **E**. Salinities of $H_2O$-$CO_2$ fluid inclusions. **F**. Diameters of $H_2O$-$CO_2$ fluid inclusions with measured total homogenization temperatures.

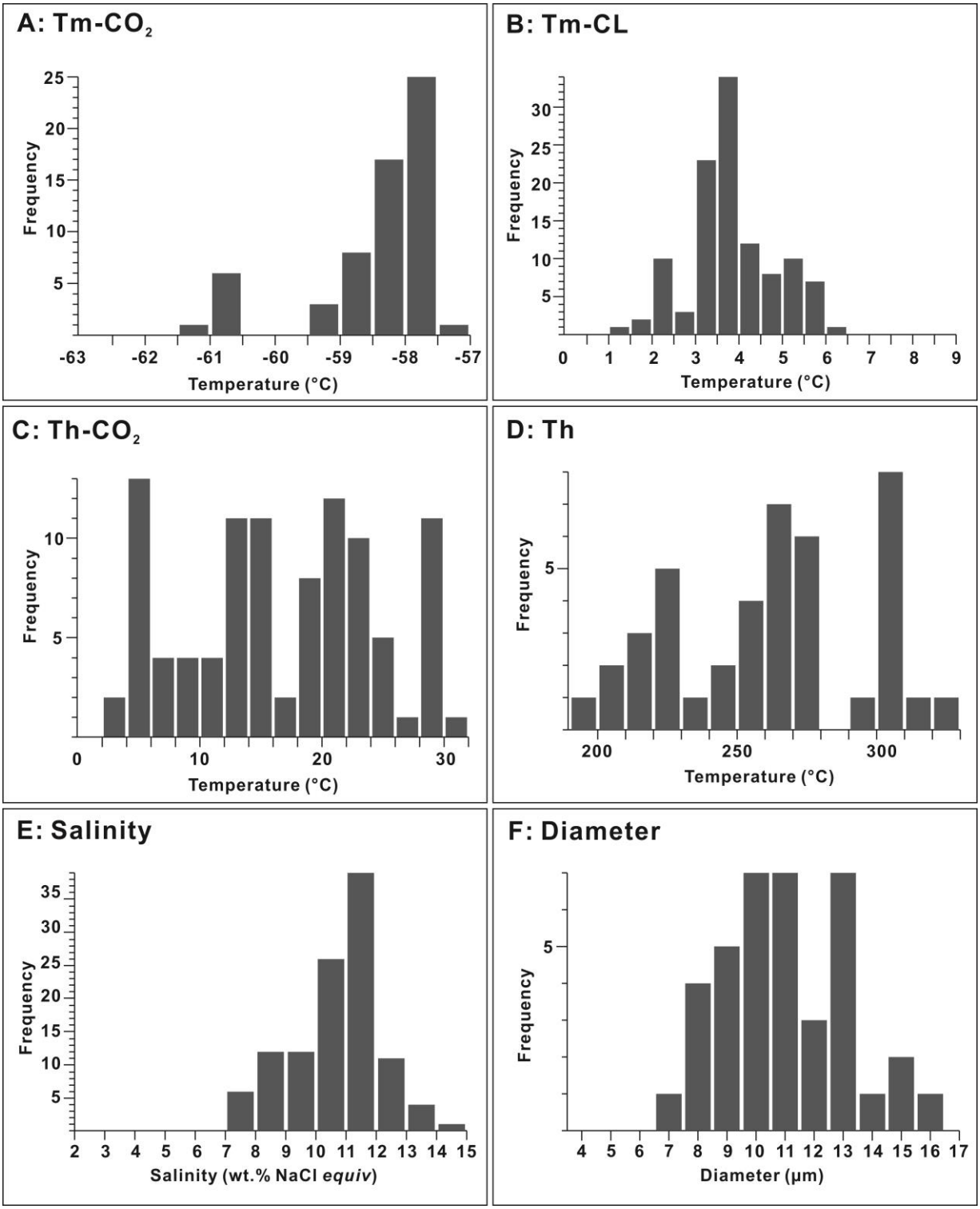


FIG. 3.15. Frequency histograms of microthermometric data for $H_2O$-$CO_2$ fluid inclusions in stage III quartz. **A**. Final melting temperatures of solid $CO_2$. **B**. Final melting temperatures of $CO_2$–$H_2O$ clathrate. **C**. Homogenization temperatures of the $CO_2$ phases. **D**. Total homogenization temperatures of $H_2O$-$CO_2$ fluid inclusions. **E**. Salinities of $H_2O$-$CO_2$ fluid inclusions. **F**. Diameters of $H_2O$-$CO_2$ fluid inclusions with measured total homogenization temperatures.

TABLE 3.8. Microthermometric data of fluid inclusions

| | | $TmCO_2$ (℃) | | Tmclath (℃) | | $ThCO_2$ (℃) | |
|---|---|---|---|---|---|---|---|
| Quartz stage | FI type | Range (N) | Average (SD) | Range (N) | Average (SD) | Range (N) | Average (SD) |
| I | $H_2O$-$CO_2$ | -62.1 to -57.3 (79) | -58.1 (1.1) | 0.5 to 8.5 (129) | 5.6 (1.6) | 0.9 to 31.0 (165) | 22.1 (6.5) |
| | $H_2O$ | | | | | | |
| III | $H_2O$-$CO_2$ | -61.1 to -57.4 (61) | -58.4 (1.0) | 1.0 to 6.1 (111) | 3.8 (1.0) | 2.8 to 30.6 (99) | 16.7 (7.9) |
| | $H_2O$ | | | | | | |
| | | Tmice(℃) | | Salinity (wt.% NaClequiv.) | | Th (℃) | |
| Quartz stage | FI type | Range (N) | Average (SD) | Range (N) | Average (SD) | Range (N) | Average (SD) |
| I | $H_2O$-$CO_2$ | | | 3.0 to 15.0 (129) | 7.9 (2.5) | 230 to 440 (95) | 314 (56) |
| | $H_2O$ | -0.8 to -1.7 (5) | -1.1 (0.3) | 1.4 to 2.9 (5) | 1.9 (0.5) | 143 to 159 (5) | 154 (6) |
| III | $H_2O$-$CO_2$ | | | 7.2 to 14.4 (111) | 10.7 (1.5) | 198 to 320 (42) | 263 (34) |
| | $H_2O$ | -0.6 to -17 (11) | -8.8 (6.1) | 1.1 to 20.2(11) | 11.5 (6.8) | 149 to 204 (11) | 162 (15) |

Salinities for $H_2O$-$CO_2$ fluid inclusions are calculated from final melting temperatures of $CO_2$-clathrate after Collins (1979). Salinities for $H_2O$-$CO_2$ fluid inclusions are calculated from final melting temperatures of ice after Bodnar (1993). Abbreviations: FI = fluid inclusion, N = number of significant values, SD = standard deviation, $T_mCO_2$= final melting temperature of solid $CO_2$, $T_m$clath = final melting temperature of $CO_2$–$H_2O$ clathrate, $T_h$ $CO_2$ = homogenization temperature of the $CO_2$ phases, $T_m$ice = final melting temperature of ice, $T_h$ = total homogenization temperature of fluid inclusion. wt.% $NaCl_{equiv.}$ = weight % NaCl equivalent

### *3.2.4 Uv-Fs-LA-ICP-MS data*

A total number of 76 individual Type 1 $H_2O$-$CO_2$ fluid inclusions were analyzed by LA-ICP-MS, belonging to 24 fluid inclusion assemblages (FIA) with 1–7 inclusions per assemblage. B, Na, K, Rb, Sr, and Cs are always present in detectable concentrations for $H_2O$-$CO_2$ fluid inclusions in both stage I and stage III quartz, while Pb and Zn are always present in detectable concentrations in $H_2O$-$CO_2$ fluid inclusions in stage III quartz. Although Mn, Cu, Fe, Ag, Mo, Te, Au, and Bi were detected in some fluid inclusions, most of which do not show distinct peaks for Mn, Cu, Fe, and Ag in the time-resolved ICP-MS signals during the ablation of fluid inclusions, and all do not show peaks for Mo, Te, Au, and Bi (e.g., Figs. 3.16, 3.17). Further, where detected, the concentrations of Mn, Cu, Fe, and Ag, especially Mo, Te, Au, and Bi, are often close to the detection limit. This implies that some detected element concentrations are analytical artefacts. Therefore, the uncertainties of element concentrations in individual fluid inclusions are firstly used to assess the quality of data. For individual fluid inclusion data, element concentrations with errors >50% and without visible peak in the

time-resolved ICP-MS signals are considered as artefacts and were not included when calculated the average element concentrations of fluid inclusion assemblages. LA-ICP-MS data here are reported as average element concentrations of fluid inclusion assemblages and are summarised in Table 3.9. The complete data set for each individual inclusion is reported in the Appendix.

*FIA in Stage I quartz:* Na is the dominant cation (13867–27928 ppm), followed by K (3286–10086 ppm) and B (145–502 ppm). The concentrations of other alkali (Li: 20–235 ppm, Rb: 21–83 ppm, Cs: 9–46 ppm) and earth alkaline (Sr: 4–91 ppm, Ba: 1–44 ppm) elements are typically in the range of several to tens of ppm. The concentrations of Mn (9–158 ppm), Zn (15–173 ppm), Pb (0.4–31 ppm) are quite low, mostly below their crustal averages (Mn: 950 ppm, Zn: 70 ppm, Pb: 13 ppm; Taylor 1964). The concentrations of Cu are also rather low (5–56 ppm), except one FIA (FIA A8) consisting of three solid-bearing fluid inclusions shows much higher value (19 wt.%). Fe, Mo, Te, and Bi are always below the detection limit, while Ag was only detected in the solid-bearing FIA (Ag: 629 ppm; FIA A8). Au was only detected in one fluid inclusion within one FIA (Au: 1 pm), but peak for Au was not observed in the time-resolved ICP-MS signal.

*FIA in Stage III quartz:* Like FIA in stage I quartz, FIA in stage III quartz are dominated by Na (24203–37211 ppm) and K (9869–16592) with subordinate amounts of B (130–527 ppm). Compared with FIA in Stage I quartz, the systematically higher concentrations of Na and K are correlated with the higher salinities. The concentrations of other alkali (Li: 31–57 ppm, Rb: 28–64 ppm, Cs: 5–13 ppm) and earth alkaline (Sr: 20–76 ppm, Ba: 2–10 ppm) elements are all in the range of several to tens of ppm. On average, FIA in stage III quartz contain ten times more Pb (19–120 ppm) than FIA in stage I quartz. This is in accordance with the fact that galena is the dominant mineral during stage III mineralization. The concentrations of Mn, Cu, and Zn range from 19 to 44 ppm, 6 to 179 ppm, and 13 to 58 ppm, respectively. Mo, Ag, Te, Au, and Bi are always below the detection limit, while Fe was only detected in one fluid inclusion within one FIA (Fe: 104 ppm).

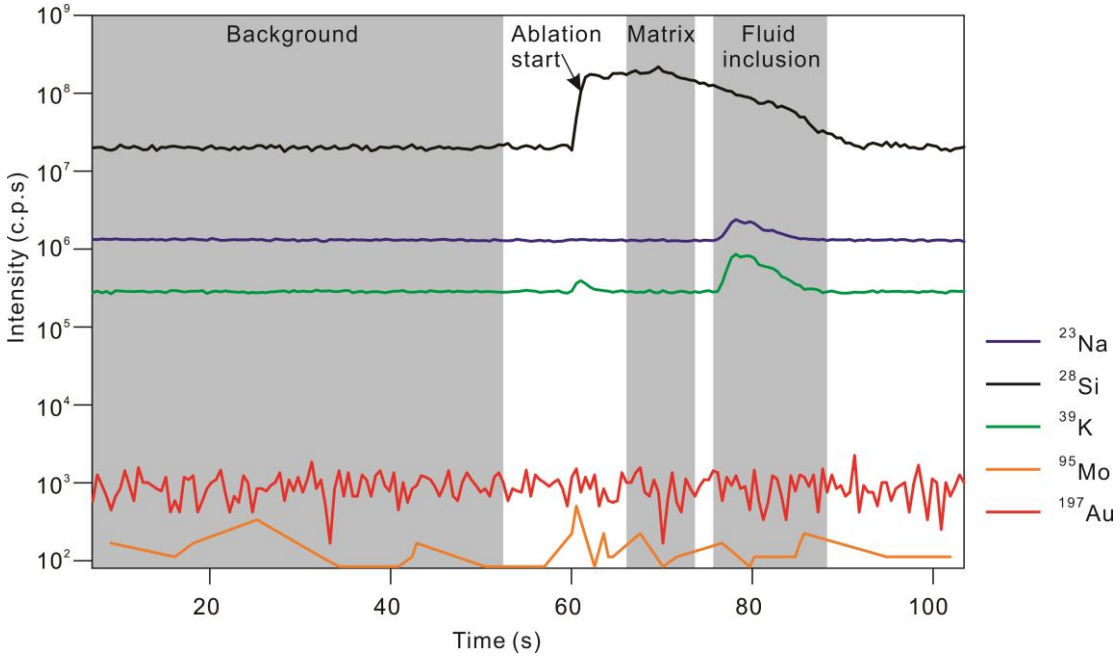


Fig. 3.16. Time-resolved LA-ICP-MS signal of a single fluid inclusion (DH-505-8-L2) in stage I quartz. Only Na, Si, K, Mo, and Au signal lines are shown here. Grey areas show the integration windows used for calculation of background, matrix (quartz), and fluid inclusion signal. Note calculated Mo and Au concentrations in this fluid inclusion are 2.4 ppm and 2.0 ppm, respectively, but the time-resolved LA-ICP-MS signal does not show peaks for Mo and Au during the ablation of the fluid inclusion.

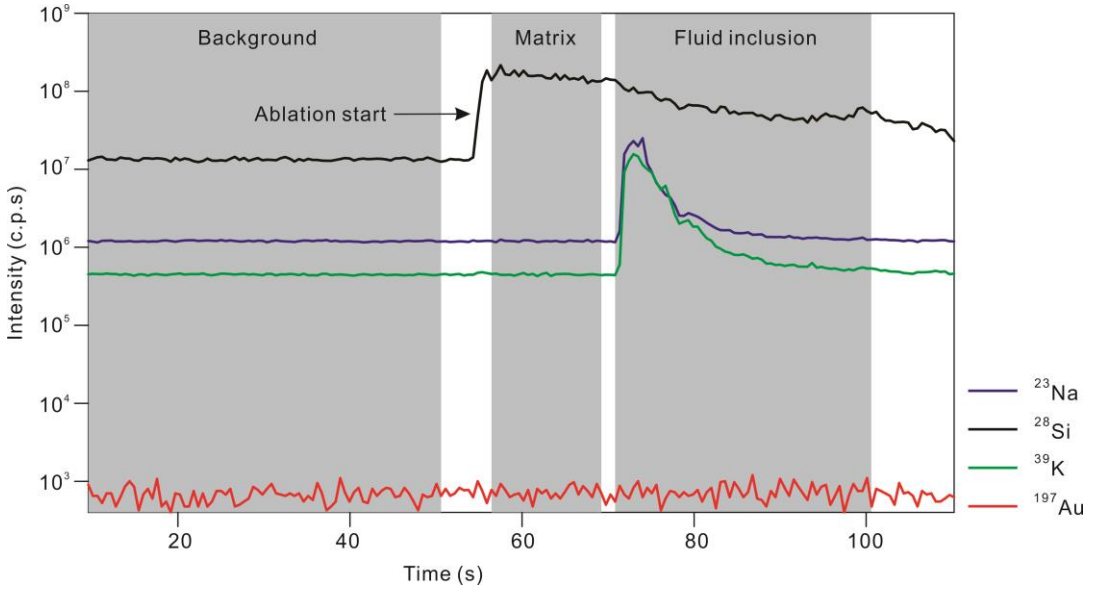


Fig. 3.17. Time-resolved LA-ICP-MS signal of a single fluid inclusion (470-F7-13D-L31) in stage I quartz. Only Na, Si, K, Mo, and Au signal lines are shown here. Grey areas show the integration windows used for calculation of background, matrix (quartz), and fluid inclusion signal. Note calculated Au concentration in this fluid inclusion is 0.5 ppm, but the time-resolved LA-ICP-MS signal does not show peaks for Au during the ablation of the fluid inclusion.

TABLE 3.9. Element concentrations (ppm) in fluid inclusions assemblages (FIA)

| FIA | N | Salinity (wt.%) | Li | SD (n) | B | SD (n) | Na | SD (n) | K | SD (n) | Mn | SD (n) | Fe | SD (n) | Cu | SD (n) | Zn | SD (n) | Rb | SD (n) |
|---|---|---|---|---|---|---|---|---|---|---|---|---|---|---|---|---|---|---|---|---|
| DH-505-8 | | | | | | | | | | | | | | | | | | | | |
| A1 | 4 | 6.8 | 20 | 3 (2) | 264 | 71 (4) | 21694 | 4257 (4) | 8417 | 1716 (4) | 30 | - (1) | <88 | - (0) | 56 | - (1) | <7 | - (0) | 83 | 20 (4) |
| A2 | 2 | 7.9 | 88 | 19 (2) | 424 | 79 (2) | 26733 | 747 (2) | 7155 | 291 (2) | 81 | - (1) | <95 | - (0) | <3 | - (0) | 63 | 9 (2) | 53 | 4 (2) |
| A3 | 3 | 8.6 | 235 | - (1) | 502 | 28 (3) | 27928 | 2604 (3) | 10086 | 1407 (3) | 158 | - (1) | <114 | - (0) | <4 | - (0) | 173 | - (1) | 69 | 16 (3) |
| A4 | 2 | 5.1 | 31 | 10 (2) | 177 | 2 (2) | 17649 | 4808 (2) | 4406 | 197 (2) | 18 | - (1) | <53 | - (0) | <2 | - (0) | <4 | - (0) | 41 | 2 (2) |
| A5 | 4 | 5.5 | 26 | 5 (3) | 177 | 30 (4) | 17856 | 2445 (4) | 6413 | 691 (4) | 10 | 3 (3) | <48 | - (0) | 7 | - (1) | <4 | - (0) | 59 | 7 (4) |
| A6 | 4 | 4.9 | 25 | 11 (3) | 156 | 13 (4) | 15746 | 1586 (4) | 5887 | 567 (4) | <6 | - (0) | <70 | - (0) | 5 | - (1) | <5 | - (0) | 42 | 14 (4) |
| A7 | 6 | 6.5 | 30 | 15 (6) | 217 | 38 (6) | 21879 | 2657 (6) | 6491 | 1313 (6) | 14 | 8 (4) | <53 | - (0) | <2 | - (0) | 15 | - (1) | 54 | 8 (6) |
| A8 | 3 | 5.0 | 29 | - (1) | 167 | 7 (3) | 13867 | 1644 (3) | 9714 | 1171 (3) | 40 | - (1) | <81 | - (0) | 191379 | 122706 (3) | <6 | - (0) | 35 | 2 (3) |
| A9 | 4 | 5.6 | 28 | 11 (3) | 169 | 32 (4) | 19036 | 1919 (4) | 5042 | 422 (4) | 19 | 6 (2) | <51 | - (0) | <2 | - (0) | <4 | - (0) | 35 | 4 (4) |
| A10 | 3 | 4.7 | 21 | - (1) | 153 | 18 (3) | 14632 | 2370 (3) | 6783 | 1160 (3) | <7 | - (0) | <71 | - (0) | <3 | - (0) | <5 | - (0) | 30 | 2 (3) |
| A11 | 1 | 5.9 | 72 | - (1) | 251 | - (1) | 21121 | - (1) | 3286 | - (1) | <3 | - (0) | <33 | - (0) | <1 | - (0) | <2 | - (0) | 21 | - (1) |
| A12 | 1 | 6.5 | <10 | - (0) | 169 | - (1) | 22913 | - (1) | 4787 | - (1) | 24 | - (1) | <64 | - (0) | <2 | - (0) | <4 | - (0) | 34 | - (1) |
| A13 | 1 | 5.7 | <20 | - (0) | 357 | - (1) | 19377 | - (1) | 5047 | - (1) | <12 | - (0) | <139 | - (0) | <5 | - (0) | <10 | - (0) | 36 | - (1) |
| A14 | 1 | 5.5 | 23 | - (1) | 164 | - (1) | 18603 | - (1) | 5227 | - (1) | 9 | - (1) | <45 | - (0) | <2 | - (0) | <3 | - (0) | 46 | - (1) |
| A15 | 1 | 5.1 | 74 | - (1) | 145 | - (1) | 17100 | - (1) | 5307 | - (1) | <8 | - (0) | <95 | - (0) | <3 | - (0) | <7 | - (0) | 41 | - (1) |
| Average | | 6.0 | 54 | | 233 | | 19742 | | 6270 | | 40 | | | | 47862 | | 84 | | 45 | |
| 470-F7-13A | | | | | | | | | | | | | | | | | | | | |
| B1 | 4 | 9.5 | 31 | 10 (4) | 130 | 77 (4) | 31373 | 3173 (4) | 9869 | 4386 (4) | 44 | - (1) | <63 | - (0) | 179 | - (1) | 13 | 3 (4) | 28 | 6 (4) |
| B2 | 7 | 9.4 | 44 | 8 (7) | 527 | 238 (7) | 29782 | 2370 (7) | 12155 | 1476 (7) | 19 | - (1) | <98 | - (0) | <3 | - (0) | 52 | 34 (7) | 50 | 7 (7) |
| B3 | 1 | 7.7 | 38 | - (1) | 149 | - (1) | 24203 | - (1) | 10355 | - (1) | 24 | - (1) | <60 | - (0) | <2 | - (0) | 21 | - (1) | 36 | - (1) |
| Average | | 8.8 | 38 | | 269 | | 28453 | | 10793 | | 29 | | | | 179 | | 29 | | 38 | |
| 470-F7-13D | | | | | | | | | | | | | | | | | | | | |
| C1 | 6 | 11 | 47 | 4 (6) | 370 | 45 (6) | 34485 | 1309 (6) | 14635 | 1543 (6) | 25 | 12 (2) | <54 | - (0) | <2 | - (0) | 58 | 28 (6) | 52 | 3 (6) |
| C2 | 7 | 10 | 44 | 7 (7) | 337 | 36 (7) | 32528 | 3648 (7) | 12387 | 1705 (7) | 28 | 1 (3) | 104 | (1) | 6 | - (1) | 39 | 12 (7) | 58 | 11 (7) |
| C3 | 5 | 11 | 49 | 5 (5) | 341 | 31 (5) | 34651 | 1037 (5) | 14985 | 1179 (5) | 34 | - (1) | <63 | - (0) | <2 | - (0) | 50 | 10 (5) | 47 | 5 (5) |
| C4 | 3 | 12 | 49 | 4 (3) | 288 | 48 (3) | 37211 | 358 (3) | 14391 | 1618 (3) | <8 | - (0) | <70 | - (0) | <2 | - (0) | 35 | 4 (3) | 51 | 7 (3) |
| C5 | 2 | 11 | 49 | 10 (2) | 321 | 9 (2) | 34761 | 1250 (2) | 12905 | 570 (2) | 23 | - (1) | <64 | - (0) | <2 | - (0) | 52 | 7 (2) | 64 | 5 (2) |
| C6 | 1 | 11 | 57 | - (1) | 339 | - (1) | 34265 | - (1) | 16592 | - (1) | <4 | - (0) | <32 | - (0) | <0.8 | - (0) | 38 | - (1) | 50 | - (1) |
| Average | | 11 | 49 | | 333 | | 34650 | | 14316 | | 27 | | 104 | | 6 | | 46 | | 54 | |

(Cont.)

| FIA | N | Salinity (wt.%) | Sr | SD (n) | Mo | SD (n) | Ag | SD (n) | Te | SD (n) | Cs | SD (n) | Ba | SD (n) | Au | SD (n) | Pb | SD (n) | Bi | SD (n) |
|---|---|---|---|---|---|---|---|---|---|---|---|---|---|---|---|---|---|---|---|---|
| DH-505-8 | | | | | | | | | | | | | | | | | | | | |
| A1 | 4 | 6.8 | 16 | 5 (4) | <0.8 | - (0) | <0.6 | - (0) | <5 | - (0) | 26 | 8 (4) | <1 | - (0) | <1.0 | - (0) | 5 | 5 (3) | <0.2 | - (0) |
| A2 | 2 | 7.9 | 37 | 17 (2) | <0.9 | - (0) | <0.8 | - (0) | <5 | - (0) | 43 | 2 (2) | 9 | 6 (2) | <1.1 | - (0) | 14 | 15 (2) | <0.1 | - (0) |
| A3 | 3 | 8.6 | 91 | 6 (3) | <1 | - (0) | <1 | - (0) | <6 | - (0) | 46 | 13 (3) | 44 | - (1) | <1.3 | - (0) | 31 | 16 (2) | <0.2 | - (0) |
| A4 | 2 | 5.1 | 7 | 1 (2) | <0.4 | - (0) | <0.5 | - (0) | <3 | - (0) | 12 | 0.1 (2) | <0.7 | - (0) | <0.6 | - (0) | 0.7 | - (1) | <0.1 | - (0) |
| A5 | 4 | 5.5 | 17 | 15 (4) | <0.4 | - (0) | <0.3 | - (0) | <3 | - (0) | 15 | 4 (4) | 1 | - (1) | <0.6 | - (0) | 2 | 1 (3) | <0.1 | - (0) |
| A6 | 4 | 4.9 | 8 | 4 (4) | <0.7 | - (0) | <0.6 | - (0) | <4 | - (0) | 11 | 3 (4) | <0.9 | - (0) | <0.8 | - (0) | 1 | 1 (2) | <0.1 | - (0) |
| A7 | 6 | 6.5 | 10 | 4 (6) | <0.5 | - (0) | <0.5 | - (0) | <3 | - (0) | 15 | 2 (6) | 1 | 0.7 (3) | <0.6 | - (0) | 2 | 0.8 (5) | <0.1 | - (0) |
| A8 | 3 | 5.0 | 15 | 10 (3) | <0.7 | - (0) | 629 | 467 (3) | <4 | - (0) | 10 | 0.9 (3) | 3 | - (1) | <0.9 | - (0) | 16 | 11 (3) | <0.1 | - (0) |
| A9 | 4 | 5.6 | 12 | 2 (4) | <0.5 | - (0) | <0.5 | - (0) | <3 | - (0) | 13 | 4 (4) | <0.7 | - (0) | 1 | - (1) | 3 | 4 (2) | <0.1 | - (0) |
| A10 | 3 | 4.7 | 10 | 0.7 (3) | <0.6 | - (0) | <0.6 | - (0) | <4 | - (0) | 11 | 0.7 (3) | 3 | - (1) | <0.9 | - (0) | 0.4 | 0 (2) | <0.1 | - (0) |
| A11 | 1 | 5.9 | 4 | - (1) | <0.3 | - (0) | <0.3 | - (0) | <2 | - (0) | 9 | - (1) | <0.5 | - (0) | <0.4 | - (0) | <0.1 | - (1) | <0.1 | - (0) |
| A12 | 1 | 6.5 | 9 | - (1) | <0.5 | - (0) | <0.6 | - (0) | <3 | - (0) | 13 | - (1) | 3 | - (1) | <0.8 | - (0) | 1 | - (0) | <0.1 | - (0) |
| A13 | 1 | 5.7 | 21 | - (1) | <1 | - (0) | <1 | - (0) | <7 | - (0) | 27 | - (1) | <2 | - (0) | <1.6 | - (0) | <0.3 | - (1) | <0.2 | - (0) |
| A14 | 1 | 5.5 | 11 | - (1) | <0.4 | - (0) | <0.4 | - (0) | <3 | - (0) | 14 | - (1) | 0.9 | - (1) | <0.5 | - (0) | 1 | - (0) | <0.1 | - (0) |
| A15 | 1 | 5.1 | 13 | - (1) | <0.9 | - (0) | <0.8 | - (0) | <5 | - (0) | 11 | - (1) | <1 | - (0) | <1.1 | - (0) | <0.2 | - (1) | <0.1 | - (0) |
| Average | | 6.0 | 19 | | | | 629 | | | | 18 | | 8.1 | | 1.5 | | 6.4 | | | |
| 470-F7-13A | | | | | | | | | | | | | | | | | | | | |
| B1 | 4 | 9.5 | 33 | 16 (4) | <0.4 | - (0) | <0.5 | - (0) | <3 | - (0) | 5 | 1 (4) | 2 | 1 (4) | <0.4 | - (0) | 22 | 10 (4) | <0.1 | - (0) |
| B2 | 7 | 9.4 | 38 | 25 (7) | <0.6 | - (0) | <0.8 | - (0) | <4 | - (0) | 13 | 4 (7) | 5 | 3 (6) | <0.5 | - (0) | 39 | 16 (7) | <0.1 | - (0) |
| B3 | 1 | 7.7 | 20 | - (1) | <0.3 | - (0) | <0.4 | - (0) | <3 | - (0) | 8 | - (1) | 3 | (1) | <0.3 | - (0) | 19 | - (1) | <0.1 | - (0) |
| Average | | 8.8 | 30 | | | | | | | | 8.5 | | 3.3 | | | | 27 | | | |
| 470-F7-13D | | | | | | | | | | | | | | | | | | | | |
| C1 | 6 | 11 | 73 | 18 (6) | <0.3 | - (0) | <0.4 | - (0) | <2 | - (0) | 6 | 0.7 (6) | 8 | 6 (6) | <0.3 | - (0) | 90 | 28 (6) | <0.1 | - (0) |
| C2 | 7 | 10 | 76 | 14 (7) | <0.3 | - (0) | <0.3 | - (0) | <2 | - (0) | 8 | 3 (7) | 10 | 7 (7) | <0.3 | - (0) | 120 | 83 (7) | <0.1 | - (0) |
| C3 | 5 | 11 | 61 | 5 (5) | <0.3 | - (0) | <0.5 | - (0) | <3 | - (0) | 6 | 0.5 (5) | 6 | 1 (5) | <0.4 | - (0) | 104 | 8 (5) | <0.1 | - (0) |
| C4 | 3 | 12 | 47 | 8 (3) | <0.3 | - (0) | <0.5 | - (0) | <3 | - (0) | 6 | 2 (3) | 2 | (1) | <0.4 | - (0) | 103 | 55 (3) | <0.1 | - (0) |
| C5 | 2 | 11 | 72 | 0.1 (2) | <0.4 | - (0) | <0.5 | - (0) | <3 | - (0) | 7 | 2 (2) | 6 | 4 (2) | <0.4 | - (0) | 100 | 37 (2) | <0.1 | - (0) |
| C6 | 1 | 11 | 60 | - (1) | <0.1 | - (0) | <0.2 | - (0) | <1 | - (0) | 5 | - (1) | 7 | (1) | <0.2 | - (0) | 88 | - (1) | <0.1 | - (0) |
| Average | | 11 | 65 | | | | | | | | 6 | | 6 | | | | 101 | | | |

Abbreviations: N = Number of analyzed inclusions, n = Number of significant concentrations, SD = standard deviation.

### 3.3 Stable isotope data

Oxygen and hydrogen isotope analyses of 22 stage I quartz samples were performed with a MAT253EM mass spectrometer at the Isotopic Laboratory of the Institute of Mineral Resources, Chinese Academy of Geological Sciences. Oxygen isotope analyses for quartz were performed using the $BrF_5$ technique of Clayton and Mayeda (1963). For hydrogen isotope analyses of fluid inclusion waters, quartz samples were outgassed at 105℃ for 12 hours, and then fluid inclusions were decrepitated by heating at 500 to 600℃. Released waters were converted to hydrogen gas by using the zinc reduction method of Coleman et al. (1982). All $\delta^{18}O$ and $\delta D$ values reported are in per mil relative to the SMOW standard. The analytical uncertainty is ±0.2‰ for oxygen and ±2‰ for hydrogen.

The hydrogen and oxygen isotope compositions of 22 stage I quartz samples are given in Table 3.10. The $\delta^{18}O$ values for quartz range from 10.2 to 12.0‰, whereas the $\delta D$ values for fluid inclusion waters range from -117 to -54‰.

TABLE 3.10. Oxygen and hydrogen isotope data of stage I quartz

| Sample No. | Elevation m/fault | $\delta^{18}O_{quartz}$ (‰) | $\delta D$ (‰) | $\delta^{18}O_{fluid}$ (‰) |
|---|---|---|---|---|
| 470-F7-12-1 | 470/F7 | 11.0 | -113 | 6.4 |
| 470-F7-33 | 470/F7 | 11.5 | -110 | 6.9 |
| 470-F7-8 | 470/F7 | 11.2 | -98 | 6.6 |
| F7-19 | 540/F7 | 11.3 | -95 | 6.7 |
| F7-11 | 505/F7 | 10.6 | -90 | 6.0 |
| F5-505-1 | 505/F5 | 11.2 | -94 | 6.6 |
| YM540-B3 | 540/F5 | 11.0 | -90 | 6.4 |
| YM540-B6 | 540/F5 | 10.6 | -92 | 6.0 |
| YM505-B10 | 505/F35 | 10.5 | -117 | 5.9 |
| YM505-B12 | 505/F35 | 10.6 | -102 | 6.0 |
| S35-4 | 505/F35 | 12.0 | -94 | 7.4 |
| 470-19 | 470/F7 | 11.2 | -55 | 6.6 |
| 470-f7-18 | 470/F7 | 10.6 | -83 | 6.0 |
| 690-5 | 690/F8 | 10.2 | -54 | 5.6 |
| 540-b1 | 540/F5 | 11.8 | -73 | 7.2 |
| D540-3-a | 540/F7 | 11.4 | -91 | 6.8 |
| 470-f7-20 | 470/F7 | 11.1 | -83 | 6.5 |
| 505-B38 | 505/F7 | 11.7 | -87 | 7.1 |
| 505-B1-2 | 505/F5 | 11.9 | -81 | 7.3 |
| DH-B9 | Ore pile | 11.2 | -89 | 6.6 |
| 435-B3 | 435/F7 | 11.8 | -93 | 7.2 |
| 540-18-b | 540/F5 | 11.9 | -62 | 7.3 |

$\delta^{18}O_{fluid}$ values are calculated by the quartz-water fractionation equation of Matsuhisa et al. (1979) for a temperature of 375℃

### 3.4 Re-Os isotope data

Four ore samples were collected from underground exposures for Re-Os isotope analyses. Sample locations are projected in Figure 3.1. Sample 470-F7-11 and 470-F7-20 were collected from an Au-Mo mineralized quartz vein controlled by the F7 fault, at an elevation of ~470 m. Both samples show a friable texture. They have similar mineralogy and consist of K-feldspar, quartz, molybdenite, pyrite, and galena, and small amounts of chalcopyrite, monazite, rutile, and tellurides. Very fine-grained (<0.1 mm) molybdenite (stage II) occurs as fracture-fillings in quartz and K-feldspar, but minor molybdenite (stage I) also occurs as dissemination in quartz and K-feldspar. Molybdenite aggregates often enclose monazite and chalcopyrite, and are locally enclosed by galena. Native gold was not discovered in the two samples but in ore samples close to them. Sample YM540-B1 and YM540-B6 were collected from Mo mineralized quartz veins controlled by the F5 fault, at an elevation of ~540 m. Both samples consist of compact milky white quartz with molybdenite films (stage II) and disseminations (stage I). Small amounts of pyrite and K-feldspar were also discovered. Microscopic work was not carried out for the two samples.

#### *3.4.1 Sample preparation and analytical techniques*

Bulk molybdenum ore samples were first crushed, and then molybdenite was magnetically separated and handpicked using a binocular microscope. Fresh, non-oxidized molybdenite powders (<0.1 mm in size and purity >99%) were used for Re-Os isotope analyses.

Re-Os isotope analyses were carried out at the Re-Os Laboratory of the National Research Center of Geoanalysis, Chinese Academy of Geological Sciences. Sample preparation, chemical separation, and analytical procedure have been described in Shirey and Walker (1995), Markey et al. (1998), and Du et al. (2004), and are briefly summarized below. HCl-$HNO_3$ digestion was used for sample dissolution. The weighed sample was loaded in a Carius tube (thick-walled borosilicate glass ampoule) through a thin neck long funnel. Then enriched $^{190}Os$ and $^{185}Re$ spike solution (obtained from the Oak Ridge National Laboratory), 2–3 ml of 10 *M* HCl, and 4–5 ml of 16 *M* $HNO_3$ were added while the bottom part of the tube was frozen at -50 to -80 ℃ in an ethanol-liquid nitrogen slush. The top of the tube was sealed using an oxygen–propane torch. The tube was then placed in a stainless-steel jacket and heated for 24 h at 200 ℃. Upon cooling, the bottom part of the tube was kept frozen, the neck of the tube was broken, and the contents of the tube were poured into a distillation flask. The residue was

washed out with 20 ml of water. $OsO_4$ was distilled at 105–110 ℃ for 30 minutes and trapped in 5 ml of water. The water trap solution was used for ICP-MS determination of the Os isotope ratio. The residual Re-bearing solution was saved in a 150 ml Teflon beaker for Re separation. The Re-bearing solution was evaporated to dryness, and 1 ml of water was added twice with heating to near-dryness. Then, 4–10 ml of 5 *M* NaOH was added to the residue to obtain alkaline conditions, followed by Re extraction with 4–10 ml of acetone in a 120-ml Teflon separation funnel. After that, the acetone phase was transferred to a 150-ml Teflon beaker that contained 2 ml of water, and was subsequently evaporated to dryness. Then, several drops of concentrated $HNO_3$ and 30% $H_2O_2$ were added to dissolve Re. Finally, the solution was evaporated to dryness and picked up in 2% $HNO_3$ for ICP-MS determination of the Re isotope ratio (Du et al., 2004). A TJA X-series ICP-MS was used for Re and Os isotope determination. The analytical reliability was tested by analyses of the Certified Reference Material GBW04436 (JDC standard). Average blanks for the Carius tube procedure are 0.04635 ng Re, 0.0003 ng common Os, and 0.0001 ng $^{187}$Os.

*3.4.2 Results*

Re-Os abundances and isotopic data for four molybdenite samples are given in Table 3.11. Rhenium, common Os, $^{187}$Re, and $^{187}$Os concentrations vary from 0.594 to 1.812 ppm, 0.044 to 0.455 ppb, 0.3733 to 1.139 ppm, and 1.305 to 3.937 ppb, respectively. The model ages are calculated with the decay constant of $\lambda^{187}\text{Re} = 1.666 \times 10^{-11}$ yr$^{-1}$ with an absolute uncertainty of $0.017 \times 10^{-11}$ (1%) (Smoliar et al., 1996). Model age uncertainty includes the uncertainty of the decay constant (1%) and is given as 2σ. Four model ages range from 207.1 ± 3.1 to 210.4 ± 3.1 Ma with an isochron age of 206.4 ± 3.9 Ma (Fig. 3.18). The isochron age is calculated by the ISOPLOT 4.15 software of Ludwig (2012).

TABLE 3.11. Re-Os data of molybdenite

| | Sample weight g | Re μg/g | | Common Os ng/g | | $Re^{187}$ μg/g | | $Os^{187}$ ng/g | | Model age Ma | |
|---|---|---|---|---|---|---|---|---|---|---|---|
| Sample No. | | Measured | Error | Measured | Error | Measured | Error | Measured | Error | Measured | Error |
| 470-F7-11 | 0.05037 | 0.7704 | 0.0068 | 0.396 | 0.004 | 0.4842 | 0.0043 | 1.699 | 0.017 | 210.2 | 3.3 |
| 470-F7-20 | 0.02151 | 0.8306 | 0.0063 | 0.455 | 0.019 | 0.5221 | 0.004 | 1.833 | 0.017 | 210.4 | 3.1 |
| YM540-B1 | 0.04597 | 1.812 | 0.017 | 0.134 | 0.005 | 1.139 | 0.01 | 3.937 | 0.034 | 207.1 | 3.1 |
| YM540-B6 | 0.04117 | 0.594 | 0.0055 | 0.044 | 0.01 | 0.3733 | 0.0034 | 1.305 | 0.012 | 209.5 | 3.3 |

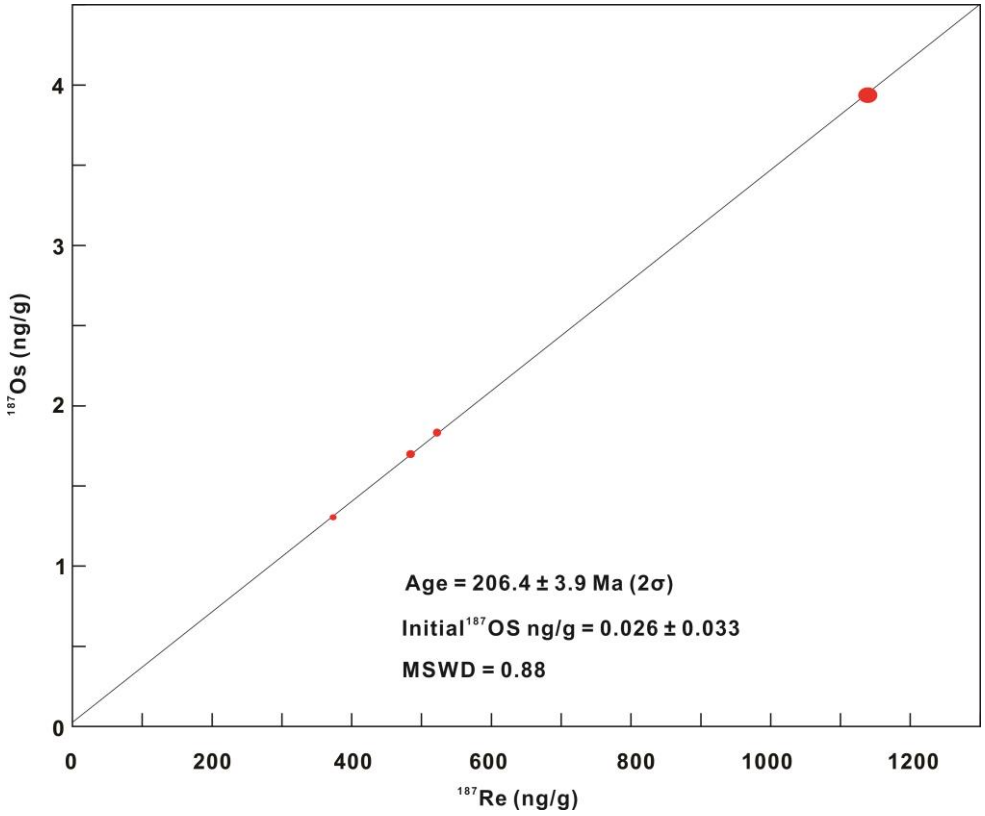


FIG. 3.18. Re-Os isochron diagram for four molybdenite samples. Isochron age is calculated by the ISOPLOT 4.15 software of Ludwig (2012).

## 3.5 Discussion

### *3.5.1 Timing of mineralization*

Our four Re-Os molybdenite model ages range from 210.4 ± 3.1 to 207.1 ± 3.1 Ma (Table 3.11) and yield an isochron age of 206.4 ± 3.9 Ma (MSWD = 0.88) (Fig. 3.18). These new ages are slightly younger than previously reported Re-Os molybdenite ages. Li et al. (2007) obtained three model ages of 232.9 ± 2.7 Ma, 223.7 ± 2.6 Ma, and 223.0 ± 2.8 Ma. Li et al. (2008) obtained six model ages of 255.6 ± 9.6 Ma, 252.8 ± 6.0 Ma, 236.9 ± 7.4 Ma, 232.1 ± 10.0 Ma, 220.6 ± 8.8 Ma, and 215.4 ± 5.4 Ma, with a poorly defined isochron age of 218 ± 41 Ma (MSWD = 38). For the Re-Os molybdenite ages of Li et al. (2008), information on common Os and spike is not provided. One possibility is that they used common Os as spike during the sample preparation; for molybdenite samples with $^{187}$Os/common Os ratios <~40, this can lead to inaccurate ages (Li et al., 2012c). Excluding the Re-Os molybdenite ages of Li et al. (2008), seven Re-Os molybdenite model ages range from 232.9 ± 2.7 to 207.1 ± 3.1 Ma. One tentative explanation for the large age span is that the Re-Os molybdenite ages reflect multiple episodes of molybdenum mineralization. This would be consistent with the petrographic observations that indicate at least two stages of molybdenite deposition. Stage I quartz with molybdenite disseminations (Fig. 3.5A) is fractured and brecciated, and subsequently filled by stage II molybdenite (Fig. 3.4C). Our Re-Os molybdenite samples are mainly stage II molybdenite with minor stage I molybdenite. For the Re-Os molybdenite samples of Li et al. (2007), however, information on mineral paragenesis is not provided.

Petrographic observations indicate that gold precipitated later than molybdenite. The exact time of gold mineralization, however, is not well constrained, because no mineral sharing a cogenetic relationship with gold has been dated. Monazite associated with molybdenite yields SHRIMP U–Th–Pb ages ranging from 224.3 ± 3.3 to 101.1 ± 7.1 Ma, with a peak at 216 ± 5 Ma (Li et al., 2011). The scattered ages, together with the fractured texture of the measured monazite, suggest that monazite may have undergone low-temperature alteration (e.g., Poitrasson et al., 2000; Seydoux-Guillaume et al., 2012; Didier et al., 2013). Li et al. (2011) proposed that 216 ± 5 Ma represents the time of monazite and molybdenite deposition, and the younger and scattered ages are related to monazite alteration, which partially disturbed the U–Th–Pb system in monazite and produced hybrid ages. They further pointed out that the monazite alteration occurred at ~125 Ma and was coeval with gold mineralization. However, the time of monazite alteration is largely uncertain. Further, the sample for monazite dating

consists of quartz, molybdenite, monazite, and pyrite, without gold mineralization (Li et al., 2011). Therefore, there is no petrographic evidence to link the monazite alteration process to gold mineralization. Considering the close spatial association between gold and molybdenite (i.e., gold and molybdenite often appear together on the hand specimen scale and molybdenite is widespread in gold orebodies), we believe that Re-Os molybdenite ages give a best estimate of the time of gold mineralization until more reliable geochronological data from minerals cogenetic with gold are available. In conclusion, we propose molybdenum mineralization occurred during the Late Triassic, which is constrained by the Re-Os molybdenite ages of 232.9 ± 2.7 to 207.1 ± 3.1 Ma and SHRIMP U–Th–Pb monazite ages of 216 ± 5 Ma. The time of gold mineralization is not well constrained, most likely also in the Late Triassic.

*3.5.2 Grey quartz*

Fine-grained, anhedral gray quartz is present both in the molybdenum and gold ores at this deposit. The gray quartz has long been considered as an important indicator for gold mineralization in the Xiaoqinling region. Earlier studies propose that the gray quartz represent another quartz deposition stage after the initial precipitation of the buck white quartz, which forms the main part of the quartz vein systems. Microscopic work of this study, however, reveals that the gray quartz results from the fracturing and recrystallization of the early buck white quartz rather than precipitation of new quartz. The presence of abundant fine-grained sulfides gives it a gray appearance. On the other hand, if sulfides are rare or absent, the matrix quartz will be colorless and cleaner than the larger quartz fragments. This is because the milky white appearance of quartz is caused by a large number of fluid inclusions (Roedder. 1984), and the process of recrystallization will eliminate most of the fluid inclusions in quartz (Kerrich 1976), thus giving quartz a more transparent appearance.

*3.5.3 Conditions of telluride deposition*

The Dahu deposit has a large number of telluride minerals. The estimated $fTe_2$–$fS_2$ conditions of telluride mineralization are indicated in Figure 3.19, with log $fTe_2$ between -13 and -9 and log $fS_2$ between -15 and -11 for 250 ℃. The abundance of gold, tellurobismuthite, and tetradymite, the scarcity of calaverite, and the absence of native bismuth constrain the tellurium fugacity of stage III mainly between the $AuTe_2$–Au equilibrium line and the $Bi_2Te_3$–Bi equilibrium line. On the other hand, the absence of bismuthinite ($Bi_2S_3$) suggests that $fS_2$ is lower than defined by the $Bi_2Te_3$–$Bi_2S_3$ equilibrium line. The scarcity of pyrrhotite

suggests that $fS_2$ is mostly buffered within the pyrite stability field by the abundant pyrite.

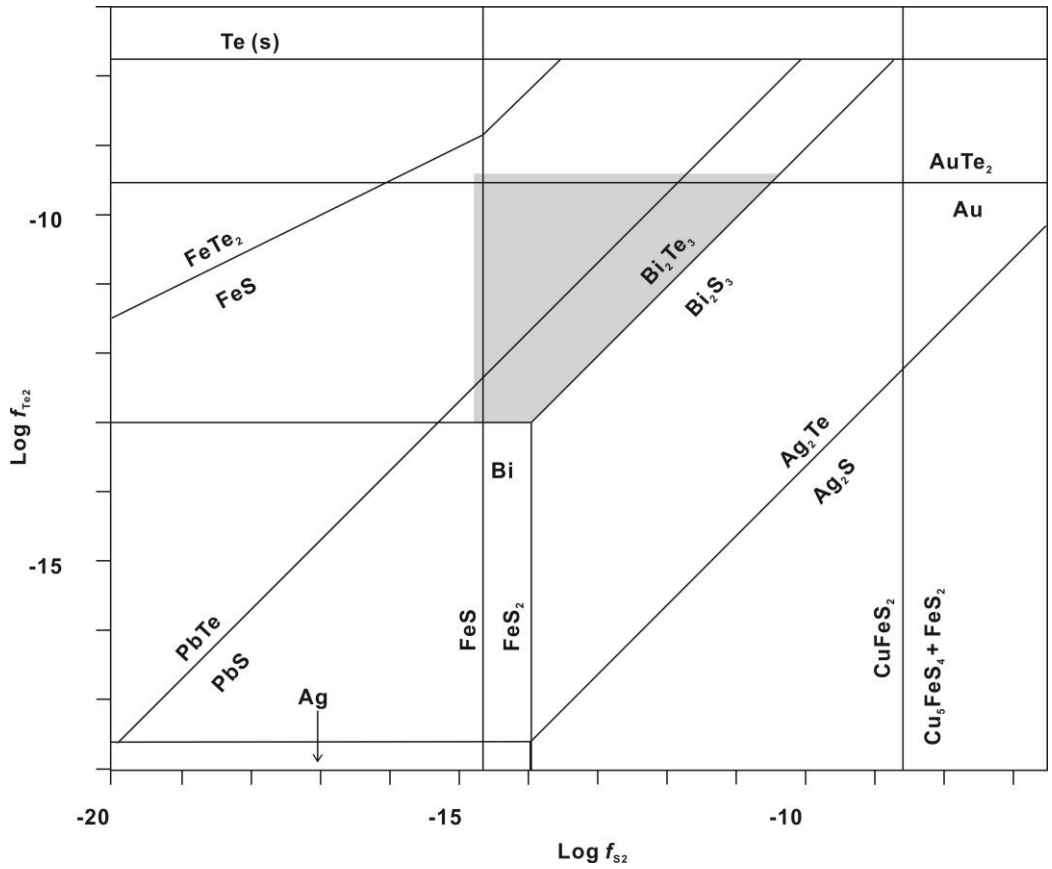


FIG. 3.19. Sulfur versus tellurium fugacity diagram with selected sulfide-telluride equilibria at 250 ℃ (modified from Afifi et al 1988; Plotinskaya et al., 2006). Shaded area indicates $f_{Te2}$-$f_{S2}$ conditions of the sulfide–telluride–sulfosalt–gold stage.

### *3.5.4 Interpretation of fluid inclusions*

*Origin of fluid inclusions:* The $H_2O$-$CO_2$ fluid inclusions occur in various populations in both stage I and stage III quartz. They occur as planar groups outlining healed fractures that come to the surface of quartz crystals or terminate within quartz crystals (Fig. 3.9A, 3.10A, 3.11A), suggesting they are either secondary or pseudosecondary in origin. Many reasons can cause a natural crystal to be fractured during its growth (yielding pseudosecondary inclusions) or afterward (yielding secondary inclusions): solid inclusions whose compressibility or thermal-expansion characteristics differ from those of the host, crystal misfit along lineage growth, thermal shock, mechanical stress from distortion of the base where attached, etc. (Roedder, 1984). Some $H_2O$-$CO_2$ fluid inclusions also appear as random, three-dimensional distributions within quartz crystals (Fig. 3.9A), suggesting a possible primary origin. However,

this is not definite, because overprinting of several secondary or pseudosecondary fluid inclusion trails can also result in a random, three-dimensional distribution of fluid inclusions. Despite the complex occurrences of the $H_2O$-$CO_2$ fluid inclusions, we propose that the $H_2O$-$CO_2$ fluid inclusions represent the ore-forming fluids, while the $H_2O$ fluid inclusions are all secondary in origin, post-date the $H_2O$-$CO_2$ fluid inclusions, and represent the post-mineralization fluids, based on the following reasons: (1) minerals (e.g., molybdenite, pyrite, chalcopyrite, anhydrite, celestine) present as solids in $H_2O$-$CO_2$ fluid inclusions in stage I quartz also occur as mineral inclusions in stage I quartz, and opaque solids, probably sulfides, are also present in $H_2O$-$CO_2$ fluid inclusions in stage III quartz, but solids have not been observed in the $H_2O$ fluid inclusions; (2) total homogenization temperatures of the $H_2O$-$CO_2$ fluid inclusions are systematically higher than those of the $H_2O$ fluid inclusions (Table 3.8), and this is also true for the microthermometric data of Ni et al. (2008) ($H_2O$-$CO_2$ fluid inclusions: 225 to 503 ℃; $H_2O$ fluid inclusions: 227 to 251 ℃); (3) the $H_2O$ fluid inclusions all occur as planar groups, which locally cut the $H_2O$-$CO_2$ fluid inclusion planes (Fig. 3.10); (4) negative crystal shape $H_2O$-$CO_2$ fluid inclusions are common in both stage I and stage III quartz (e.g., Fig. 3.9D,E, 3.10C, 3.11B, C, E), but the $H_2O$ fluid inclusions all have a thin and flat shape (Fig. 3.10A, B), suggesting that the $H_2O$ fluid inclusions were trapped later and at lower temperature, because healing of fractures in quartz first yields thin and flat fluid inclusions, and subsequent recrystallization (i.e., dissolution and re-precipitation) of quartz tends to reduce the surface energy of fluid inclusions by producing fluid inclusions with more regular or equant shapes (e.g., negative crystal shape) (Roedder, 1984); at low temperatures, the low solubilities of quartz in water result in low recrystallization rates of quartz, enabling the flat and immature shape of secondary fluid inclusions to be preserved.

*Scatter of fluid inclusion data*: The $H_2O$-$CO_2$ fluid inclusions have variable $CO_2/H_2O$ ratios and scattered microthermometric data (especially total homogenization temperatures). Fluid unmixing, sequential trapping of fluid inclusions under varying P-T conditions, and post-entrapment re-equilibration of fluid inclusions, can all account for the large variation in $CO_2/H_2O$ ratios and microthermometric data. Fluid unmixing is often used to explain the variable $CO_2/H_2O$ ratios of fluid inclusions in gold-bearing quartz veins of the Xiaoqinling region (e.g., Fan et al., 2003; Ni et al., 2008; Li et al., 2012b). We agree that fluid unmixing is a possible mechanism resulting in fluid inclusions with variable $CO_2/H_2O$ ratios. For example, fluid inclusions with high and low $CO_2/H_2O$ ratios occur in the same fluid inclusion assemblage and show similar shape and orientation (Fig. 3.11E), suggesting these fluid inclusions may represent heterogeneous entrapment of unmixing fluids. Indeed, considering

that the solubility of $CO_2$ in water generally decreases with decreasing temperature and pressure, unmixing of $CO_2$ from a $CO_2$-rich fluid is very likely during the ore-forming process. However, we believe that the roles of sequential trapping of fluid inclusions under varying P-T conditions and post-entrapment re-equilibration of fluid inclusions have been underestimated. For example, primary, pseudosecondary, and secondary $H_2O$-$CO_2$ fluid inclusions are present in the same quartz crystal (Fig. 3.9A), suggesting sequential trapping of $H_2O$-$CO_2$ fluid inclusions at different times, and different generations of $H_2O$-$CO_2$ fluid inclusions can have different compositions and total homogenization temperatures. Re-equilibration textures (Vityk and Bodnar, 1995), such as tiny fractures or planes of small fluid inclusions extending from large fluid inclusions (Fig. 3.9C), and necking down of fluid inclusions after phase separation (Fig. 3.9K), are often present. The earlier texture suggests that fluid inclusions have undergone partial leakage, which can change the densities and $CO_2/H_2O$ ratios of fluid inclusions, and accordingly, the total homogenization temperatures. Necking down after separation of the $H_2O$ and $CO_2$ phases can produce smaller fluid inclusions with variable $CO_2/H_2O$ ratios, and, accordingly, a range in total homogenization temperatures. However, the textural evidence of re-equilibration may not be large enough to be observed, and can even be eliminated because of sufficient recrystallization (i.e., dissolution and re-precipitation) of quartz (Roedder, 1984). Formation of the Xiaoqinling core complex in the Early Cretaceous (Wang and Mao, 2002; Zhang et al., 2003) may have resulted in a nearly isothermal decompression process, which can cause large internal overpressure of fluid inclusions, and subsequent re-equilibration of fluid inclusions by partial leakage or necking down.

### *3.5.5 Interpration of Uv-Fs-LA-ICP-MS data*

*Concentrations of Mo and Au*: The ore fluids of the Dahu deposit contain less than 1 ppm of Mo (detection limit of Mo is between 0.1 and 1 ppm in this study). This value is not only much lower than Mo concentrations reported in the fluids of porphyry Mo deposits (200–400 ppm) or porphyry Cu-(Mo-Au) deposits (10–600 ppm), but also lower than Mo concentrations reported in the fluids of barren granite (5–90 ppm; Audétat et al., 2008 and references therein). Low Mo concentrations may indicate that the analyzed fluids are not responsible for Mo mineralization. However, this explanation seems unlikely, because $H_2O$-$CO_2$ fluid inclusions always dominate fluid inclusion populations in molybdenite mineralized quartz veins. Under microscope, molybdenite shows close spatial associations with $H_2O$-$CO_2$ fluid inclusions in stage I quartz, and molybdenite was also observed as solid in one opened fluid inclusion (Fig. 3.13C). Therefore, perhaps most Mo, together with Cu, was lost from the fluids we analyzed

before trapping, by precipitation of molybdenite and copper sulfides. This assumption is supported by the fact that solids (e.g., covellite, $Cu_{1.65}S$, bornite, molybdenite, celestine) are abundant in $H_2O$-$CO_2$ fluid inclusions in stage I quartz, but solid-free fluid inclusions, even in the same fluid inclusion assemblage with solid-bearing fluid inclusions, always show quite low metal concentrations. Another possibility is that fluids without enriched Mo concentrations are capable of forming a Mo deposit. For example, Mo concentrations in the ore fluids of the Butte porphyry Cu-Mo deposit are also all below the detection limit of 5 to 20 ppm (Rusk et al., 2004).

Although Au was detected in one fluid inclusion with a value of 1 ppm, this value is suspicious, probably also artefacts (as discussed before, element concentrations for individual fluid inclusions with errors >50% and without visible peak in the time-resolved ICP-MS signal are considered as artifacts and have already been excluded), as no visible peak in the time-resolved ICP-MS signal has been observed. Therefore, we consider that Au concentrations in the ore fluids of the Dahu deposit are all below the detection limit of 0.2 to 2 ppm. Nevertheless, fluids with only 10 to 15 ppb of Au are considered to be capable of forming a gold deposit (e.g., Sibson and Scott, 1998; Simmons and Brown, 2006).

*Comparisons with other hydrothermal systems:* Compared to metamorphic fluids (e.g., Marsala et al., 2013; Miron et al., 2013; Rauchenstein-Martinek et al., 2014), the ore fluids of the Dahu deposit show higher salinities and higher concentrations of most elements (Na, K, Mn, Zn, Rb, Pb), while Sr and Cu concentrations are mostly within the ranges reported for metamorphic fluids. Among all the elements, the Dahu ore fluids show notably higher Rb concentrations varying between 21 and 83 ppm, while Rb concentrations in metamorphic fluids range from 0.6 to 9 ppm. Further, the Na/K weight ratios of the Dahu ore fluids (Na/K: 1–6) are significantly lower than those of metamorphic fluids (Na/K: 26–94).

The Dahu ore fluids resemble the ore fluids of orogenic gold deposits (e.g., Yardley et al., 1993; Hodge, 2010; Garofalo et al., 2014) by similar concentrations of most elements (Li, B, Na, Mn, Fe, Cu, Zn, Sr, Pb) and elevated $CO_2$ contents. However, like metamorphic fluids, orogenic gold deposit ore fluids show lower Rb concentrations (1–17 ppm) and higher Na/K ratios (2–181) than the Dahu ore fluids, as well as lower Cs concentrations (1–5 ppm) and higher Ba concentrations (10–68 ppm).

In the K vs. Rb and Na/K vs. Na + K diagrams (Fig. 3.20), the Dahu ore fluids clearly differ from metamorphic fluids and orogenic gold deposit ore fluids, but show close affinities to the ore fluids of magmatic-hydrothermal deposits (e.g., porphyry and intrusion-related deposits). However, the Dahu ore fluids also differ from magmatic-hydrothermal ore fluids by containing

much higher $CO_2$ contents and much lower concentrations of Fe, Mn, Cu, Zn, and Mo. These elements typically show enrichment factors of 10–1000 against their crustal averages in magmatic-hydrothermal ore fluids (e.g., Ulrich et al., 2002; Rusk et al., 2004; Klemm et al. 2007, 2008; Audétat et al., 2008; Stefanova et al., 2014), but are close to or lower than their crustal averages in the Dahu ore fluids. It is noted, however, that the ore fluids of intrusion-related gold deposits in the Tintina Gold Province of Alaska and Yukon show similar low concentrations of these elements and elevated $CO_2$ contents (Ridley, 2008? Ridley and Gibson, 2011;).

In summary, the Dahu ore fluid compositions clearly differ from metamorphic fluid compositions, but show both similarities and differences with those reported from orogenic gold deposits and magmatic-hydrothermal deposits.

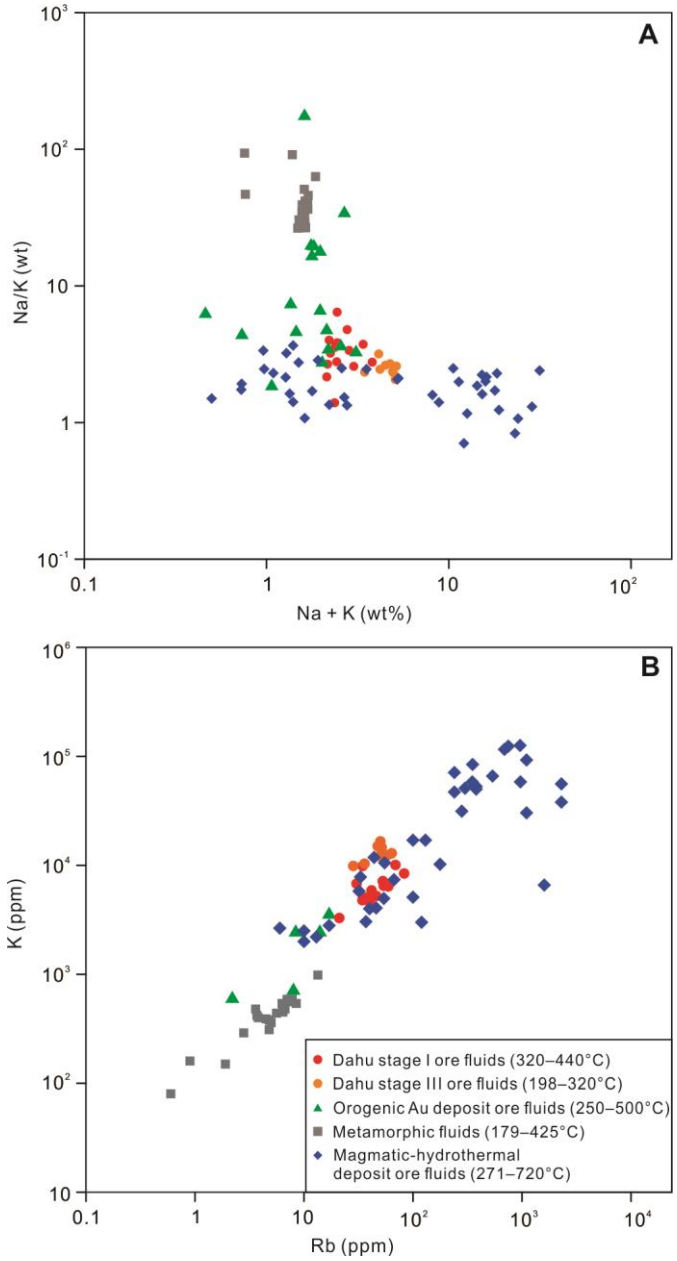


FIG. 3.20. Fluid compositions of the Dahu deposit compared to other hydrothermal systems. **A**. Fluid compositions plotted in Na/K vs. Na + K. **B**. Fluid compositions plotted in K vs. Rb space. Estimated trapping temperatures for fluid inclusions are shown in brackets. Data for orogenic Au deposit ore fluids are from Yardley et al. (1993), Hodge (2010), and Garofalo et al. (2014), for metamorphic fluids are from Marsala et al. (2013), Miron et al. (2013), for magmatic-hydrothermal deposit (i.e., porphyry and intrusion-related deposit) ore fluids are from Ulrich et al. (2002), Rusk et al. (2004), Klemm et al. (2007, 2008), Audéat et al. (2008), Stefanova et al. (2014).

*3.5.6 Temperature and pressure of mineralization*

Total homogenization temperatures of the $H_2O$-$CO_2$ fluid inclusions in stage I and stage III quartz range from 230 to 440 ℃ and 198 to 320 ℃, respectively. As discussed above, the wide temperature range may partly result from secondary $H_2O$-$CO_2$ fluid inclusions, but it is not always possible to distinguish them from primary and pseudosecondary fluid inclusions during the microthermometric work. This is especially true for $H_2O$-$CO_2$ fluid inclusions in stage I quartz, because stage I quartz precipitated at the earliest stage, and fluids responsible for stage II and stage III mineralization can be trapped as secondary fluid inclusions in stage I quartz. This agrees with the total homogenization temperature frequency histogram of $H_2O$-$CO_2$ fluid inclusions in stage I quartz, which shows two distinct modes at 245 ℃ and 375 ℃, respectively. The mode at 245 ℃ is likely caused by secondary $H_2O$-$CO_2$ fluid inclusions, while the mode at 375 ℃ may result from primary and pseudosecondary $H_2O$-$CO_2$ fluid inclusions. Therefore, we propose stage I mineralization took place at between ~320 and 440 ℃, and stage III mineralization took place at between ~198 to 320 ℃. However, the estimated temperatures for mineralization should be treated with caution, because fluid inclusions may have undergone post-entrapment re-equilibration and total homogenization temperatures of fluid inclusions only represent the minimum trapping temperatures.

Fluid inclusion diameters can be used to estimate the minimum trapping pressure of fluid inclusions. The internal pressure of fluid inclusions for decrepitation is inversely related to fluid inclusion size according to the equation of Bodnar et al. (1989): $\mathbf{P = 4.26\ \boldsymbol{D}^{-0.432}}$, $P$ is the pressure in kbars required to decrepitate fluid inclusions in quartz under one atmosphere confining pressure, whereas $D$ is the fluid inclusion diameter in micrometers. Because all $H_2O$-$CO_2$ fluid inclusions larger than 16 μm in diameter decrepitated before total homogenization (Fig. 3.14F, 3.15F), we assume that the decrepitation pressure for a 16 μm fluid inclusion, 1.3 kbars, approximately represents the minimum trapping pressure for the $H_2O$-$CO_2$ fluid inclusions. Assuming a lithostatic environment and an overlying rock density of 2.8 g/cm$^3$, this pressure corresponds to a minimum formation depth of 4.7 km. Quartz vein fabrics can also be used to broadly identify the P-T conditions during vein development (e.g., Dowling and Morrison, 1989). At the Dahu deposit, quartz veins are characterized by an anhedral buck-quartz texture and well-developed superimposed textures (e.g., breccia texture, recrystallization texture, and deformation texture). These textures are clearly different from quartz-vein textures of gold deposits in a shallow environment. For example, porphyry gold deposits (formation depth <5 km; Groves et al., 1998) are characterized by comb-textured

quartz with rare superimposed textures (Dowling and Morrison, 1989), whereas epithermal gold deposits (formation depth <2 km; Hedenquist and Lowenstern, 1994; Groves et al., 1998) are characterized by multiple generations of chalcedonic, microcrystalline, and comb-textured quartz disposed as crustiform and colloform bands, and cockade overgrowths (Dowling and Morrison, 1989). Conversely, quartz veins up to 10 m in width and breccias are characteristic of a brittle environment. Therefore, we expect that quartz veins at Dahu are typical of veins developing within the seismogenic regime (i.e., <10–15 km; Sibson, 1986) and suggest that the Dahu deposit formed at 5–10 km depth.

*3.5.7 Remarks on possible fluid sources*

The stable isotope data of stage I quartz are characterized by uniform $\delta^{18}O$ values of quartz, and low and scattered δD values of fluid inclusion waters. We propose that the δD values reflect a mixture of ore-forming fluids trapped by the $H_2O$-$CO_2$ fluid inclusions at deep crustal levels, and post-mineralization fluids, possibly meteoric waters, trapped by the secondary $H_2O$ fluid inclusions at higher crustal levels during uplift of the Xiaoqinling core complex. This phenomenon is common for fluid inclusions extracted from vein quartz in metamorphic terrain (e.g., Pickthorn et al., 1987; Goldfarb et al., 1991), because multiple periods of fracturing and rehealing of quartz can result in relatively large populations of secondary fluid inclusions. Although the quartz samples for hydrogen isotope analysis in this study were initially outgassed at 105 ℃ for 12 hours to release labile volatiles and secondary fluid inclusions, total homogenization temperatures (143–159 ℃) of the secondary $H_2O$ fluid inclusions in stage I quartz suggest these fluid inclusions would not decrepitate during the degassing process. In contrast, because the high activation energy for diffusion of oxygen in quartz inhibits isotopic exchange at temperatures below about 600 ℃ (Giletti and Yund, 1984; Stein and Hannah, 1985), the $\delta^{18}O$ values of quartz are unaffected by the post-mineralization fluids. The $\delta^{18}O_{fluid}$ values are calculated by the quartz-water fractionation equation of Matsuhisa et al. (1979) for a temperature of 375 ℃. The calculated $\delta^{18}O_{fluid}$ values range from 5.6 to 7.4‰, and are within the range of both magmatic and metamorphic waters, but are much higher than the $\delta^{18}O$ values of meteoric waters (Fig. 3.21).

A metamorphic fluid origin from devolatilization of the basement rocks seems unlikely. First, the Sr–Nd isotope systematics of the ore sulfides at the Dahua deposit are far less radiogenic than those of the Archean Taihua rocks (Ni et al., 2012); the ore-forming fluids must ultimately stem from a more primitive source. For example, sixteen sulfide samples yield εNd(t) values between -13.5 and -18.1 (average: -15.1) and initial $^{87}Sr/^{86}Sr$ ratios of 0.705–0.713 (average:

0.709), while five Archean Taihua rock samples have εNd(t) values between −20.0 and −31.1 (average: −25.1) and initial $^{87}Sr/^{86}Sr$ ratios of 0.709–0.732 (average: 0.723) (Ni et al., 2012). Second, the refractory Archean Taihua rocks have a low content of volatiles (0.75–2.6 wt% LOI; Luan et al., 1985). Most volatiles of these rocks probably have been released during the regional amphibolite-facies metamorphism in the Paleoproterozoic (Zhou et al., 1998; Ni et al., 2003; Li et al., 2007b). In addition, trace element concentrations in the ore-forming fluids of the Dahu deposit are clearly different from those of metamorphic fluids (Fig. 3.20).

Based on the Sr–Nd isotope data, Ni et al. (2012) proposed that the ore-forming fluids directly originated from devolatilization of a subducting oceanic slab, and by interaction of the ore-forming fluids with the radiogenic Archean Taihua rocks yielding an enriched-mantle like Sr–Nd isotope signature. They further pointed out that the Mianlue Ocean between the North China Craton and the Yangtze Craton was not yet closed during the Late Triassic, and that subduction was still active. This model, however, disagrees with the widely accepted idea that the final collision between the North China Craton and the Yangtze Craton occurred during the Triassic (e.g., 242 to 227 Ma: Wu et al., 2006), and that the Qinling–Dabie Orogen evolved into a post-collisional extensional domain during the Late Triassic. Further, fluids derived from devolatilization of a subducting oceanic slab are likely to be soaked up by the mantle wedge via serpentinization, rather than migrating directly into the crust through many tens of kilometers (Phillips and Powell, 2009). Also, if the ore-forming fluids directly originated from devolatilization of the subducting oceanic slab, their oxygen fugacity would be buffered by interaction with the relatively reduced crustal rocks (e.g., the Archean Taihua rocks have no sulfate-bearing evaporites and are locally rich in graphite: Cai and Su, 1985) because of their long travel distance in the crust and the low water/rock ratio during this travel, contrasting with the oxidized fluid environment of the Dahu deposit (see discussion below).

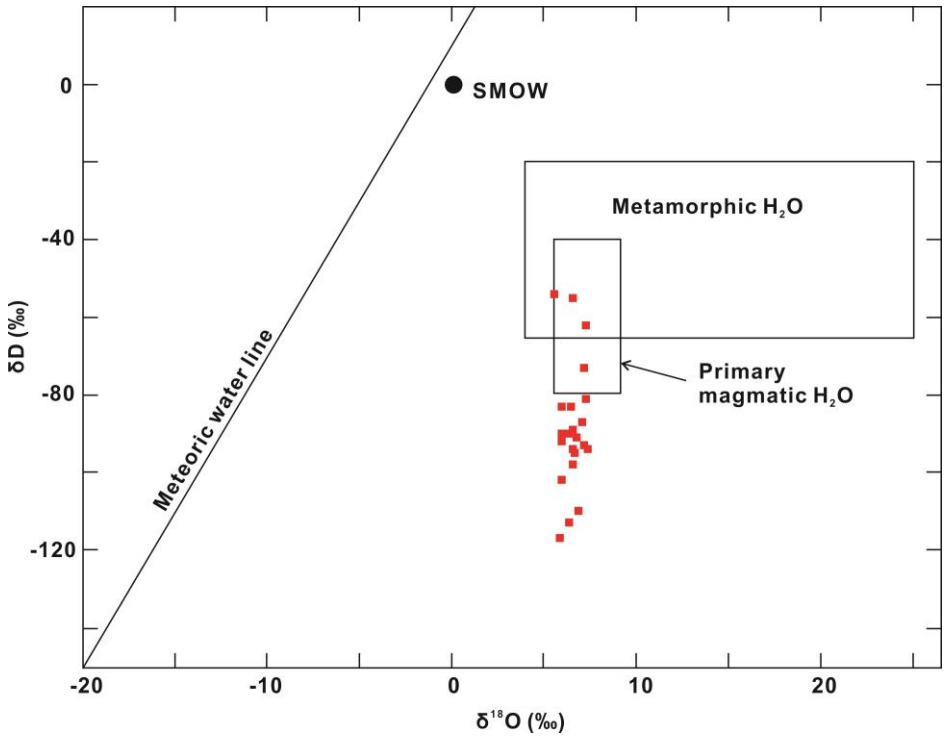


FIG. 3.21. Plot of $\delta^{18}O$ versus δD showing the calculated composition for the ore-forming fluids of the Dahu Au-Mo deposit. Metamorphic water field, primary magmatic water filed, and meteoric water line are from Taylor (1974).

# Chapter 4

# Telluride and Bi-sulfosalt Mineralogy of the Yangzhaiyu Au Deposit

## 4.1 Deposit geology

The Yangzhaiyu Au deposit is located about 10 km southwest of the Dahu deposit (Figs. 1.2, 4.1), and is one of the largest gold deposits in the Xiaoqinling region, with a proven reserve of 34.4 t Au (mean grade of 11.4 g/t Au) (Mao et al., 2002). Gold mineralization is controlled by a series of quartz veins. The S60 quartz vein is the largest gold-bearing quartz vein at the Yangzhaiyu Au deposit. It is 0.3 to 7 m wide and extends more than 4 km in a roughly east–west direction, dipping to the south. Traditionally, mineralization of the Yangzhaiyu Au deposit has been divided into four stages: an initial quartz–pyrite stage characterized by milky quartz and minor coarse-grained euhedral pyrite, a pyrite-dominated stage characterized by fine-grained pyrite and small amounts of gold, a base-metal sulfide stage characterized by abundant galena and chalcopyrite, and accessory gold, tellurides, and Bi-sulfosalts, and a final barren carbonate-dominated stage (e.g., Li SM et al., 1996, Mao et al., 2002, Li JW et al., 2012b). The quartz-vein systems formed from $CO_2$-rich, low- to moderate-salinity fluids (Li et al., 2012b), and are attributed to the class of orogenic gold deposits (Mao et al., 2002). Four $^{40}Ar/^{39}Ar$ plateau ages of ore-related biotite and sericite range from 134.5 $\pm$ 0.7 to 123.7 $\pm$ 0.5 Ma (Li et al., 2012b), suggesting an Early Cretaceous age.

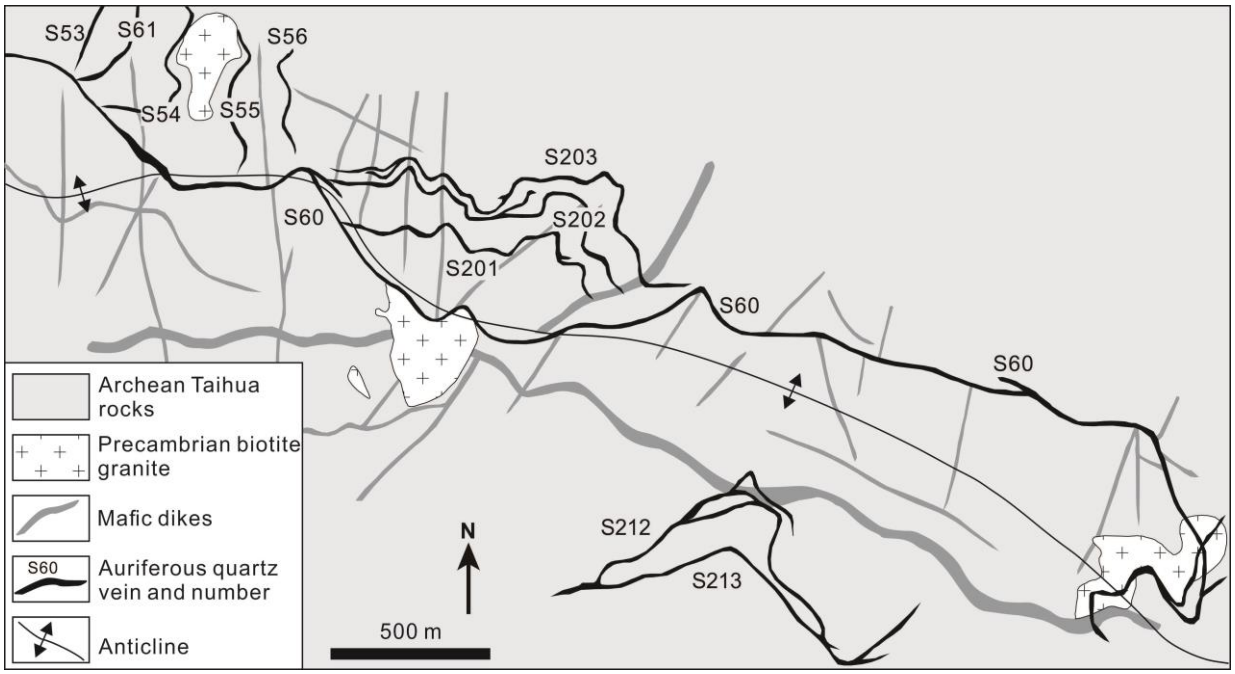


FIG. 4.1. Geologic map of the Yangzhaiyu Au deposit (after Song et al., 1980, Li et al., 2012a).

## 4.2 Sample material and analytical techniques

Ore samples were collected underground from different levels of the S60 gold-bearing quartz vein at the Yangzhaiyu Au deposit, with elevations ranging from 892 to 1936 m above NN. The telluride mineralogy was studied in fourteen selected polished sections by reflected-light microscopy.

Electron back-scattering diffraction (EBSD) and scanning electron microscope (SEM) analyses were carried out at Clausthal University of Technology, Germany, using a FEI Helios NanoLab FIB-SEM platform. Electron backscatter diffraction (EBSD) is a microstructural-crystallographic technique used to examine the crystallographic orientation of many materials. EBSD can provide quantitative microstructural information about the crystallographic nature of metals, minerals, semiconductors, and ceramics. It reveals grain size, grain boundary character, grain orientation, texture, and phase identity of the sample under the beam. EBSD is important for the characterization of new minerals, in a situation where grains are too small/rare to be analysed by X-ray methods (Maitland and Sitzman 2007; Prior et al., 2009). Electron back-scattering diffraction analysis was performed at 20 kV and 2.8 nA. Other parameters were as follows: magnification = 10000, horizontal field width of the image (HFW) = 25.6 μm, TiltAngle = 70.00, TiltAxis = 0.00. For scanning electron microscope analysis, a

low-voltage high-contrast detector (vCD) was used for scanning electron imaging at 5 kV and 0.17 nA. The scanning electron microscope is equipped with an energy-dispersive X-ray detector. Electron microprobe (EPMA) analyses were carried out at Clausthal University of Technology, Germany, using a Cameca SX100 electron microprobe. Analytical conditions, reference materials, and X-ray emission lines were as follows: 20 kV and 20 nA, and beam size of 1 μm; pure metals for Bi*Mα*, Ag*Lα*, Au*Lα*, and Cu*Kα*, PbTe for Pb*Mα* and Te*Lα*, $FeS_2$ for Fe*Kα* and S*Kα*. $FeS_2$ is natural pyrite; other reference materials are synthetic materials.

### 4.3 Ore mineralogy

Tellurides, Bi-sulfosalts, and associated ore minerals occur as fracture-fillings, irregular patches, and composite inclusions within pyrite and quartz. Twelve telluride and four Bi-sulfosalt phases were identified. Tellurides include sylvanite [$(Au,Ag)_2Te_4$], hessite [$Ag_2Te$], petzite [$Ag_3AuTe_2$], calaverite [$AuTe_2$], stützite [$Ag_{5-x}Te_3$], rucklidgeite [$PbBi_2Te_4$], altaite [PbTe], volynskite [$AgBiTe_2$], tellurobismuthite [$Bi_2Te_3$], tetradymite [$Bi_2Te_2S$], buckhornite [$AuPb_2BiTe_2S_3$], and Phase A – an unnamed Ag-telluride with the empirical formula of $AgTe_3$. Bi-sulfosalts include aikinite [$PbCuBiS_3$], felbertalite [$Cu_2Pb_6Bi_8S_{19}$], wittichenite [$Cu_3BiS_3$], and Phase B – an unnamed Bi-sulfosalt with the empirical formula of $Cu_{20}FePb_{11}Bi_9S_{37}$. Ore minerals spatially associated with tellurides and Bi-sulfosalts are chalcopyrite, galena, bornite, sphalerite, gold, and native tellurium. Tellurides, Bi-sulfosalts, and associated ore minerals occur in the following commonly observed assemblages: Phase A + sylvanite + chalcopyrite (e.g., Figs. 4.2, 4.3, 4.4), sylvanite + native tellurium + stützite (e.g., Fig. 4.6E, F), rucklidgeite + altaite + volynskite ± hessite ± petzite (e.g., Fig. 4.6A), rucklidgeite + gold ± altaite (e.g., Fig. 4.7A), hessite + petzite ± sylvanite (e.g., Fig. 4.6C), petzite + sylvanite, calaverite + gold + petzite ± chalcopyrite ± tellurobismuthite/rucklidgeite (e.g., Fig. 4.7B, C), tetradymite + felbertalite, and tetradymite + gold.

Tellurides and Bi-sulfosalts commonly appear in different contact assemblages, but tetradymite has been observed to occur in contact with felbertalite and aikinite, and Phase B has been observed in the same assemblage with hessite. Cross-cutting relations among different mineral assemblages are rare, trails of Phase A-bearing composite inclusions are locally cut by fractures filled by Bi-telluride-bearing assemblages (e.g., rucklidgeite-bearing assemblage, Fig.

4.3A–C) and gold (Fig. 4.2F). Within individual assemblages, minerals often display intergrowth textures, such as triple joint junctions (Figs. 4.2, 4.3D, 4.5A–C, 4.6B, E, F) and mutual curvilinear boundaries (Fig. 4.6G). Sylvanite, however, locally occurs as minute graphic blebs within hessite or petzite (Fig. 4.6C), and gold and calaverite locally occur as rounded inclusions within petzite (Fig. 4.7B).

### *4.3.1 Tellurides*

*Phase A:* $AgTe_3$ has been synthesized by Range et al. (1982), but its natural occurrence has not been reported so far. In this study, we have observed Phase A (Figs. 4.2, 4.3, 4.4), with the empirical formula of $AgTe_3$, in five polished sections from two gold ore samples. Electron back-scattering diffraction (EBSD) images (Fig. 4.4) of Phase A were successfully obtained from three different Phase A grains. Phase A shows golden reflection color, without discernable reflectance pleochroism or anisotropy. It occurs in small intergrowth composites (<20 μm) commonly consisting of Phase A, sylvanite, and chalcopyrite, and locally of bornite, galena, and altaite in healed micro-fractures in pyrite. Although Bi-tellurides and Bi-sulfosalts are widespread in our sample set, Phase A has not been observed to occur in assemblages with them. Electron microprobe data of 17 Phase A grains yield 74.8 to 76.7 wt.% Te and 20.8 to 22.0 wt.% Ag. Atomic ratios of Te/Ag vary from 2.87 to 3.06, with an average value of 3.00 (Table 4.1). All the analyzed Phase A grains contain small amounts of Fe and S (<2 wt.%), which are probably caused by contamination of adjacent pyrite, because the Phase A grains are small (<20 μm) and always occur as inclusions in pyrite. Some Phase A grains contain trace amounts of Cu (0.1–0.6 wt.%). This is likely a result of contamination by adjacent copper sulfides, because seven out of eight grains of Phase A containing Cu are in assemblages with chalcopyrite and/or bornite.

*Altaite:* Altaite [PbTe] is widespread and one of the most abundant tellurides in our sample set. It has two major occurrences, i.e., as isolated grains within galena, or in assemblages with a variety of minerals, including rucklidgeite, volynskite, gold, hessite, stützite, sylvanite, petzite, Phase A, chalcopyrite, and galena (Figs. 4.2C, E, G, 4.6A, 4.7A, B). Altaite locally forms lamellae in rucklidgeite, suggesting that some altaite exsolved from the $(Bi,Sb)_2Te_3$–PbTe solid solution (Kase et al., 1993).

*Buckhornite*: Buckhornite [$AuPb_2BiTe_2S_3$] is a rare Au-Pb-Bi sulfotelluride. Only one grain of buckhornite was identified in this study. It occurs in a contact assemblage consisting of bornite, chalcopyrite, galena, hessite, and Phase B (Fig. 4.5). Buckhornite displays moderate reflectance pleochroism, with reflection colors varying from brownish grey to greenish grey and bluish grey.

TABLE 4.1. Electron microprobe data of $AgTe_3$

| | wt.% | | | | | | | Atomic ratio |
|---|---|---|---|---|---|---|---|---|
| | S | Ag | Cu | Te | Fe | Pb | Total | Te/Ag |
| 1 | 0.66 | 21.12 | 0.19 | 75.97 | 1.50 | <0.27 | 99.44 | 3.04 |
| 2 | 0.26 | 21.50 | <0.13 | 76.73 | 1.32 | <0.23 | 99.81 | 3.02 |
| 3 | 0.21 | 21.67 | <0.13 | 76.55 | 1.39 | <0.25 | 99.82 | 2.99 |
| 4 | 0.16 | 20.94 | 0.17 | 75.49 | 1.35 | <0.26 | 98.11 | 3.05 |
| 5 | 0.22 | 20.96 | <0.12 | 75.77 | 1.40 | <0.24 | 98.35 | 3.06 |
| 6 | 0.37 | 21.42 | <0.13 | 76.44 | 1.61 | <0.24 | 99.84 | 3.02 |
| 7 | 0.12 | 21.64 | <0.12 | 76.29 | 1.04 | <0.25 | 99.09 | 2.98 |
| 8 | 0.50 | 21.43 | <0.12 | 76.25 | 1.93 | <0.25 | 100.11 | 3.01 |
| 9 | 0.52 | 20.99 | 0.14 | 75.87 | 1.56 | <0.25 | 99.08 | 3.06 |
| 10 | 0.52 | 21.35 | <0.12 | 75.60 | 1.88 | 0.27 | 99.62 | 2.99 |
| 11 | 1.29 | 21.00 | <0.13 | 74.99 | 1.87 | <0.24 | 99.15 | 3.02 |
| 12 | 0.30 | 21.49 | 0.16 | 75.97 | 1.58 | <0.24 | 99.50 | 2.99 |
| 13 | 0.85 | 22.00 | 0.62 | 74.79 | 1.94 | <0.29 | 100.20 | 2.87 |
| 14 | 0.65 | 21.39 | 0.29 | 75.04 | 1.97 | <0.29 | 99.34 | 2.97 |
| 15 | 0.22 | 21.79 | <0.13 | 76.37 | 1.56 | <0.29 | 99.94 | 2.96 |
| 16 | 0.39 | 21.19 | 0.25 | 75.59 | 1.39 | <0.31 | 98.81 | 3.02 |
| 17 | 0.48 | 20.83 | 0.13 | 75.11 | 1.46 | 2.10 | 100.11 | 3.05 |

Gold and Bi are below the detection limits of 0.26–0.49 wt.% Au and 0.27 wt.% Bi, respectively.

*Calaverite*: Calaverite [$AuTe_2$] mainly occurs in the calaverite + gold + petzite ± chalcopyrite ± tellurobismuthite/rucklidgeite assemblage (Figs. 4.2F, 4.6B, 4.7B, C). Calaverite always has a low but consistent Ag content, which ranges from 0.65 to 0.88 wt.% (Table 4.2).

*Hessite*: Hessite [$Ag_2Te$] is widespread and one of the most abundant tellurides in our sample set. It occurs as a major phase in the hessite + petzite ± sylvanite assemblage (Fig. 4.6C, D), or as a subordinate phase in the rucklidgeite + altaite + volynskite ± hessite ± petzite assemblage. Hessite also occurs in contact with gold, tellurobismuthite, and chalcopyrite.

*Petzite*: Petzite [$Ag_3AuTe_2$] mainly occurs in the hessite + petzite ± sylvanite assemblage and the calaverite + gold + petzite ± chalcopyrite ± tellurobismuthite/rucklidgeite assemblage. In the latter assemblage, petzite either forms straight boundaries with calaverite and gold (Fig. 4.7C), or encloses rounded grains of calaverite and gold (Fig. 4.7B). Some petzite analyses gave much lower Au content than ideal petzite (25.4 wt.%), most likely resulting from diffusion of Au away from the electron beam during electron microprobe analysis (Rucklidge and Stumpfl, 1968).

*Rucklidgeite:* Rucklidgeite [$PbBi_2Te_4$] appears pinkish white in reflected light. It is widespread and one of the most abundant tellurides in our sample collection. Rucklidgeite is intimately associated with altaite, and also occurs in contact with volynskite, hessite, petzite, gold, and calaverite (Figs. 4.6A, B, 4.7A, B). Rucklidgeite contains some Ag, its atomic ratio Bi/Pb is higher than the ideal stoichiometry (Table 4.2). On the other hand, the atomic ratio (Bi-Ag)/(Pb+2Ag) varies from 1.96 to 2.04, a tight range that can be explained by some incorporation of $Ag_2Te$ component giving the modified formula [$(Ag_xPb_{1-2x}Bi_{2+x})_3Te_4$] (Kase et al., 1993).

*Stützite*: Stützite [$Ag_{5-x}Te_3$] is rarely observed; it occurs in minute composite inclusions in pyrite, and in contact with native tellurium, sylvanite, chalcopyrite, and bornite (Figs. 4.2E, F, 4.6E, F).

*Sylvanite:* Sylvanite [$(Au,Ag)_2Te_4$] is a widespread telluride that rarely exceeds 20 μm across. Sylvanite occurs in contact with all the observed Au-Ag tellurides (petzite, hessite, stützite, and Phase A) but not with calaverite, and also occurs in contact with native tellurium, altaite, chalcopyrite, and bornite. In the Phase A + sylvanite + chalcopyrite and sylvanite + tellurium + stützite assemblages, sylvanite and other phases everywhere display intergrowth textures, such as mutual curvilinear boundaries and triple joint junctions (Figs. 4.2, 4.3, 4.4, 4.6E, F). Where found together with hessite and/or petzite, sylvanite commonly occurs as minute graphic blebs or larger inclusions in hessite or petzite (Fig. 4.6C). Sylvanite contains up to 1.5 wt.% Cu, supporting the suggestion by Bonev et al. (2005) that up to 15 atom.% of the Ag in sylvanite can be substituted by Cu.

*Tellurobismuthite:* Tellurobismuthite [$Bi_2Te_3$] often occurs as lath-shaped crystals, and in contact with a wide range of minerals, including gold, calaverite, petzite, hessite, tetradymite,

and volynskite (Figs. 4.6G, 4.7C). Although both tellurobismuthite and rucklidgeite occur in assemblages containing calaverite, gold, petzite, and chalcopyrite, the two tellurides have not been observed together.

*Tetradymite:* Tetradymite [$Bi_2Te_2S$] is rare in our sample set. It occurs in contact with gold, tellurobismuthite (Fig. 4.6G), and Bi-sulfosalts including felbertalite and aikinite.

*Volynskite:* Volynskite [$AgBiTe_2$] appears purplish white in reflected light. It often occurs in contact with rucklidgeite, altaite, and hessite, and occasionally with petzite, sylvanite, tellurobismuthite, galena, and chalcopyrite (Fig. 4.6A).

### *4.3.2 Bi-sulfosalts*

*Phase B*: One grain of an unnamed Bi-sulfosalt, Phase B, was observed (Fig. 4.5). It shows pinkish grey reflection color, without discernable reflectance pleochroism or anisotropy. Phase B is *ca.* 5 μm in width and *ca.* 20 μm in length, and occurs in a contact assemblage consisting of Phase B, hessite, galena, chalcopyrite, bornite, and buckhornite within pyrite (Fig. 4.5). Three analyses of Phase B give the following average composition: 34.9 wt.% Pb, 27.4 wt.% Bi, 18.4 wt.% Cu, 17.4 wt.% S, 1.1 wt.% Fe, and 0.6 wt.% Au (Table 4.2), with the empirical formula of $Cu_{20}FePb_{11}Bi_9S_{37}$ based on 78 atoms per formula unit. The remarkable character of Phase B, empirical $Cu_{20}FePb_{11}Bi_9S_{37}$, is that it contains 47 atomic % S. Among all the minerals containing Pb, Cu, Bi and S in their formula, only three have less than 50 atomic % of S: angelaite [$Cu_2AgPbBiS_4$] (44 atomic % S), larosite [$(Cu,Ag)_{21}PbBiS_{13}$] (36 atomic % S), and miharaite [$PbCu_4FeBiS_6$] (46 atomic % S). In addition, Chang and Hoda (1977) have reported a synthesized phase $Pb_{2.4}Bi_{2.3}Cu_{12.9}S_{12.3}$ with 41 atomic % S. The chemical composition of Phase B, however, is clearly different from the minerals mentioned above.

*Aikinite, felbertalite, and wittichenite*: Aikinite [$PbCuBiS_3$] occurs in contact with chalcopyrite, galena, and tetradymite, or as isolated grains within pyrite. Felbertalite [$Cu_2Pb_6Bi_8S_{19}$] occurs in contact with galena, tetradymite, and gold, or as isolated grain within pyrite (further study is required to confirm this, because felbertalite cannot normally be confirmed based on electron microprobe analysis alone). Wittichenite [$Cu_3BiS_3$] occurs in contact with chalcopyrite, bornite, and galena, and locally replaces bornite (Fig. 4.6D).

*4.3.4 Associated ore minerals*

*Gold*: Gold is a widespread minor mineral. It occurs in contact with a wide range of minerals, most commonly with rucklidgeite, less commonly with calaverite, hessite, petzite, altaite, chalcopyrite, galena, tellurobismuthite, tetradymite, and felbertalite (Figs. 4.2F, 4.7).

*Native tellurium*: Native tellurium is rare. It occurs in minute composite inclusions in pyrite, and always occurs in contact with sylvanite, and locally with chalcopyrite, bornite, and stützite (Figs. 4.2E, 4.6E, F). Both native tellurium and Phase A form mineral assemblages with sylvanite, and often occur adjacent to each other (Fig. 4.2E), but they have not been found to coexist in the same composite aggregate.

Bornite: Bornite [$Cu_5FeS_4$] is most commonly in contact with chalcopyrite, but was also found in contact with galena, wittichenite, native tellurium, stützite, Phase A, buckhornite, and Phase B (Figs. 4.2A, D, 4.5, 4.6D, F). Bornite locally contains up to 7.7 wt.% Bi (Table 4.2). This corresponds to the experimental work of Sugaki et al. (1984), which showed that bornite can incorporate up to 11.4 wt.% Bi at 300 ℃.

TABLE 4.2. Selected electron microprobe data of tellurides, Bi-sulfosalts, and bornite

| | 1 | 2 | 3 | 4 | 5 | 6 | 7 | 8 | 9 | 10 | 11 | 12 | 13 | 14 | 15 | 16 | 17 | 18 | 19 |
|---|---|---|---|---|---|---|---|---|---|---|---|---|---|---|---|---|---|---|---|
| wt.% | | | | | | | | | | | | | | | | | | | |
| S | <0.07 | 8.18 | <0.08 | <0.06 | <0.07 | 0.06 | 0.16 | 0.23 | 0.06 | 4.52 | 0.10 | 17.05 | 16.88 | 19.17 | 17.20 | 17.44 | 17.58 | 25.51 | 25.69 |
| Bi | 0.55 | 16.76 | <0.48 | <0.29 | <0.37 | 39.34 | <0.26 | <0.28 | 50.55 | 57.85 | 36.07 | 36.66 | 47.94 | 42.39 | 26.96 | 28.24 | 27.02 | 7.70 | 1.92 |
| Ag | 0.42 | <0.20 | 0.82 | 62.08 | 43.96 | 0.95 | 57.12 | <0.13 | 0.32 | <0.17 | 18.43 | <0.19 | 1.85 | <0.18 | <0.20 | <0.19 | <0.16 | <0.16 | <0.14 |
| Cu | <0.11 | <0.13 | <0.12 | <0.13 | <0.12 | <0.11 | <0.13 | <0.12 | <0.13 | <0.12 | <0.12 | 10.26 | 3.71 | 36.80 | 18.28 | 18.06 | 18.99 | 54.59 | 60.55 |
| Te | 37.46 | 21.41 | 57.46 | 37.18 | 32.81 | 43.60 | 41.69 | 99.08 | 47.24 | 35.78 | 44.81 | <0.17 | 0.45 | <0.14 | <0.17 | <0.15 | <0.14 | <0.11 | <0.12 |
| Au | <0.23 | 16.64 | 41.89 | <0.27 | 25.18 | <0.23 | <0.27 | <0.27 | <0.50 | <0.51 | <0.50 | <0.50 | <0.52 | <0.27 | 0.57 | 0.55 | 0.59 | <0.25 | <0.24 |
| Fe | 0.12 | 0.41 | <0.06 | <0.07 | <0.07 | 0.08 | 1.10 | 0.83 | <0.07 | <0.06 | 0.33 | 1.41 | 0.67 | 1.34 | 1.06 | 1.44 | 0.91 | 11.87 | 11.34 |
| Pb | 60.62 | 36.59 | <0.41 | <0.30 | <0.35 | 14.53 | <0.29 | <0.31 | 1.15 | <0.33 | <0.31 | 34.98 | 28.90 | <0.31 | 34.95 | 34.78 | 34.89 | <0.25 | <0.26 |
| Total | 99.17 | 99.99 | 100.17 | 99.26 | 101.95 | 98.56 | 100.07 | 100.14 | 99.32 | 98.15 | 99.74 | 100.36 | 100.40 | 99.70 | 99.02 | 100.51 | 99.98 | 99.67 | 99.50 |
| *apfu* | | | | | | | | | | | | | | | | | | | |
| S | – | 2.98 | – | – | – | 0.02 | 0.05 | 0.01 | 0.02 | 1.01 | 0.02 | 3.00 | 18.68 | 2.98 | 36.59 | 36.58 | 36.74 | 4.18 | 4.07 |
| Bi | 0.01 | 0.94 | – | – | – | 2.15 | – | – | 1.94 | 1.98 | 0.98 | 0.99 | 8.14 | 1.01 | 8.80 | 9.09 | 8.66 | 0.19 | 0.05 |
| Ag | 0.01 | – | 0.03 | 1.99 | 3.09 | 0.10 | 4.81 | – | 0.02 | – | 0.97 | – | 0.61 | – | – | – | – | – | – |
| Cu | – | – | – | – | – | – | – | – | – | – | – | 0.91 | 2.07 | 2.89 | 19.62 | 19.12 | 20.02 | 4.51 | 4.85 |
| Te | 0.99 | 1.96 | 2.01 | 1.01 | 1.95 | 3.91 | 2.97 | 0.97 | 2.97 | 2.01 | 2.00 | – | 0.13 | – | – | – | – | – | – |
| Au | – | 0.99 | 0.95 | – | 0.97 | – | – | – | – | – | – | – | – | – | 0.20 | 0.19 | 0.20 | – | – |
| Fe | 0.01 | 0.09 | – | – | – | 0.02 | 0.18 | 0.02 | – | – | 0.03 | 0.14 | 0.43 | 0.04 | 1.29 | 1.73 | 1.09 | 1.12 | 1.03 |
| Pb | 0.98 | 2.06 | – | – | – | 0.80 | – | – | 0.04 | – | – | 0.95 | 4.95 | – | 11.50 | 11.29 | 11.28 | – | – |
| Total | 2 | 9 | 3 | 3 | 6 | 7 | 8 | 1 | 5 | 5 | 4 | 6 | 35 | 7 | 78 | 78 | 78 | 10 | 10 |

*1* altaite, *2* buckhornite, *3* calaverite, *4* hessite, *5* petzite, *6* rucklidgeite, *7* stützite, *8* native tellurium, *9* tellurobismuthite, *10* tetradymite, *11* volynskite, *12* aikinite, *13* felbertalite, *14* wittichenite, *15–17* Phase B, *18–19* bornite. Abbreviation: *apfu* = atoms per formula unit.

TABLE 4.3. Electron microprobe data of sylvanite intergrown with $AgTe_3$ or stützite

| | S | Ag | Cu | Te | Au | Fe | Total |
|---|---|---|---|---|---|---|---|
| 1 | 0.26 | 13.45 | 0.44 | 61.98 | 23.00 | 1.52 | 100.65 |
| 2 | <0.07 | 13.06 | 0.26 | 62.95 | 23.16 | 0.87 | 100.30 |
| 3 | 0.09 | 13.46 | 0.30 | 63.14 | 23.39 | 0.59 | 100.97 |
| 4 | 0.48 | 12.60 | 0.45 | 60.97 | 23.42 | 1.78 | 99.70 |
| 5 | 0.24 | 12.58 | 0.49 | 62.56 | 23.22 | 1.37 | 100.46 |
| 6 | 0.17 | 12.77 | 0.44 | 62.20 | 22.89 | 1.61 | 100.08 |
| 7 | 0.16 | 13.05 | 0.40 | 62.21 | 23.18 | 1.39 | 100.39 |
| 8 | 0.07 | 13.75 | 0.43 | 62.59 | 21.78 | 1.33 | 99.95 |
| 9 | 0.72 | 13.50 | 0.70 | 60.57 | 22.56 | 2.14 | 100.19 |
| 10 | 0.39 | 14.76 | 0.36 | 60.72 | 22.83 | 1.87 | 100.93 |
| 11 | 0.12 | 13.03 | 0.34 | 60.32 | 22.94 | 1.25 | 98.00 |

Pb and Bi are below the detection limit of 0.31 wt.% Pb and 0.39 wt.% Bi, respectively.

FIG. 4.2. Reflected-light photomicrographs (oil immersion) of Phase A and associated minerals. **A**. Phase A-bearing composite inclusion consisting of Phase A, bornite, and digenite (?). Note Phase A shows distinct golden reflection color. **B**. Phase A-bearing composite inclusion consisting of Phase A, chalcopyrite, sylvanite, and stützite. **C**. Phase A-bearing composite inclusions consisting mainly of Phase A, sylvanite, and chalcopyrite. Sample 1050-1c/1050 m. **D**. Phase A-bearing composite inclusions and bornite-bearing composite inclusions in pyrite. Sample 1050-1a/1050 m. **E**. Phase A-bearing composite inclusions and native tellurium-bearing composite inclusions in pyrite. Sample 1050-1a/1050 m. **F**. Trail of Phase A-bearing composite inclusions cut by fracture filled by gold. Note gold is yellower and brighter than Phase A. Sample 1050-1e/1050 m. **G**. Trail of Phase A-bearing inclusions in pyrite. The largest composite inclusion in the right consists of Phase A, sylvanite, altaite, and other small, unidentified phases. Sample 1050-1c/1050 m. Abbreviations: Alt = altaite, Au = gold, Bn = bornite, Cp = chalcopyrite, Dg = digenite, Clv = calaverite, Gn = galena, Ptz = petzite, Py = pyrite, Stz = stützite, Syl = sylvanite, Te = native tellurium.

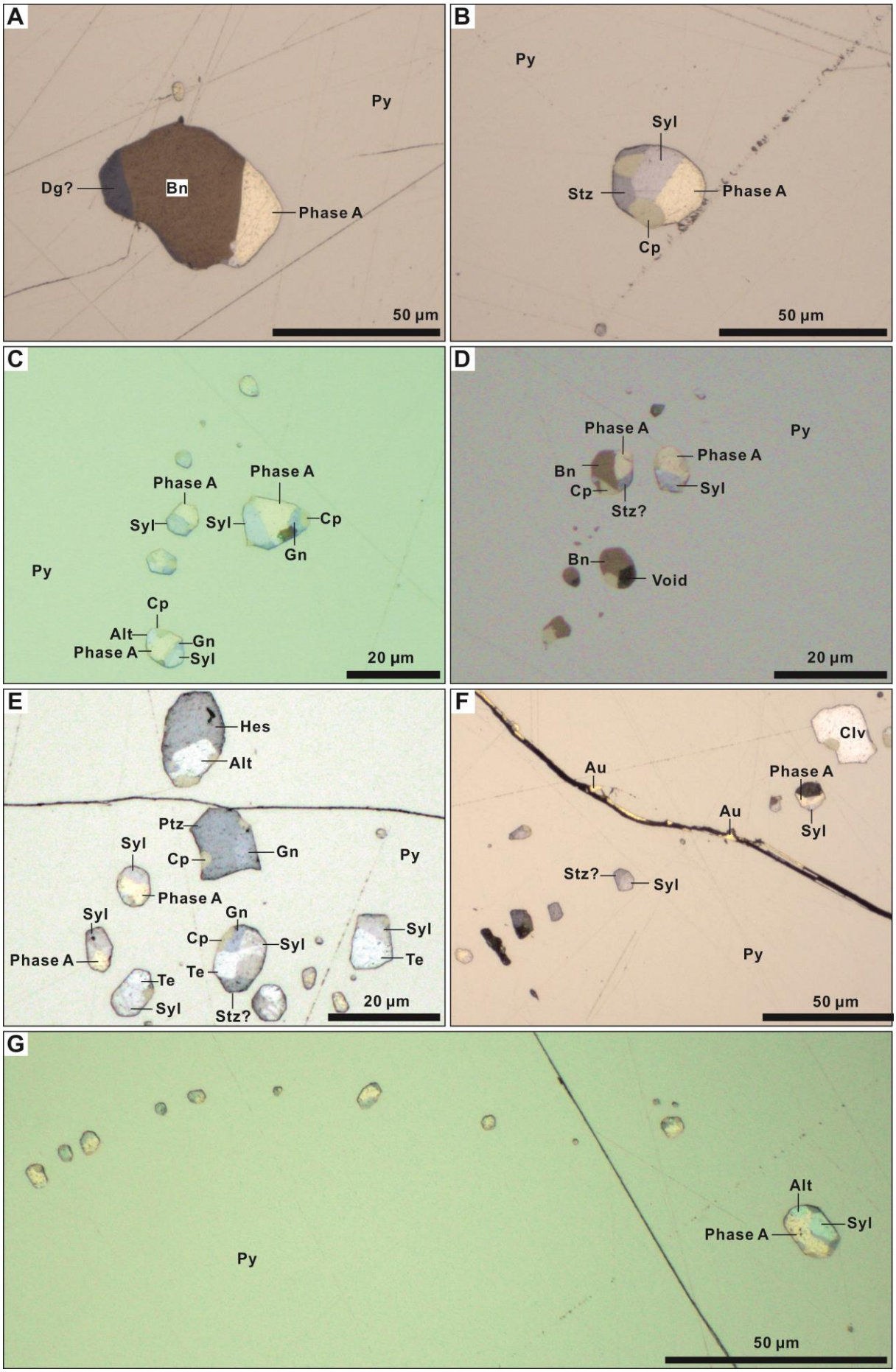
A
Py
Dg?
Bn
Phase A
50 µm
B
Py
Syl
Stz
Phase A
Cp
50 µm
C
Phase A
Phase A
Syl
Syl
Cp
Gn
Py
Cp
Alt
Gn
Phase A
Syl
20 µm
D
Phase A
Py
Phase A
Bn
Cp
Syl
Stz?
Bn
Void
20 µm
E
Hes
Alt
Ptz
Syl
Cp
Gn
Py
Phase A
Syl
Gn
Cp
Syl
Syl
Phase A
Te
Te
Te
Syl
Stz?
20 µm
F
Clv
Au
Phase A
Au
Syl
Stz?
Syl
Py
50 µm
G
Alt
Syl
Phase A
Py
50 µm

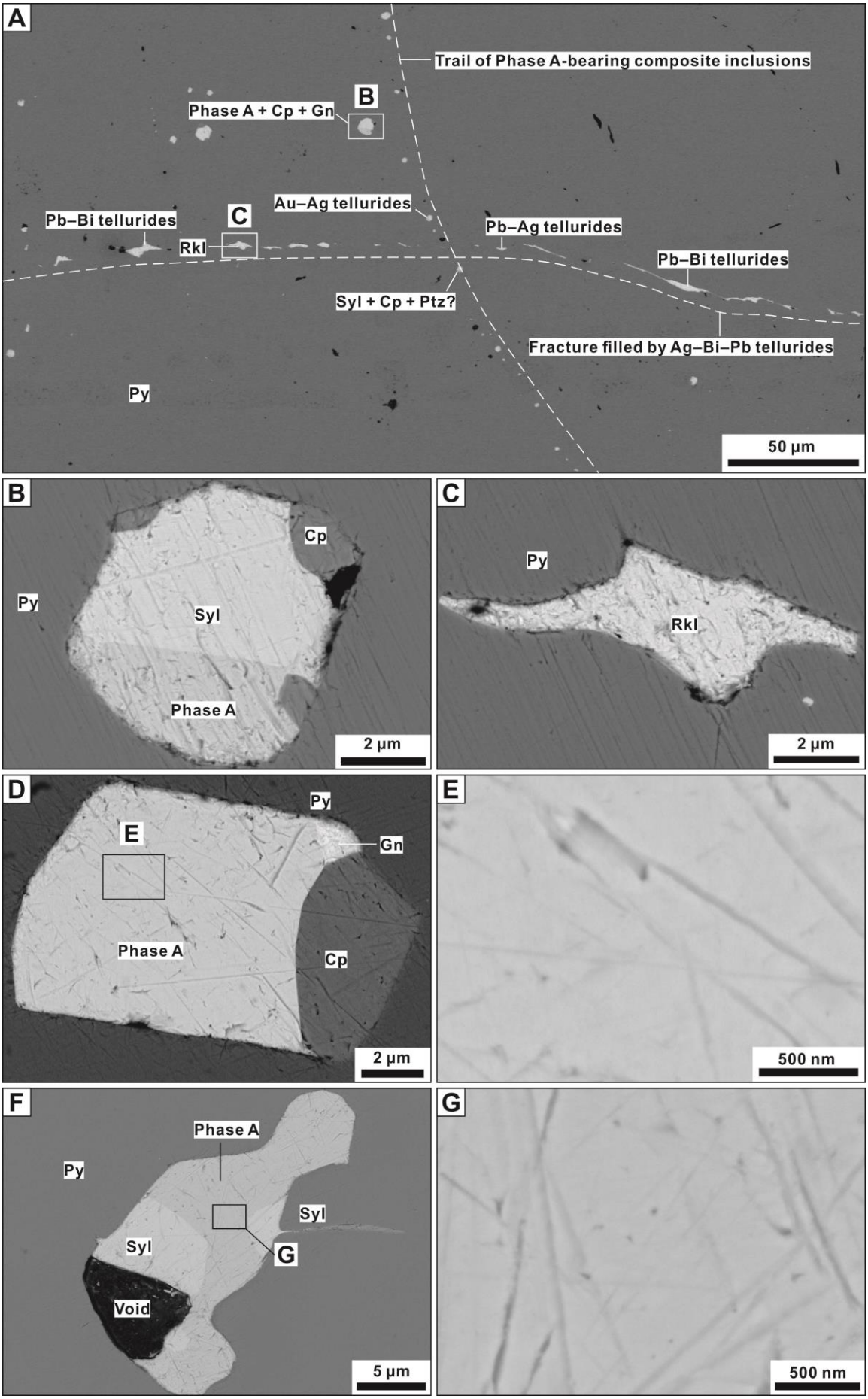
A
Trail of Phase A-bearing composite inclusions
Phase A + Cp + Gn
B
Au–Ag tellurides
Pb–Bi tellurides
C
Rkl
Pb–Ag tellurides
Pb–Bi tellurides
Syl + Cp + Ptz?
Fracture filled by Ag–Bi–Pb tellurides
Py
50 μm
B
Cp
Py
Syl
Phase A
2 μm
C
Py
Rkl
2 μm
D
Py
E
Gn
Phase A
Cp
2 μm
E
500 nm
F
Phase A
Py
Syl
Syl
G
Void
5 μm
G
500 nm

FIG. 4.3. Scanning electron microscope images of Phase A and associated minerals. **A**. Trail of Phase A-bearing composite inclusions cut by fracture filled by Ag–Bi–Pb tellurides. Sample 1050-1c/1050 m. **B**. Close-up view of the Phase A-bearing composite inclusion indicated in A. This composite inclusion consists of Phase A, sylvanite, and chalcopyrite. Sample 1050-1c/1050 m. **C**. Close-up view of the rucklidgeite aggregate indicated in A. Sample 1050-1c/1050 m. **D**. Composite inclusion consisting of Phase A, galena, and chalcopyrite. Sample 1050-1a/1050 m. **E**. Close-up view of a part of the Phase A grain indicated in D. Note Phase A is compositionally homogeneous. Sample 1050-1a/1050 m. **F**. Composite inclusion consisting of Phase A and sylvanite. Sample 1050-1a/1050 m. **G**. Close-up view of a part of the Phase A grain indicated in F. Note Phase A is compositionally homogeneous. Sample 1050-1a/1050 m. Abbreviations: Cp = chalcopyrite, Gn = galena, Rkl = rucklidgeite, Ptz = petzite, Py = pyrite, Syl = sylvanite.

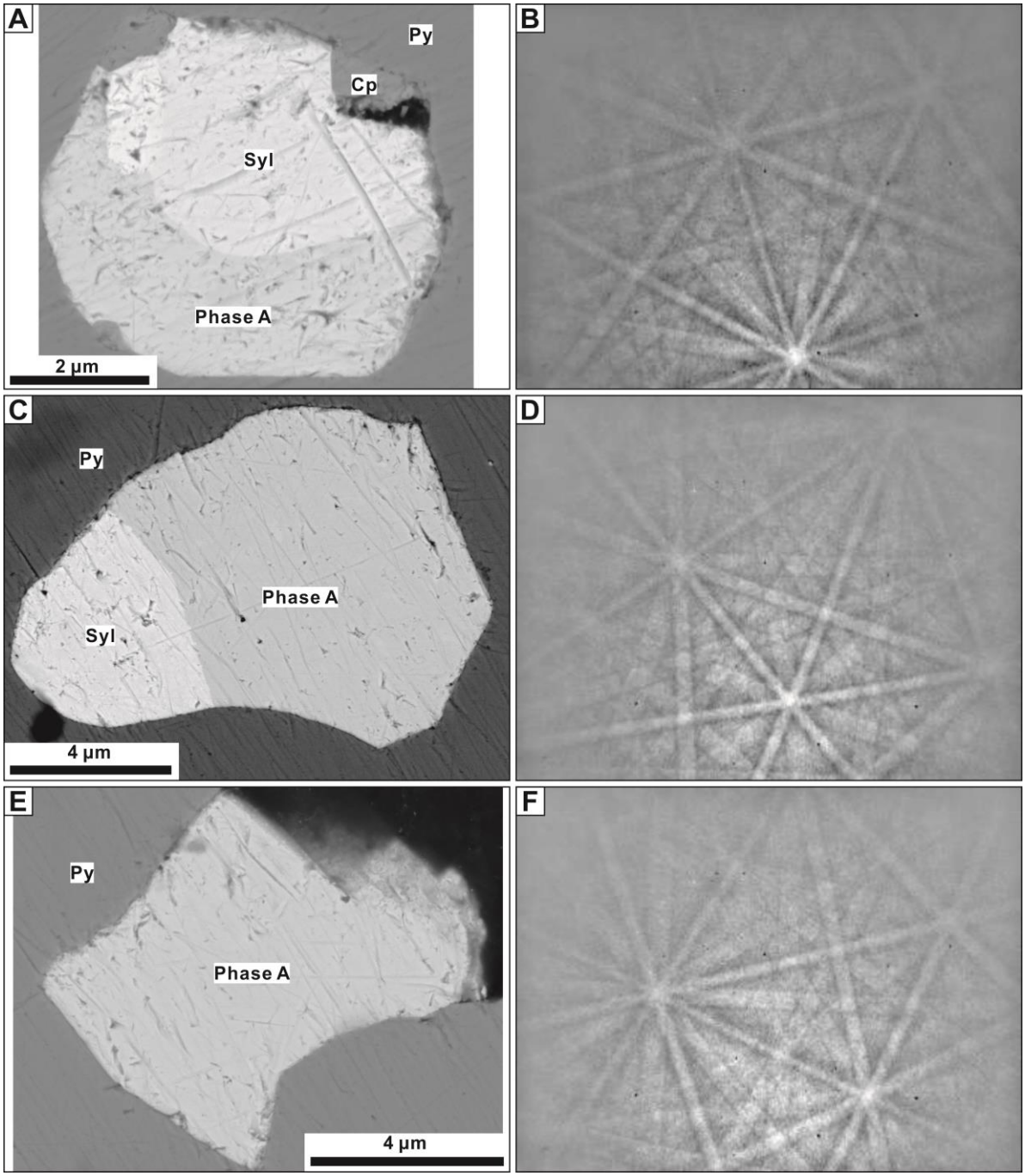


FIG. 4.4. Scanning electron microscope (SEM) images (left column, A, C, E) of Phase A grains and their corresponding electron backscatter diffraction (EBSD) images (right column, B, D, E).

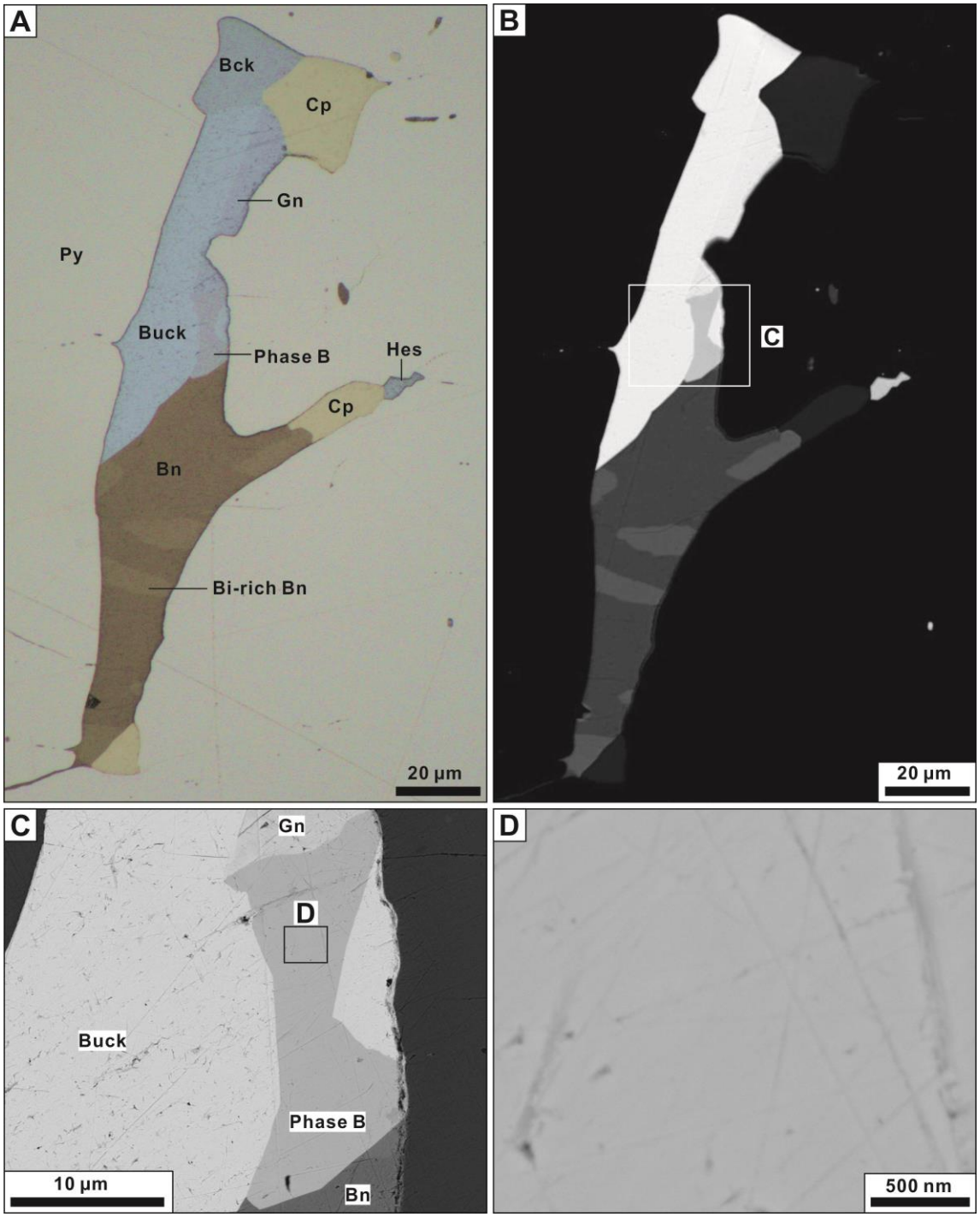


FIG. 4.5. Reflected-light photomicrograph (A, oil immersion), BSE image (B), and SEM images (C, D) of Phase B and associated ore minerals. (**A, B**) Aggregate of Phase B, chalcopyrite, bornite, buckhornite, galena, and hessite within pyrite. Brighter patches in bornite contain *ca.* 8 wt.% Bi (*cf.* column 18 in Table 4.2); other areas in bornite have ca. 2 wt.% Bi (*cf.* column 19 in Table 4.2). **C**. Close-up view of the rectangular area indicated in B. **D**. Close-up view of a part of the Phase B grain indicated in C. Note Phase B is compositionally homogeneous. Sample 1050-1a/1050 m. Abbreviations: Buck = buckhornite, Bn = bornite, Cp = chalcopyrite, Gn = galena, Hes = hessite, Py = pyrite.

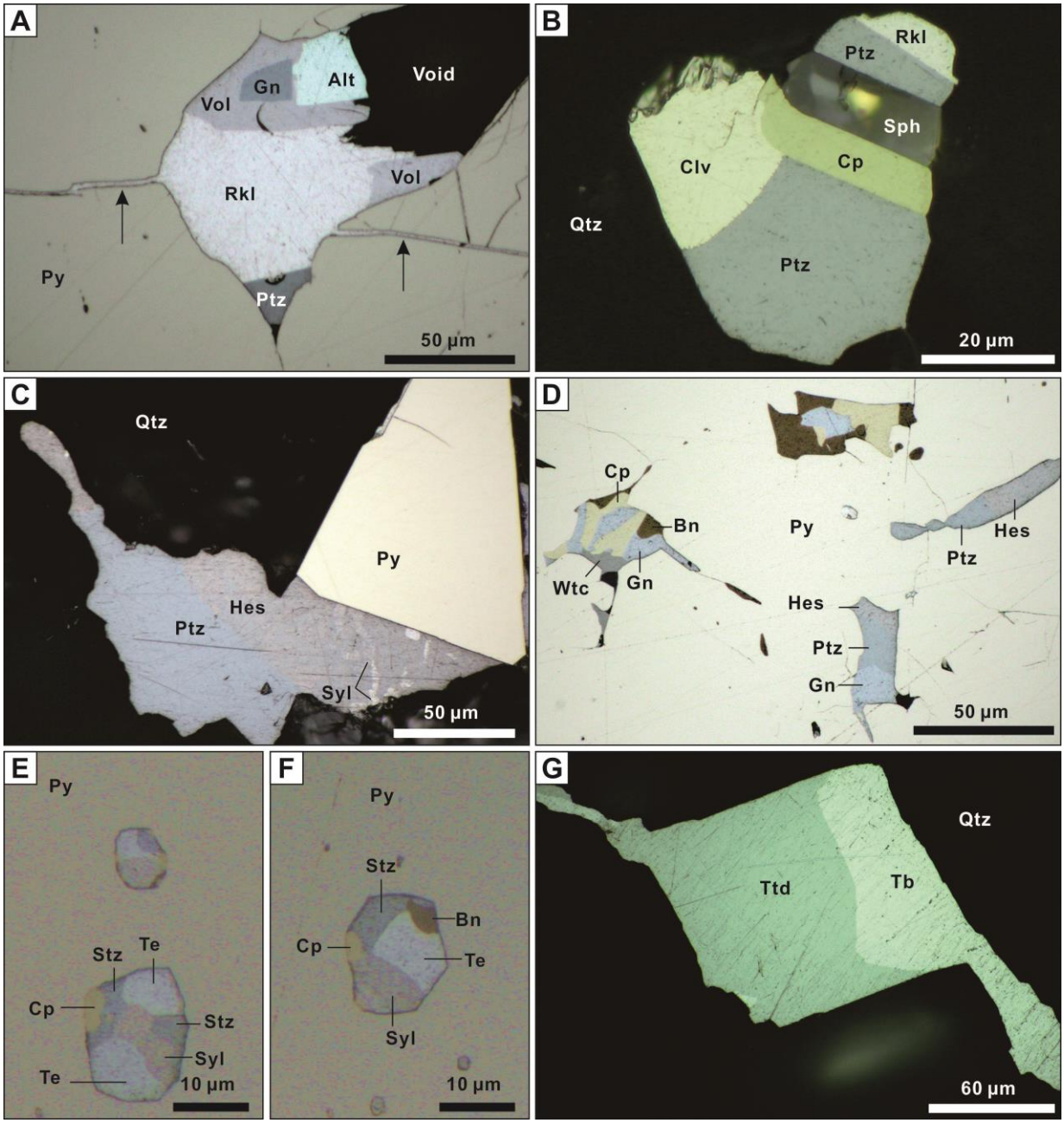


FIG. 4.6. Reflected-light photomicrographs (oil immersion) of tellurides and associated minerals. **A**. Aggregate of altaite, volynskite, petzite, galena, and rucklidgeite in pyrite. Micro-fractures are filled by rucklidgeite (arrowed). Sample 1050-1a/1050 m. **B**. Intergrowth aggregate of calaverite, petzite, chalcopyrite, sphalerite, and rucklidgeite in quartz. Sample 1050-1b/1050 m. **C**. Aggregate of hessite, petzite, and sylvanite on pyrite. Sylvanite occurs as minute graphic blebs in hessite. Sample DY-892-4b/892 m. **D**. Telluride and sulfide-bearing aggregates in pyrite. Sample 1050-1a/1050 m. **E**. Aggregate of native tellurium, sylvanite, stützite, and chalcopyrite in pyrite. Note triple junctions between native tellurium, sylvanite, and stützite. Sample 1050-1a/1050 m. **F**. Intergrowth aggregate of

native tellurium, sylvanite, stützite, chalcopyrite, and bornite, with triple-junction contacts. Sample 1050-1c/1050 m. **G**. Aggregate of tellurobismuthite and tetradymite. Sample DY-892-4c/892 m. Abbreviations: Bn = bornite, Clv = calaverite, Cp = chalcopyrite, Gn = galena, Hes = hessite, Ptz = petzite, Py = pyrite, Rkl = rucklidgeite, Sph = sphalerite, Stz = Stützite, Syl = sylvanite, Tb = tellurobismuthite, Ttd = tetradymite, Vol = volynskite, Wtc = wittichenite.

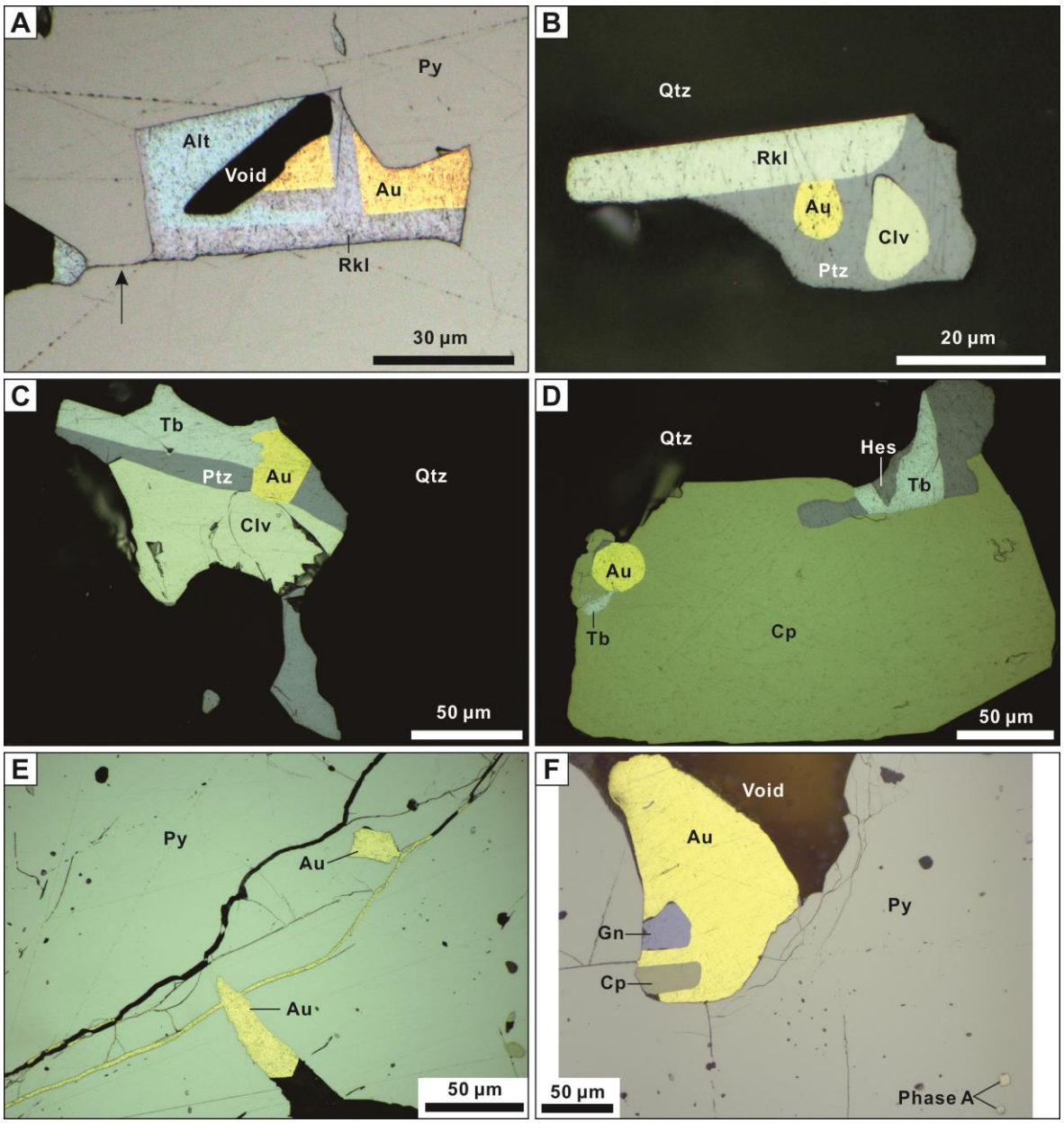


FIG. 4.7. Reflected-light photomicrographs (oil immersion) of gold and associated minerals. **A**. Aggregate of gold, altaite, and rucklidgeite in pyrite. Note the bottom left margin of the aggregate is delimitated by a micro-fracture (arrowed). Sample DY-892-4b/892 m. **B**. Aggregate of gold, calaverite, petzite, and rucklidgeite in quartz. Gold and calaverite occur as rounded grains in petzite. Sample 1050-1b/1050 m. **C**. Aggregate of gold, calaverite, petzite, and tellurobismuthite in quartz. Sample 1050-1b/1050 m. **D**. Rounded gold grain enclosed by chalcopyrite. Sample 1050-1b/1050 m. **E**. Gold aggregate in pyrite fracture. Sample 1050-1c/1050 m. **F**. Gold in contact with galena and chalcopyrite. Note two small phase A grains (bottom right) have reflection color similar to gold but are slightly darker than gold. Abbreviations: Au = gold, Clv = calaverite, Cp = chalcopyrite, Gn = galena, Hes = hessite, Ptz = petzite, Py = pyrite, Rkl = rucklidgeite, Tb = tellurobismuthite.

## 4.5 Discussion

### *4.5.1 Phase A*

There are three minerals in the Ag–Te binary system: hessite ($Ag_2Te$), stützite ($Ag_{5-x}Te_3$), and empressite (AgTe). In addition, γ phase ($Ag_{1.9}Te$) (Kiukkola and Wagner, 1957; Cabri, 1965) and $AgTe_3$ (Range et al., 1982) have been reported as synthetic phases. $AgTe_3$, with a distinctly golden color, has been synthesized by Range et al. (1982), and its stability field has been studied by Range and Thomas (1983), but the natural occurrence of $AgTe_3$ has not been reported so far.

The chemical composition and optical properties of Phase A observed at the Yangzhaiyu Au deposit all resemble synthetic $AgTe_3$. Phase A, with the empirical formula of $AgTe_3$, has very consistent chemical composition (Table 4.1) and much higher tellurium content than other Ag tellurides. Phase A shows no heterogeneity in high-magnification SEM images (Figs. 4.3, 4.4), excluding the possibility that Phase A is an intimate intergrowth of native tellurium and other Ag tellurides. The characteristic golden reflection color of Phase A (Fig. 4.2) further distinguishes it from other Ag tellurides and native tellurium. Synthetic $AgTe_3$ has a rhombohedral, pseudocubic structure, which can be viewed as a slightly deformed ordered (1:3; Ag:Te) variant of the α-polonium structure, with Te forming a 3D-framework with $TeTe_4$ squares and $AgTe_6$ octahedra sharing vertices to form two non-intersecting 3D-frameworks (Range et al., 1982). These features are optically expressed as the isotropic character of Phase A observed at the Yangzhaiyu Au deposit. However, the EBSD patterns of Phase A do not match the structure of the synthetic $AgTe_3$.

Range et al. (1982) point out that synthetic $AgTe_3$ is only stable above 0.4 GPa, below which it decomposes to a mixture of $Ag_{5-x}Te_3$ and Te. The decomposition of synthetic $AgTe_3$ only takes a few minutes at 1 bar and 300 ℃. It is unrealistic that the vein system of the Yangzhaiyu Au deposit was emplaced above 0.4 GPa (i.e., >15 km). First, thick quartz veins as wide as 7 meters are characteristic of a brittle environment. Therefore, we expect that quartz veins at the Yangzhaiyu deposit are typical of veins developing within the seismogenic regime (i.e., less than 10–15 km; Sibson, 1986). Second, the silver content in sylvanite intergrown with more

Ag-rich tellurides can be used to constrain the formation temperature (Cabri, 1965). At the Yangzhaiyu Au deposit, sylvanite grains intergrown with stützite ($Ag_{5-x}Te_3$) or Phase A ($AgTe_3$) contain 12.6 to 14.8 wt.% Ag (Table 4.3), with an average value of 13.3, suggesting a formation temperature of *ca.* 220 ℃ according to the phase diagram of Cabri (1965). Assuming a geothermal gradient of 25 ℃ per km of depth, a formation depth of 15 km would suggest a temperature of 375 ℃ for the ambient rocks; this temperature is much higher than the calculated depositional temperature of sylvanite, and by analogy Phase A. Therefore, Phase A observed at the Yangzhaiyu Au deposit might be a low-pressure polymorph of the synthetic $AgTe_3$. However, additional data such as crystallographic data and physical property data are required before Phase A can be submitted as a new mineral species, but the small size of Phase A makes it difficult to obtain these data.

*4.5.2 Telluride paragenesis*

The telluride-bearing mineral assemblages, as observed in our sample collection, suggest a generally decreasing $f_{Te2}$ trend during telluride deposition, and bismuth is scarce in fluids during the early stage of telluride deposition. This is because native tellurium and Phase A ($AgTe_3$)-bearing assemblages are paragenetically older than other telluride-bearing assemblages, and Bi-tellurides and Bi-sulfosalts never occur in assemblages with native tellurium and Phase A.

Native tellurium and Phase A-bearing assemblages always occur as composite inclusions along well-sealed fractures in pyrite (Figs. 4.2, 4.3, 4.4, 4.6E, F), contrasting with other telluride-bearing assemblages, which occur as larger patches connecting with fractures or as fracture-fillings in pyrite (Figs. 4.3A, 4.6A, 4.7A). Trails of Phase A-bearing composites are also locally cut by fractures filled by Bi-telluride-bearing assemblages (e.g., rucklidgeite-bearing assemblage, Fig. 4.3A) and gold (Fig. 4.2F). The microstructures suggest that the Phase A and native tellurium-bearing assemblages formed early and at higher temperatures, at which pyrite was more soluble in aqueous fluids (the solubility of pyrite peaks at ca. 300 ℃, and decreases with decreasing temperature; Reed and Palandri, 2006) and thus a higher recrystallization rate (i.e., dissolution and re-precipitation rate), enabling pyrite to completely seal pre-existing fractures. At lower temperatures, however, the lower

recrystallization rate of pyrite keeps micro-fractures unsealed or visible, sometimes filled by tellurides.

*4.5.3 Conditions of telluride deposition*

The estimated $f_{Te2}$–$f_{S2}$ conditions of telluride mineralization for the temperature of 200 ℃ are indicated in Fig. 4.8, with log $f_{Te2}$ between -15 and -9 and log $f_{S2}$ between -17 and -11. The upper $f_{Te2}$ and $f_{S2}$ limits of the telluride deposition are constrained by the stützite–native tellurium equilibrium and the chalcopyrite–bornite equilibrium, respectively, based on the presence of sylvanite-tellurium-stützite-chalcopyrite-bornite intergrowth aggregates (Fig. 4.6F). The lower $f_{Te2}$ and $f_{S2}$ limits must be higher than the $Bi_2Te_3$–Bi and the $FeS_2$–FeS equilibrium, respectively, based on the absence of native bismuth and pyrrhotite. Further, the absence of $FeTe_2$ and $Bi_2S_3$ constrains the $f_{Te2}$-$f_{S2}$ conditions between the $FeTe_2$–FeS equilibrium line and the $Bi_2Te_3$–$Bi_2S_3$ equilibrium line.

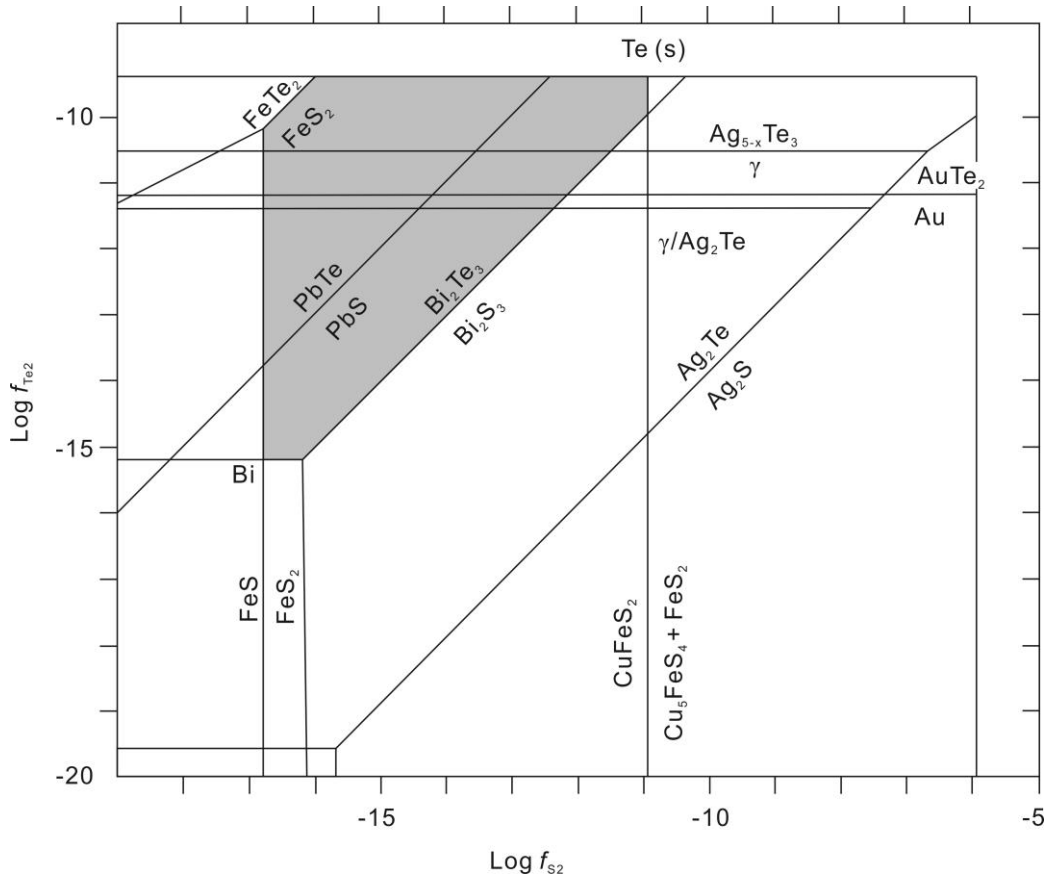


FIG. 4.8. Fugacity diagram of S vs. Te, with selected sulfide–telluride equilibria at 200 ℃ (modified from Afifi et al., 1988). Shaded area indicates $f_{Te2}$–$f_{S2}$ conditions of the telluride–gold deposition stage.

# Chapter 5

# Metallogenic Model for the Xiaoqinling Region

## 5.1 Dahu Au-Mo deposit

The quartz-vein style Dahu Au-Mo deposit is hosted by the Neoarchean amphibolite-facies metamorphic rocks of the Taihua Group. The hydrothermal system has an Re-Os isochron age of 206.4 ± 3.9 Ma. The mineralized quartz veins mainly consist of quartz, K-feldspar, pyrite, chalcopyrite, galena, and molybdenite, and accessory gold, tellurides, Bi-sulfosalts, covellite, $Cu_{1.65}S$, bornite, anhydrite, celestine, rutile, etc. The system is characterized by carbono-aqueous fluids of low to moderate salinity and high oxygen fugacity. The stable isotope data of stage I quartz are characterized by uniform $\delta^{18}O$ values of quartz, and low and scattered δD values of fluid inclusion waters. The mineralization of the Dahu deposit was coeval with the large-scale post-collisional magmatism in the Qinling–Dabie Orogen during the Late Triassic. Based on the metal signature, mineral association, fluid characteristics, and tectono-magmatic setting of the Dahu deposit, it can be ruled out that the ore-forming fluids have significant contributions from meteoric waters, or fluids derived from devolatilization of basement rocks or a subducting oceanic slab (see discussion in Chapter 3). We propose that the ore-forming fluids of the Dahu deposit were derived from an unexposed and oxidized magmatic system (Fig. 5.1).

Anomalous enrichment of Mo, Bi, and Te is a feature of magmatic-hydrothermal systems related to felsic magmatism (e.g., Afifi et al., 1988; White et al., 1981; Thompson and Newberry, 2000; Mao et al., 2008, 2011), and Mo deposits are associated with oxidized magmatic systems rather than reduced magmatic systems (Ishihara, 1981; Lehmann, 1990). The oxidized fluid environment (Fig. 5.2) of the Dahu deposit is indicated by the vein mineral association, such as the widespread presence of anhydrite and celestine in stage I, the abundance of pink K-feldspar (owing to the presence of $Fe^{3+}$ or hematite; Deer et al., 2001), the abundance of pyrite and scarcity of pyrrhotite, the presence of Au(Ag)-tellurides instead of native bismuth and maldonite ($Au_2Bi$), and the presence of green biotite (owing to the abundance of Mg and $Fe^{3+}$; Ishihara, 1998). In addition, reduced gases such as $CH_4$ and $N_2$

were not detected in fluid inclusions by Raman spectroscopic analysis (Fig. 3.12). Hypogene bornite and covellite commonly occur in magmatic-hydrothermal systems, such as porphyry and epithermal deposits (e.g., Einaudi et al., 2003; Cook et al., 2011), but are rarely reported in orogenic gold deposits, most of which are considered to be related to metamorphic fluids (e.g., McCuaig and Kerrich 1998; Goldfarb et al., 2005). This is probably because covellite and bornite precipitate at high fluid sulfidation states, which are typical of magmatic-hydrothermal fluids (Einaudi et al., 2003). Niobium-rich rutile is also a typical magmatic-hydrothermal mineral (e.g., Černý et al., 1999).

A magmatic-hydrothermal origin is in accordance with the regional tectono-magmatic setting. The Late Triassic is a major magmatic period in the Qinling–Dabie Orogen, with abundant granitic rocks and mafic dikes emplaced in a post-collisional extensional setting and related to partial melting of the lower crust and an ancient enriched lithospheric mantle beneath the southern margin of the North China Craton and the North Qinling Belt. Emplacement of the Laoniushan granitic complex (228 ± 1 to 215 ± 4 Ma: Ding et al., 2011) and the Wengyu granite (205 ± 2 Ma: Hu et al., 2012) within the Huashan complex (i.e., not the Early Cretaceous Wenyu granite) during the Late Triassic suggests that the post-collisional magmatism also occurred in the Xiaoqinling region. Hronsky et al. (2012) propose that the critical fundamental control on gold metallogeny in accretionary orogens is the presence of a gold-enriched upper mantle, which becomes a source of mineralization via melt or hydrothermal fluid components. This model may apply to the Dahu deposit, because elevated Au contents (10.4–13.5 ppb) in peridotite xenoliths from the Hebi locality (Zheng et al., 2005) suggesting significant gold enrichment in subduction-refertilised upper mantle peridotite beneath the North China Craton, and Sr and Nd isotope data of the ore sulfides from the Dahu deposit plot near enriched mantle composition (Ni et al., 2012).

Therefore, we propose the parent magma of the Dahu Au-Mo deposit stems from partial melting of enriched lithosphere mantle, which had been metasomatised by subduction related fluids and/or low-degree partial melts from convecting mantle wedge during the Late Paleozoic to the Early Triassic and thus is enriched in incompatible components (e.g., $H_2O$, $SO_2$, Au). The lack of magmatism activity in the southern margin of the North China Craton during the Late Paleozoic to the Early Triassic (e.g., Wang et al., 2013) suggests that incompatible

components retained in the metasomatised upper mantle rather than being carried to the surface by mantle-derived melts. During the Late Triassic, subsequent melting of the enriched lithospheric mantle could produce magmas with high $H_2O$ and $SO_2$ contents, thus high oxygen fugacity (Ishihara, 1981; Takagi and Tsukimura, 1997). The exceptionally thick Precambrian continental crust (>50 km: Zhao et al., 2012) in the Xiaoqinling region is more favorable as a fractionation column than thinner crust, because it extends the residence time of magmas (Carten et al., 1993). On crystallization of oxidized melt system, Mo and Au partition preferentially into the silicate liquid (Candela, 1992; Jugo et al., 1999), thus producing Mo and Au rich residual melts with subsequent removal of Mo and Au into the aqueous fluid phase. S and Te will also be hold in the oxidized melt system as long as there is no sulfide saturation. On fluid saturation, these components will also quantitatively partition into the aqueous fluid phase (e.g., Keppler and Wyllie 1991; Keppler 1999; Frank et al., 2002; Audétat and Pettke 2003). The oxidation state of aqueous fluids in equilibrium with silicate magmas is controlled by $fO_2$ of the magmas (Cameron and Hattori, 1987), efficient exsolution of $CO_2$-rich aqueous fluids is feasible from magmas in relatively deep environments (e.g., >10 km or 3 kbar; Ridley and Diamond, 2000; Lowenstern, 2001), and highly saline fluids are not predicted as the end-product of granitic magma crystallization at pressures greater than about 1.3 kbars (Ridley and Diamond, 2000). Finally, crustal fracture systems associated with lithospheric extension served as ideal sites for fluid flow and metal accumulation in thermal gradients.

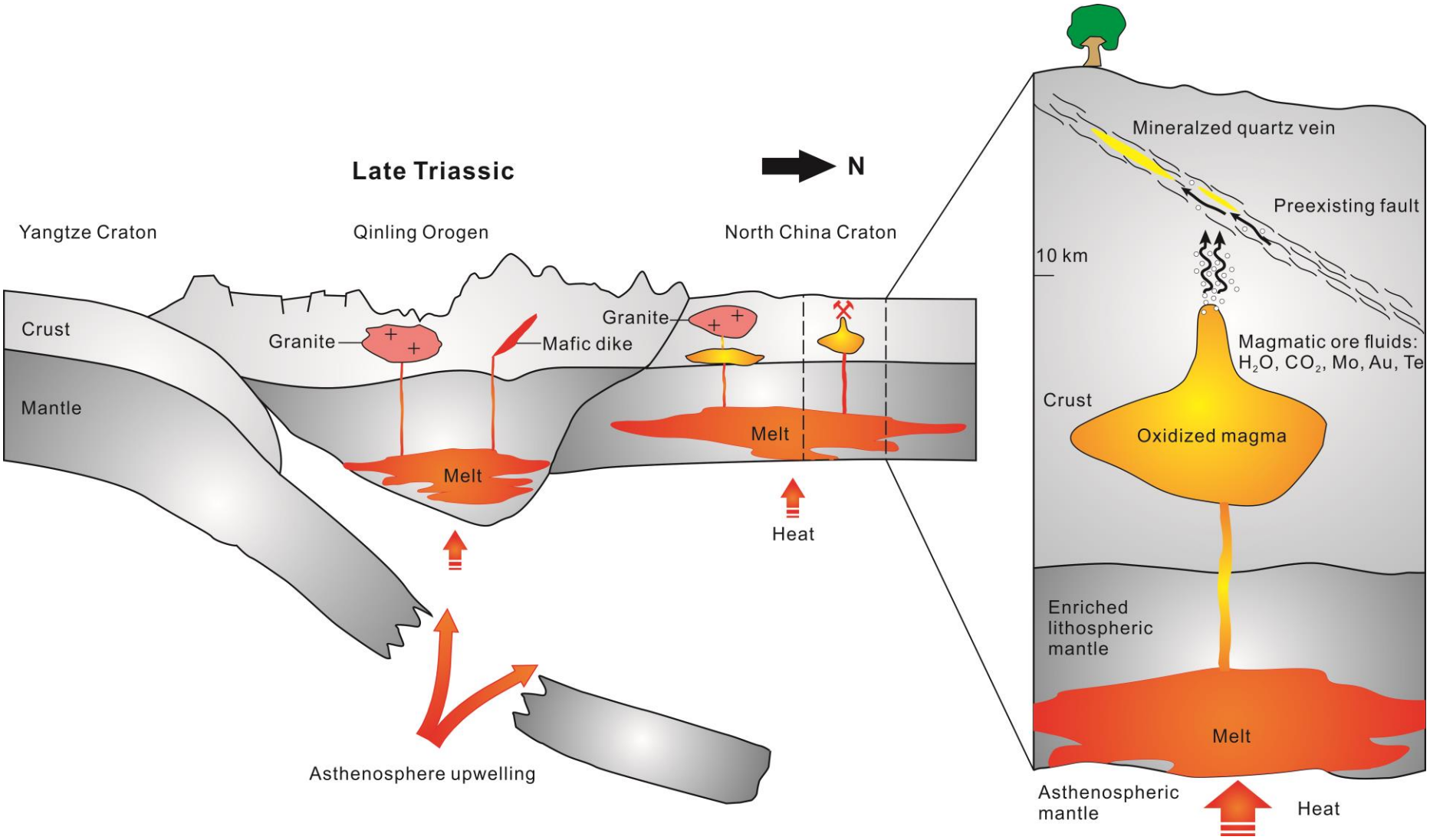


FIG. 5.1. Schematic diagram showing tectonic setting and genetic model of the Dahu Au-Mo deposit.

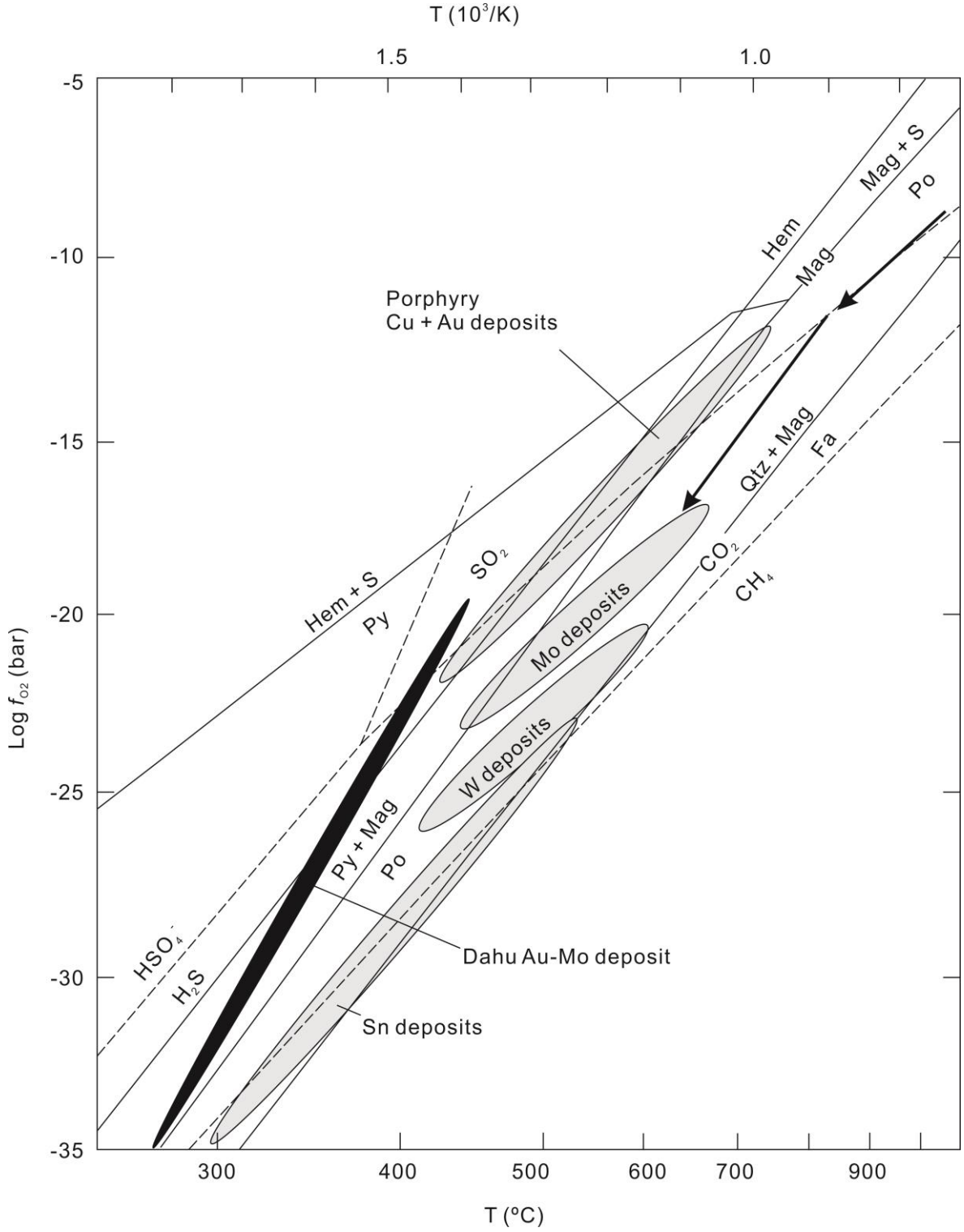


FIG. 5.2. Temperature and oxygen fugacity conditions of the Dahu Au-Mo deposit (black area) compared to some magmatic-hydrothermal ore deposits (modified from Ohmoto and Goldhaber, 1997; Takagi and Tsukimura, 1997). The solid lines are common mineral buffers. The dashed lines are for $SO_2/H_2S$ = 1, $H_2S/HSO_4^-$ = 1, $SO_2/HSO_4^-$ = 1, and $CO_2/CH_4$ = 1 at $P_{\text{total fluid}}$ = 1 kbar. Arrows show general redox paths of an oxidized granitic magma

## 5.2 Yangzhaiyu Au deposit

The Yangzhaiyu Au deposit is located about 10 km southwest of the Dahu deposit (Figs. 1.2, 4.1) and hosted in the Neoarchean amphibolite-facies metamorphic rocks of the Taihua Group. The ore-mineral assemblage consists of pyrite, chalcopyrite, galena, bornite, sphalerite, gold, and native tellurium together with a wide variety of tellurides and Bi-sulfosalts. Four $^{40}Ar/^{39}Ar$ plateau ages of ore-related biotite and sericite range from 134.5 ± 0.7 to 123.7 ± 0.5 Ma (Li et al., 2012b), suggesting an Early Cretaceous age. The mineralization of the Yangzhaiyu deposit was coeval with the large-scale magmatism related to lithospheric thinning of eastern China during the Early Cretaceous. The Neoarchean Taihua Group rocks can be excluded as a fluid source, because most volatiles of these rocks likely have been released during the regional medium-grade metamorphism in the Paleoproterozoic, and the refractory Neoarchean Taihua rocks have a low content of volatiles (0.75–2.6 wt% LOI; Luan et al. 1985), and are also very low in gold (<1.7 ppb, Li et al. 1996, Feng et al. 2009) and tellurium (the Neoarchean Taihua Group lacks Te-rich sources such as limestone, black shale, oceanic Fe-Mn crusts, and sulfide-rich rocks). Although formed about 80 Ma after the Dahu Au-Mo deposit, the metal signature (e.g., anomalous enrichment of Bi and Te) and ore-mineral assemblage (e.g., bornite, tellurides, Bi-sulfosalts) of the Yangzhaiyu deposit also suggests a magmatic-hydrothermal origin. Similar to the Dahu deposit, the parent magma most likely results from partial melting of the upper mantle, as Li et al. (2012a) suggest a magmatic and mantle source for the ore-forming fluids of the Yangzhaiyu Au deposit based on fluid inclusion characteristics, stable and noble gas isotope compositions, and geochronological data.

## 5.3 Conclusions

There are two major episodes of Au-Mo mineralization in the Xiaoqinling region: the Late Triassic and the Early Cretaceous. The mineralization of the Dahu and the Yangzhaiyu deposits, and by analogy the Late Triassic and the Early Cretaceous Au-Mo mineralization events in the Xiaoqinling region, are both related to and coeval with large-scale magmatism. The Late Triassic Au-Mo mineralization and magmatism is related to the final collision between the North China Craton and the Yangtze Craton, and the subsequent post-collisional extensional

process, while the Early Cretaceous Au-Mo mineralization and magmatism is related to tectonic reactivation and lithospheric thinning of eastern China induced by underthrusting of the Paleo-Pacific plate beneath the eastern China continent. The critical fundamental control on Au-Mo metallogeny in the Xiaoqinling region is likely the presence of a metasomatised upper mantle, which is produced by early subduction-related processes before the final collision between the North China Craton and the Yangtze Craton and becomes a long-term source of mineralization-associated magma and hydrothermal fluid components.

# References


Albrecht M., Derrey I., Horn I., Schuth S., and Weyer S., 2014, Quantification of trace element contents in frozen fluid inclusions by UV-fs-LA-ICP-MS analysis: Journal of Analytical Atomic Spectrometry, v. 29, p. 1034–1041.

Ames L., Tilton G.R. and Zhou G.Z., 1993, Timing of collision of the Sino-Korean and Yangtse cratons: U–Pb zircon dating of coesite-bearing ecologites: Geology, v. 21, p. 339–342.

Afifi, A.M., Kelly, W.C., and Essene, E.J., 1988, Phase relations among tellurides, sulfides, and oxides: II Applications to telluride-bearing ore deposits: Economic Geology, v. 83, p. 395–404.

Audétat, A.,and Pettke, T., 2003,The magmatic-hydrothermal evolution of two barren granites: A melt and fluid inclusion study of the Rito del Medio and Can˜ada Pinabete plutons in northern New Mexico (USA): Geochimica et Cosmochimica Acta, v. 67, p. 97–121.

Audétat, A., Pettke, T., Heinrich, C.A., and Bodnar, R.J., 2008, The composition of magmatic–hydrothermal fluids in barren versus mineralized intrusions: Economic. Geology, v. 103, p. 877–908.

Barton P.B., 1973, Solid solutions in the system Cu-Fe-S. Part I: The Cu-S and CuFe-S joins: Economic Geology, v. 68, p. 455–465.

Bi, S.J., Li, J.W., Zhou, M.F., and Li, Z.K., 2011a, Gold distribution in As-deficient pyrite and telluride mineralogy of the Yangzhaiyu gold deposit, Xiaoqinling district, southern North China craton: Mineralium Deposita, v. 46, p. 925–941.

Bi, S.J., Li, J.W., and Li, Z.K., 2011b, Geological significance and geochronology of Paleproterozoic mafic dykes of Xiaoqinling gold district, southern margin of the North China Craton: Earth Science—Journal of China University of Geosciences, v. 36, p. 17–32 (in Chinese with English abstract).

Bodnar, RJ., Binns, P.R., and Hall, D.L., 1989, Synthetic fluid inclusions. VI. Quantitative evaluation of the de crepitation behaviour of fluid inclusions in quartz at one atmosphere confining pressure: Journal of Metamorphic Geology, v. 7, p. 229–242.

Bodnar, R.J., 1993, Revised equation and table for determining the freezing point depression of

$H_2O$-NaCl solutions: Geochimica et Cosmochimica Acta, v. 57, p. 683–684.

Bonev, I.K., Petrunov, R., Cook, N. J., and Ciobanu, C. L., 2005, Kostovite and its argentian varieties: Deposits and mineral associations: Bulgarian Academy of Sciences, Geochemistry, Mineralogy and Petrology, v. 42, p. 1–22.

Cabri, L.J., 1965, Phase relations in the Au-Ag-Te systems and their mineralogical significance: Economic Geology, v. 60, p. 1569–1606.

Cai, N.Z, and Su, Z.B., 1985, Stratigraphic subdivision and distinction of primary rock-types of the taihua group in the Xiaoqinling Mountain: Regional Geology of China, v. 13, p. 35–44 (in Chinese with English abstract).

Cao, E.K., Li, Y.Q., and Huang, F.E., 1989, A discovery of Te-Au-bearing quartz veins in the Xiaoqinling goldfield and the mineralogical research: Geology of Shanxi, v. 7, p. 77–87 (in Chinese with English abstract).

Carten, R.B, White, W.H., and Stein H.J., 1993, High-grade granite-related molybdenum systems: Classification and origin: Geological Association of Canada, Special Paper 40, p. 521–554

Cameron, E.M., and Hattori, K., 1987, Archean gold mineralization and oxidized hydrothermal fluids: Economic Geology, v. 82, p. 1177–1191.

Candela, P.A., 1992, Controls on ore metal ratios in granite-related ore systems: an experimental and computational approach: Transactions of the Royal Society of Edinburgh: Earth Sciences, v. 83, p. 317–326.

Černý; P., Chapman, R., Simmons, W.B., and Chackowsky, L.E., 1999, Niobian rutile from the McGuire granitic pegmatite, Park County, Colorado: Solid solution, exsolution, and oxidation: American Mineralogist, v. 84, p. 754–763.

Chang, L.L.Y., and Hoda, S. N., 1977, Phase relations in the system $PbS$-$Cu_2S$-$Bi_2S_3$ and the stability of galenobismutite: American Mineralogist, v. 62, p. 346–350.

Clayton, R.N., and Mayeda, T.K., 1963, The use of bromine pentafluoride in the extraction of oxygen from oxides and silicates for isotopic analysis: Geochimica et Cosmochimica Acta, v. 27, p. 43–52.

Coleman, M.L., Sheppard, T.J., Durham, J.J., Rouse, J.E., and Moore G.R., 1982, Reduction of water with zinc for hydrogen isotope analysis: Analytical Chemistry, v. 54, p. 993–995.

Collins, P.L.F., 1979, Gas hydrates in $CO_2$-bearing fluid inclusions and the use of freezing data for estimation of salinity: Economic Geology, v. 74, p. 1435–1444.

Cook, N.J., Ciobanu, C.L., Stanleyleyley, C.J., Paar, W.H., and Sundblad, K., 2007, Compositional data for Bi–Pb tellurosulfides: Canadian Mineralogist, v. 45, p. 417-435.

Cook, N.J., Ciobanu, C.L., Danyushevsky, L.V., and Gilbert, S., 2011, Minor and trace elements in bornite and associated Cu–(Fe)-sulfides: A LA-ICP-MS study: Geochimica et Cosmochimica Acta, v. 75, p. 6473–6496.

Deer, W.A., Howie, R.A., and Zussman, J., 2001, Rock-Forming Minerals, Volume 4A: Framework Silicates–Feldspars: London, Geological Society of London, 972 p.

Didier, A., Bosse, V., Boulvais, P., Bouloton, J., Paquette, J.L., Montel, J.M., and Devidal, J.L., 2013, Disturbance versus preservation of U–Th–Pb ages in monazite during fluid–rock interaction: textural, chemical and isotopic in situ study in microgranites (Velay Dome, France): Contributions to Mineralogy and Petrology, v. 165, p. 1051–1072.

Ding, L.X., Ma, C.Q., Li, JW., Robinson, P.T., Deng, X.D., Zhang, C., and Xu, W.C., 2011, Timing and genesis of the adakitic and shoshonitic intrusions in the Laoniushan complex, southern margin of the North China Craton: Implications for post-collisional magmatism associated with the Qinling Orogen: Lithos, v. 126, p. 212–232.

Donnay, G., Donnay, J.D.H., and Kullerud, G., 1958, Crystal and twin structure of digenite, $Cu_9S_5$: American Mineralogist, v. 43, p. 228–242

Dong, Y.P., Zhang, G.W., Neubauer, F., Liu, X.M., Genser, J., and Hauzenberger, C., 2011, Tectonic evolution of the Qinling orogen, China: Review and synthesis: Journal of Asian Earth Sciences, v. 41 p. 213–237.

Dowling, K., and Morrison, G., 1989, Application of quartz textures to the classification of gold deposits using North Queensland examples, *in* Keays, R.R., Ramsay, W.R.H., and Groves, D.I., ed., The geology of gold deposits: the perspective in 1988, Economic Geology Monograph 6: USA, The Economic Geology Publishing Company, p. 342–355.

Du, A.D., Wu, S.Q., Sun, D.Z., Wang, S.X., Qu, W.J., Markey, R., Stein, H., Morgan, J., and Malinovskiy D., 2004, Preparation and certification of Re-Os dating reference materials: Molybdenites HLP and JDC: Geostandards and Geoanalytical Research, v. 28, p. 41–52.

Einaudi, M.T., Hedenquist, J., and Inan, E., 2003, Sulfidation state of fluids in active and

extinct hydrothermal systems: Transitions from porphyry to epithermal environments, *in* Simmons, S.F., and Graham, I., eds., Volcanic, Geothermal, and Ore-Forming Fluids: Rulers and Witnesses of Processes within the Earth, Society of Economic Geologists Special Publication 10 Volume: USA, Society of Economic Geologists, p 285–313.

Fleet, M.E., 2006, Phase equilibria at high temperatures, *in* Vaughan, D.J., ed., Sulfide mineralogy and geochemistry, Reviews in Mineralogy and Geochemistry 61 Volume: USA, Mineralogical Society of America, p 365–419.

Fan, H.R., Xie, Y.H., Zhao R., and Wang, Y.L., 2000, Dual origins of Xiaoqinling gold-bearing quartz veins: fluid inclusion evidence: Chinese Science Bulletin, v. 45, p. 1424–1430.

Fan, H.R., Xie, Y.H., Zhai, M.G., and Jin, C.W., 2003, A three stage fluid flow model for Xiaoqinling lode gold metallogenesis in the Henan and Shanxi provinces, central China: Acta Petrologica Sinica, v. 19, p. 260–266 (in Chinese with English abstract).

Fang, W.X., 1996, Study on mineral geochemistry for the auriferous quartz veins in Xiaoqinling: Geology and Exploration, v. 32, p. 40–45 (in Chinese with English abstract).

Feng, J.Z., Wang, X.C., Sun, W.Z., Yan, J.S., Yu, W., Wang, S.Q., Xu, J.C., Tie, J.K., Li, Z.Y., He, Y., Zhang, X.M., Zhang, X.W., Li, C.F., Liu, Z.Y., and Sun, W.J., 2011, Prospecting report of the Dahu gold deposit, Lingbao County, Henan Province: Luoyang, No.1 Geological Team of BGMR of Henan province, 122 p (in Chinese, internal report).

Frank, M.R., Candela, P.A., Piccoli, P.M., Glascock., M.D., 2002, Gold solubility, speciation, and partitioning as a function of HCl in the brine-silicate melt-metallic gold system at 800 ℃ and 100 MPa: Geochimica et Cosmochimica Acta, v. 66, p. 3719–3732.

Gao, Y., Li, Y.F., Guo, B.J., Cheng, G.X., and Liu, Y.W., 2010, Geological characteristics and molybdenite Re-Os isotopic dating of Qianfanling quartz-vein Mo deposit in Songxian county, Western Henan Province: Acta Petrologica Sinica, v. 26, p. 757–767 (in Chinese with English abstract).

Garofalo, P.S., Fricker, M.B., Günther D., Bersani, D., and Lottici, P.P., 2014, Physical-chemical properties and metal budget of Au-transporting hydrothermal fluids in orogenic deposits, *in* Garofalo, P. S., and Ridley, J. R., eds., Gold-Transporting Hydrothermal Fluids in the Earth's Crust: London, the Geological Society of London, p 71–102.

Giletti, B.J., and Yund, R.A., 1984, Oxygen diffusion in quartz: Journal of Geophysical Research, v. 89, p. 4039–4046.

Goldfarb, R.J., Newberry, R.J., Pickthorn, W.J., and Gent, C.A., 1991, Oxygen, hydrogen, and sulfur isotope studies in the Juneau gold belt, southeastern Alaska: constraints on the origin of hydrothermal fluids: Economic Geology, v. 86, p. 66–80.

Goldfarb, R.J., Baker, T., Dube, B., Groves, D.I., Hart, C.J., and Gosselin, P., 2005, Distribution, character and genesis of gold deposits in metamorphic terranes, *in* Hedenquist, J.W., Thompson, J.F.H., Goldfarb, R.J., and Richards, J.P., eds., Economic Geology 100th Anniversary Volume: USA, Society of Economic Geologists, p. 407–450.

Goldfarb, R.J., Hart, C.J.R., Davis, G., and Groves, D.I., 2007, East Asian gold: deciphering the anomaly of Phanerozoic gold in Precambrian cratons: Economic Geology, v. 102 p. 341–346.

Grguric, B.A., Harrison, R., and Putnis, A., 2000, A revised phase diagram for the bornite-digenite join from in situ neutron diffraction and DSC experiments: Mineralogical Magazine, v. 64, p. 213–231.

Groves, D.I., Goldfarb, R.J., Gebre-Mariam, M., Hagemann, S.G., and Robert, F., 1998, Orogenic gold deposits: a proposed classification in the context of their crustal distribution and relationship to other gold deposit types: Ore Geology Reviews, v. 13, p. 7–27.

Guillong, M., Meier, D.L., Allan, M.M., Heinrich, C.A., and Yardley, B.W.D., 2008, SILLS: A Matlab-based program for the reduction of laser ablation ICP-MS data of homogeneous material and inclusions, *in* Sylvester, P., ed., Laser ablation ICP–MS in the earth sciences: current practices and outstanding issues, Mineralogical Association of Canada Short Course 40 volume: Vancouver, Canada, Mineralogical Association of Canada, p. 328–333.

Günther, D., Audétat, A., Frischknecht, R., and Heinrich, C.A., 1998, Quantitative analysis of major, minor and trace elements in fluid inclusions using laser ablation inductively coupled plasma mass spectrometry: Journal of Analytical Atomic Spectrometry, v. 13, p. 263–270.

Guo, B., Zhu, L.M., Li, B., Gong, H.J., and Wang, J.Q., 2009. Zircon U–Pb age and Hf isotope composition of the Huashan and Heyu granite plutons at the southern margin of North

China Craton: implications for geodynamic setting: Acta Petrologica Sinica, v. 25, p. 265–281.

Hacker, B.R., Ratschbacher, L., Webb, L., Ireland, T., Walker, D., and Dong, S.W., 1998, U/Pb zircon ages constrain the architecture of the ultrahigh-pressure Qinling–Dabie Orogen, China: Earth and Planet Science Letters, v. 161, p. 215–230.

Halfpenny, A., Prior, D.J., and Wheeler, J., 2006, Analysis of dynamic recrystallization and nucleation in a quartzite mylonite: Tectonophysics, v. 427, p. 3–14.

Hedenquist, J.W., and Lowenstern, J.B., 1994, The role of magmas in the formation of hydrothermal ore deposits: Nature, v. 370, p. 519–527.

Hodge J.L., 2010, Hydrothermal evolution of two stages of gold mineralization at the orogenic new Celebration gold deposit, and implications for gold mineralization within the Kalgoorlie-Kambalda corridor, eastern Goldfields Province, Western Australia: Unpublished PhD. Thesis, Perth, Australia, The University of Western Australia, 388 p.

Hronsky, JM.A., Groves, D.I., Loucks, R.R., and Begg, G.C., 2012, A unified model for gold mineralisation in accretionary orogens and implications for regional-scale exploration targeting methods: Mineralium Deposita, v. 47, p. 339–358.

Hu, J., Jiang, S.Y., Zhao, H.X., Shao, Y., Zhang, Z.Z., Xiao, E., Wang, Y.F., Dai, B.Z., and Li, H.Y., 2012, Geochemistry and petrogenesis of the Huashan granites and their implications for the Mesozoic tectonic settings in the Xiaoqinling gold mineralization belt, NW China: Journal of Asian Earth Science, v. 56, p. 276–289.

Hu, Z.G., Qian, Z.Z., Yan, G.M., Chen, Z.L., and Li, M.X., 1994, Xiaoqinling detachment-metamorphic core complex and gold deposits: Xi'an, Shaanxi Press of Science and Technology, 238 p (in Chinese).

Ishihara, S., 1981, The granitoid series and mineralization, *in* Skinner, B.J., ed., Economic Geology 75th Anniversary Volume: USA, The Economic Geology Publishing Company, p. 458–484.

Ishihara., 1998, Granitoid series and mineralization in the circum-Pacific Phanerozoic granitic belts: Resource Geology, v. 48, p. 219–224.

Jiang, N., Xu, J., and Song, M., 1999, Fluid inclusion characteristics of mesothermal gold deposits in the Xiaoqinling district, Shaanxi and Henan provinces, People’s Republic of

China: Mineralium Deposita, v. 34, p. 150–162.

Jiang, N., 2000, Hydrothermal fluid evolution associated with gold mineralization at the Wenyu Mine, Xiaoqinling District, China: Resource Geology, v. 50, p. 103–112.

Jiang, S.Y., Dai, B.Z., Jiang, Y.H., Zhao, H.X., and Hou, M.L., 2009, Jiaodong and Xiaoqinling: two orogenic gold provinces in different tectonic settings: Acta Petrologica Sinica, v. 25, p. 2727–2738 (in Chinese with English abstract).

Jugo, P.J., Candela, P.A., and Piccoli, P.M., 1999, Magmatic sulfides and Au:Cu ratios in porphyry deposits: an experimental study of copper and gold partitioning at 850 ℃, 100 MPa in a haplogranitic melt–pyrrhotite–intermediate solid solution–gold metal assemblage, at gas saturation: Lithos, v. 46, p. 573–589.

Kase, K., Kusachi, I., and Kishi, S., 1993, Rucklidgeite solid-solution in the Yanahara deposit, Japan: Canadian Mineralogist, v. 31, p. 99–104.

Keppler, H., and Wyllie P.J., 1991, Partitioning of Cu, Sn, Mo, W, U, and Th between melt and aqueous fluid in the systems haplogranite-$H_2O$−HCl and haplogranite-$H_2O$−HF: Contributions to Mineralogy and Petrology, v. 109 p. 139–150.

Keppler, H., 1999, Experimental evidence for the source of excess sulfur in explosive volcanic eruptions: Science, v. 284, p. 1652–1654.

Kerrich., 1976, Some effects of tectonic recrystallisation on fluid inclusions in vein quartz: Contributions to Mineralogy and Petrology, v. 59, p. 195–202.

Kiukkola, K., and Wagner, C., 1957, Measurements on Galvanic Cells Involving Solid Electrolytes: Journal of the Electrochemical Society, v. 104, p. 379–387.

Klemm, L., Pettke, T., and Heinrich, C.A., 2007, Hydrothermal evolution of the El Teniente deposit, Chile: Porphyry Cu-Mo ore deposition from lowsalinity magmatic fluids: Economic Geology, v. 102, p. 1021–1045.

Klemm, L., Pettke, T., and Heinrich, C.A., 2008, Fluid source and magma evolution of the Questa porphyry Mo deposit, New Mexico, USA: Mineralium Deposita, v. 43, p. 533–552.

Heinrich, C.A., Pettke, T., Halter, W., Aigner-Torres, M., Audétat, A., Günther, D., Hattendorf, B., Bleiner, D., Guillong, M., and Horn, I., 2003, Quantitative multi-element analysis of minerals, fluid and melt inclusions by laser-ablation inductively-coupled-plasma

mass-spectrometry: Geochimica et Cosmochimica Acta, v. 67, p. 3473–3496.

Hu, J., Jiang, S.Y., Zhao, H.X., Shao, Y., Zhang, Z.Z., Xiao, E., Wang, Y.F., Dai, B.Z., and Li, H.Y., 2012, Geochemistry and petrogenesis of the Huashan granites and their implications for the Mesozoic tectonic settings in the Xiaoqinling gold mineralization belt, NW China: Journal of Asian Earth Science, v. 56, p. 276–289.

Hu, Z.G., Qian, Z.Z., Yan, G.M., Chen, Z.L., and Li, M.X., 1994, Xiaoqinling detachment-metamorphic core complex and gold deposits: Xi'an, Shaanxi Press of Science and Technology, 238 p. (in Chinese).

Jensen, E.P., and Barton, M.D., 2000, Gold deposits related to alkaline magmatism, in Hagemann, S.G., and Brown, P.E., eds., Gold in 2000, Reviews in Economic Geology 13 Volume: United States, Society of Economic Geologists, p. 279–314.

Lehmann, B., 1990, Metallogeny of tin: Berlin-Heidelberg-New York, Springer-Verlag, 211 p.

Li, H.M., Ye, H.S., Mao, J.W., Wang, D.H., Chen, Y.C., Qu, W.J., and Du, A.D., 2007a, Re-Os dating of molybdenites from Au (Mo) deposits in Xiaoqinling gold ore district and its geological significance: Mineral Deposits, v. 26, p. 417–424 (in Chinese with English abstract).

Li, H.M., Chen, Y.C., Wang, D.H., Ye, H.S., Wang, Y.B., Zhang, C.Q., and Dai, J.Z., 2007b, SHRIMP U-Pb ages of metamorphic rocks and veins in the Xiaoqinling area, and their geological significance: Acta Petrologica Sinica, v. 23, p. 2504–2512 (in Chinese with English abstract).

Li, J.W., Bi, S.J., Sebly, D., Chen, L., Vasconcelos, P., Thiede, D., Zhou, M.F., Zhao, X.F., Li, Z.K., Qiu, H.N., 2012a, Giant Mesozoic gold provinces related to the destruction of the North China craton: Earth and Planetary Science Letters, v. 349–350, p. 26–37.

Li, J.W., Li, Z.K., Zhou, M.F., Chen, L., Bi, S.J., Deng, X.D., Qiu, H.N., Cohen, B., Sebly, D., and Zhao, X.F., 2012b, The Early Cretaceous Yangzhaiyu lode gold deposit, North China Craton: A link between craton reactivation and gold veining: Economic Geology, v. 107, p. 43-79.

Li C, Qu, W.J., Du, A.D., and Zhou, L.M., 2012c, Study on Re-Os isotope in molybdenite containing common Os: Acta Petrologica Sinica, v. 28, p. 702–708 (in Chinese with English abstract).

Li, N., Sun, Y.L., Li, J., Xue, L.W., and Li, W.B., 2008, Molybdenite Re–Os isotope age of the Dahu Au-Mo deposit, Xiaoqinling and the Indosinian mineralization: Acta Petrologica Sinica, v. 24, p. 810–816 (in Chinese with English abstract).

Li, N., Chen, Y.J., Fletcher, I.R., and Zeng, Q.T., 2011, Triassic mineralization with Cretaceous overprint in the Dahu Au-Mo deposit, Xiaoqinling gold province: constraints from SHRIMP monazite U-Th-Pb geochronology: Gondwana Research, v. 20, p. 543–552.

Li, S.M., Qu, L.Q., Su, Z.B., Huang, J.J., Wang, X.S., and Yue, Z.S., 1996, The geology and metallogenic prediction of the gold deposit in Xiaoqinling: Beijing, Geological Publishing House, 250 p (in Chinese with English abstract).

Li, X.H., Wang, C.H., Xuan, S.H., Wang, Q.C., and Hu, J.M., 2006, Geological map of the Xiaoqinling goldfield, unpublished map: Henan, China, Chinese People's Armed Police Force (in Chinese).

Li, X.Z., Yan, C, and Lu, X.X., 1993, Granitoids of MT. Qinling–Dabieshan: Beijing, Geological Publishing House, 218 p (in Chinese).

Lipovetskiy, A.G., Borodayeyev, Y.S., and Zav'yalolov, Y.N., 1978: New lead–bismuth tellurides of the Alekeseyev ore show: International Geology Review, v. 19, p. 1230-1234.

Liu, Q.F., 2013, Exploration breakthrough in the Xiaoqinling gold field: Resource Guide, p. 32.

Lowenstern, J.B., 2001, Carbon dioxide in magmas and implications for hydrothermal systems: Mineralium Deposita, v. 36, p. 490–502.

Lu, X.X., Wei, X.D., Xiao, Q.H., Zhang, Z.Q., Li, H.M, and Wang, W., 1999, Geochronological studies of rapakivi granites in Qinling and its geological implications: Geological Journal of China Universities, v. 15, p. 372–7 (in Chinese with English abstract).

Lu, X.X., Wei, X.D., and Dong, Y., 2004, Characteristics of gold deposits in the Xiaoqingling and Xiong'ershan districts and contributions of mantle-derived fluids: Beijing, Geological Publishing House, 128 p (in Chinese).

Luan, S.W., Cao, D.C., Fang, Y.K., and Wang, J.Y., 1985, Geochemistry of Xiaoqinling gold deposits: Minerals and Rocks, v. 5, p. 1–118 (in Chinese with English abstract).

Luan, S.W., Chen, S.D., Cao, D.C., and Fang, Y.K., 1991, Characteristics of the deep-seated gold mineralization and its evaluational criteria in Xiaoqinling area: Chengdu, Press of

Chengdu University of Science and Technology, 180 p (in Chinese).

Ludwig, K.R., 2012, User's manual for Isoplot 3.75–A geochronology toolkit for Microsoft Excel: California, Berkeley Geochronology Center Special Publication No. 5, 75 p.

Luo, Z.K., Guan, K., and Wang M.Z., 1992, Studies of Au-Ag-Te-Bi minerals of the Xiaoqinling gold mine: Geology and Prospecting, v. 28, p. 31–35 (in Chinese with English abstract).

Maitland, T., and Sitzman, S, 2007, Electron backscatter diffraction (EBSD) technique and materials characterization examples, *in* Zhou, W., and Wang, Z.L., eds., Scanning microscopy for nanotechnology: Germany, Springer, p 41–75.

Mao, J.W., Goldfarb, R.J., Zhang, Z.W., Xu, W.Y., Qiu, Y.M., and Deng, J., 2002, Gold deposits in the Xiaoqinling–Xiong'ershan region, Qinling Mountains, central China: Mineralium Deposita, v. 37, p. 306–325.

Mao, J.W., Xie, G.Q., Zhang, Z.H., Li, X.F., Wang, Y.T., Zhang, C.Q., and Li, Y.F., 2005, Mesozoic large scale metallogenic pulses in North China and corresponding geodynamic settings: Acta Geologica Sinica, v. 21, p. 169–188 (in Chinese with English abstract).

Mao, J.W., Xie, G.Q., Bierlein, F., Qu, W.J., Du, A.D., Ye, H.S., Pirajno, F., Li, H.M., Guo, B.J., Li, Y.F., and Yang, Z.Q., 2008, Tectonic implications from Re–Os dating of Mesozoic molybdenum deposits in the East Qinling–Dabie orogenic belt: Geochimica et Cosmochimica Acta, v. 72, p. 4607–4626.

Mao, J.W., Xie, G.Q., Pirajno, F., Ye, H.S., Wang, Y.B., Li, Y.F., Xiang, J.F., and Zhao, H.J., 2010, Late Jurassic–Early Cretaceous granitoid magmatism in Eastern Qinling, central–eastern China: SHRIMP zircon U–Pb ages and tectonic implications: Australian Journal of Earth Sciences, v. 57, p. 51–78.

Mao, J.W., Pirajno, F., Xiang, J.F., Gao, J.J., Ye, H.S., Li, Y.F., and Guo, B.J., 2011, Mesozoic molybdenum deposits in the East Qinling–Dabie orogenic belt: characteristics and tectonic settings: Ore Geology Reviews, v. 43, p. 264–293.

Mao, J.W., Zhou, Z.H., Feng, C.Y., Wang, Y.T., Zhang, C.Q., Peng, H.J., and Yu, M., 2012, A preliminary study of the Triassic large-scale mineralization in China and its geodynamic setting: Geology in China, v. 39, p. 1437–1471 (in Chinese with English abstract).

Markey, R., Stein, H., and Morgan, J., 1998, Highly precise Re-Os dating for molybdenite

using alkaline fusion and NTIMS: Talanta, v. 45, p. 935–946.

Marsala, A.,Wagner, T., and Wälle, M., 2013, Late-metamorphic veins record deep ingression of metamorphic water: a LA-ICPMS fluid inclusion study from the fold-and-thrust belt of the Rhenish Massif, Germany: Chemical Geology, v. 351, p. 134–153.

Matsuhisa, Y., Goldschmit, J.R., and Clayton, R.N., 1979, Oxygen isotope fractionation in the system quartz-albite-anorthite-water: Geochimica et Cosmochimica Acta, v. 43, p. 1131−1140.

McCuaig, T.C., and Kerrich, R., 1998, P-T-t-deformation-fluid characteristics of lode gold deposits: evidence from alteration systematics: Ore Geology Reviews, v. 12, p. 381–453.

Miron, G.D.,Wagner, T.,Walle, M., and Heinrich, C.A., 2013, Major and trace-element composition and pressure–temperature evolution of rock-buffered fluids in low-grade accretionary-wedge metasediments, Central Alps: Contributions to Mineralogy and Petrology, v. 165, p. 981–1008.

Ni, Z.Y., Wang, R.M., Tong, Y., Yang, C., and Dai, T.M., 2003, $^{207}Pb/^{206}Pb$ Age of zircon and $^{40}Ar/^{39}Ar$ of amphibole from plagioclase amphibolite in the Taihua Group, Luoning, Henan, China: Geological Review, v. 49, p. 361–366 (in Chinese with English abstract).

Ni, Z.Y., Li, N., Guan, S.J., Zhang, H., and Xue, L.W., 2008, Characteristics of fluid inclusions and ore genesis of the Dahu Au-Mo deposit in the Xiaoqinling glod field, Henan province: Acta Petrologica Sinica, v. 24, p. 2058–2068 (in Chinese with English abstract).

Ni, Z.Y., Chen, Y.J., Li, N., and Zhang, H., 2012, Pb-Sr-Nd isotope constraints on the fluid source of the Dahu Au-Mo deposit in Qinling Orogen, central China, and implication for Triassic tectonic setting: Ore Geology Reviews, v. 46, p. 60-67.

Nie, F.J., Jiang, S.H., and Zhao, Y.M., 2001, Lead and sulfur isotope study of the Wenyu and Dongchuang quartz vein-type gold deposits in the Xiaoqinling area, Henan and Shaanxi Province, central China: Mineral Deposits, v. 20, p. 163−173 (in Chinese with English abstract).

Ohmoto, H., and Goldhaber, M.B., 1997, Sulfur and carbon isotopes, *in* Barnes, H.L., ed., Geochemistry of hydrothermal ore deposits, 3rd ed.: New York, Wiley, p. 517–611.

Pettke, T., Oberli, F., Audétat, A., Guillong, M., Simon, C., Hanley, J.J., and Klemm, L.M., 2012, Recent developments in element concentration and isotope ratio analysis of

individual fluid inclusions by laser ablation single and multiple collector ICP-MS: Ore Geology Reviews, v. 44, p. 10–38.

Phillips, G.N., and Powell, R., 2009, Formation of gold deposits: review and evaluation of the continuum model: Earth Science Reviews, v. 94, p. 1–21.

Pickthorn, W.J., Goldfarb, R.J., and Leach, D., 1987, Comment on 'Dual origins of lode gold deposits in the Canadian Cordillera': Geology, v. 15, p. 471–472.

Plotinskaya, O.Y., Kovalenker, V.A., Seltmann, R., and Stanley, C.J., 2006, Te and Se mineralogy of the high-sulfidation Kochbulak and Kairagach epithermal gold telluride deposits (Kurama Ridge, Middle Tien Shan, Uzbekistan): Mineralogy and Petrology, v. 87, p. 187–207.

Poitrasson, F., Chenery, S., and Shepherd, T.J., 2000, Electron microprobe and LA-ICP-MS study of monazite hydrothermal alteration: implications for U–Th–Pb geochronology and nuclear ceramics: Geochimica et Cosmochimica Acta, v. 64, p. 3283–3297.

Prior, D.J., Mariani, E., and Wheeler, J., 2009, EBSD in the earth sciences: applications, common practice, and challenges, *in* Schwartz, A.J., Kumar, M., Adams, B.L., and Field, D., eds., Electron backscatter diffraction in materials science: Germany, Springer, p 345–360.

Qi, J.P., Lai, Y., Ren, K.X., and Tang, G.J., 2006, Sr-isotope constraint on the origin of the Xiaoqinling gold field: Acta Petrologica Sinica, v. 22, p. 2543–2550 (in Chinese with English abstract).

Qin, J.F., Lai, S.C., Diwu, C.R., Ju, Y.J., and Li, Y.F., 2010, Magma mixing origin for the post-collisional adakitic monzogranite of the Triassic Yangba pluton, Northwestern margin of the South China block: geochemistry, Sr–Nd isotopic, zircon U–Pb dating and Hf isotopic evidences: Contributions to Mineralogy and Petrology, v. 159, p. 389–409.

Range, K.J., Zabel, M., Rau, F., Krziwanek, F.V., Marx, R., and Panzer, B., 1982, A novel three-dimensional tellurium array: high-pressure synthesis and crystal structure of $AgTe_3$: Angewandte Chemie, v. 21, p. 706–707.

Range, K.J., and Thomas M., 1983, Pressure-temperature relations in the silver-tellurium system at 75 at-% tellurium: Materials Research Bulletin, v. 18, p. 1195–1202.

Ratschbacher L., Hacker B.R., Calvert A., Webb L.E., Grimmer J.C., McWilliams M.O.,

Ireland T., Dong S.W., and Hu J.M., 2003, Tectonics of the Qinling (Central China): tectonostratigraphy, geochronology, and deformation history: Tectonophysics, v. 366, p. 1–53.

Rauchenstein-Martinek, K., Wagner, T., Wälle, M., and Heinrich, C.A., 2014, Gold concentrations in metamorphic fluids: A LA-ICPMS study of fluid inclusions from the Alpine orogenic belt: Chemical Geology, v. 385, p. 70–83.

Ridley, J.R., and Diamond, L.W., 2000, Fluid chemistry of orogenic lode gold deposits and implications for genetic models, *in* Hagemann, S.G., and Brown, P.E., ed., Gold in 2000, Reviews in Economic Geology, Volume 13: USA, Society of Economic Geologists, p. 141–162.

Ridley, J., 2008? Differentiating Crustal Fluids in the Eastern Tintina Gold Province of Alaska and Yukon: Implications for the Genesis and Distribution of Gold Ores (technical report).

Ridley, J., and Gibson, J., 2011, Ore fluid chemistry of intrusion-related gold deposits (IRGDs) and orogenic gold deposits in the Tintina Gold Province (Alaska): What is the difference? Let's Talk Ore Deposits, 11th SGA Biennial Meeting, Antofagasta, Chile, 2011, Abstracts, p. 592–594.

Roedder, E., 1984, Fluid inclusions, Reviews in Mineralogy and Geochemistry, Volume 12: USA, Mineralogical Society of America, 644 p.

Rucklidge, J.C., and Stumpfl, E.F., 1968, Changes in the composition of petzite ($Au_3AgTe_2$) during analysis by electron microprobe: Neues Jahrbuch für Mineralogie Monatshefte, p. 61–68.

Rudnick, R.L., and Gao, S., 2003, Composition of the continental crust, in Rudnick, R.L., ed., The Crust, Treatise on Geochemistry Volume 3, Oxford, Elsevier-Pergamon, p. 1–64.

Rusk, B.G., Reed, M.H., Dilles, J.H., Klemm, L.M., and Heinrich, C.A., 2004, Compositions of magmatic hydrothermal fluids determined by LA-ICP-MS of fluid inclusions from the porphyry copper-molybdenum deposit at Butte, MT: Chemical Geology, v. 210, p. 173 – 199.

Seydoux-Guillaume, A.M., Montel, J.M., Bingen, B., Bosse, V., de Parseval, P., Paquette, J.L., Janots, E., and Wirth, R., 2012, Low-temperature alteration of monazite: Fluid mediated coupled dissolution–precipitation, irradiation damage, and disturbance of the U–Pb and

Th–Pb chronometers: Chemical Geology, v. 330–331, p. 140–158.

Shen, F.N., 1986, Discussion on the relational questions of Taihua Group in minor Qinling range: Journal of Northwest University, v. 16, p. 43–51 (in Chinese with English abstract).

Shirey, S.B., and Walker, R.J., 1995, Carius tube digestion for low-blank rhenium-osmium analysis: Analytical Chemistry, v. 67, p. 2136–2141.

Sibson, R.H., 1986, Brecciation processes in fault zones: Inferences from earthquake rupturing: Pure and Applied Geophysics, v. 124, p. 159–175.

Sibson R.H., Scott J., 1998, Stress/fault controls on the containment and release of overpressured fluids: examples from gold–quartz vein systems in Juneau, Alaska; Victoria, Australia; and Otago, New Zealand: Ore Geology Reviews, v. 13, p. 293–306.

Simmons, S.F., and Brown, K.L., 2006, Gold in magmatic hydrothermal solutions and the rapid formation of a giant ore deposit: Science, v. 314, p. 288–291.

Smoliar, M.I., Walker, R.J., and Morgan, J.W., 1996, Re-Os ages of group IIA, IIIA, IVA, and IVB iron meteorites: Science, v. 271, p. 1099–1102.

Song, D.K., Zhang, Z.Y., and Liu, J. C., 1980, Exploration report of the eastern portion of the Yangzhaiyu gold deposit: Luoyang, No.1 Geological Team of BGMR of Henan province (in Chinese, internal report).

Stefanova, E., Driesner, T., Zajacz, Z., Heinrich, C.A., Petrov, P., and Vasilev, Z., 2014, Melt and fluid Inclusions in hydrothermal veins: the magmatic to hydrothermal evolution of the Elatsite porphyry Cu-Au deposit, Bulgaria: Economic Geology, v. 109, p. 1359–1381.

Stein, H.J., and Hannah, J.L., 1985, Movement and origin of ore fluids in Climax-type systems: Geology, v. 13, p. 469–474.

Stein, H.J., Markey, R.J., and Morgan, J.W., 1997, Highly precise and accurate Re–Os ages for molybdenite from the East Qinling molybdenum belt, Shaanxi Province, China: Economic Geology, v. 92, p. 827–835.

Sugaki, A., Kitakaze, A., and Harada, H., 1984, Hydrothermal synthesis and phase relations of the polymetallic sulfide system, especially on the Cu–Fe–Bi–S system, *in* Sunagawa, I., ed., Materials science of the earth's interior: Tokyo, Terra Scientific Publication, p 545–583.

Takagi, T., and Tsukimura, K., 1997, Genesis of oxidized- and reduced-type granites:

Economic Geology, v. 92, p. 81–86.

Taylor, S.R., 1964, Abundance of chemical elements in the continental crust: a new table: Geochimica et Cosmochimica Acta, v. 28, p. 1273–1285.

Taylor, H.P., 1974, The application of oxygen and hydrogen isotope studies to problems of hydrothermal alteration and ore deposition: Economic Geology, v. 69, p. 843–883.

Thompson, J.F.H., and Newberry, R.J., 2000, Gold deposits related to reduced granitic intrusions, *in* Hagemann, S.G., and Brown, P.E., ed., Gold in 2000, Reviews in Economic Geology, Volume 13: USA, Society of Economic Geologists, p. 377–400.

Tian, S.Z., Chen, J.Y., and Li, X.M., 1994, The first discovery of buckhornite in China and its study: Acta Mineralogical Sinica, v. 14, p. 241–246 (in Chinese with English abstract).

Ulrich, T., Günther, D., and Heinrich, C.A., 2002, The evolution of a porphyry Cu-Au deposit, based on LA-ICP-MS analysis of fluid inclusions: Bajo de la Alumbrera, Argentina: Economic Geology, v. 97, p. 1889–1920.

Vityk, M.O., and Bodnar, R.J., 1995, Textural evolution of synthetic fluid inclusions in quartz during reequilibration, with applications to tectonic reconstruction: Contributions to Mineralogy and Petrology, v. 121, p. 309–323.

Wang, F., Lu, X.X., Lo, C.H., Wu, F.Y., He, H.Y., Yang, L.K., and Zhu, R.X., 2007b, Post-collisional, potassic monzonite–minette complex (Shahewan) in the Qinling Mountains (central China): $^{40}Ar/^{39}Ar$ thermochronology, petrogenesis, and implications for the dynamic setting of the Qinling orogen: Journal of Asian Earth Sciences, v. 31, p. 153–166.

Wang, G.L., Li, W.L., Li, Q.Z., Li, S.R., and Guo, X.D., 1998, Study of mineral typomorphic characteristics in Dongchuang gold deposit Xiaoqinling, Henan: Gold Geology, v. 4, p. 9–14 (in Chinese with English abstract).

Wang, T.H., Mao, J.W., and Wang, Y.B., 2008, Research on SHRIMP U-P chronology in Xiaoqinling-Xiongerʼshan area: the evidence of delamination of lithosphere in Qinling orogenic belt: Acta Petrologica Sinica, v. 24, p. 1273–1287 (in Chinese with English abstract).

Wang, X.X., Wang, T., Jahn, B.M., Hu, N.G., and Chen, W., 2007a, Tectonic significance of Late Triassic post-collisional lamprophyre dykes from the Qinling Mountains (China):

Geological Magazine, v. 144, p. 837–848.

Wang, X.X., Wang, T., Castro, A., Pedreira, R., Lu, X.X., and Xiao, Q.H., 2011a, Triassic granitoids of the Qinling orogen, central China: Genetic relationship of enclaves and rapakivi-textured rocks: Lithos, v. 126, p. 369–387.

Wang, X.X., Wang, T., Qi, Q.J., and Li, S., 2011b, Temporal-spatial variations, origin and their tectonic significance of the Late Mesozoic granites in the Qinling, Central China: Acta Petrologica Sinica, v. 27, p. 1573–1593 (in Chinese with English abstract).

Wang, X.X., Wang, T., and Zhang, C.L., 2013, Neoproterozoic, Paleozoic, and Mesozoic granitoid magmatism in the Qinling Orogen, China: Constraints on orogenic process: Journal of Asian Earth Sciences, v. 72 p.129–151.

Wang, Y.T., and Mao, J.W., 2002, Mineralization in the post-collisional orogenic extensional regime: A case study of the Xiaoqinling gold deposit clustering area: Geological Bulletin of China, v. 21, p. 562–566 (in Chinese with English abstract).

Wang, Y.T., Mao, J.W., Ye, A.W., Ye, H.S., Li, Y.F., Lu, X.X., and Li, Y.G., 2005, Isotope geochemical characteristics of auriferous quartz veins from medium and great depths of Xiaoqinling area, central China and their significance: Mineral Deposits, v. 24, p.270–279 (in Chinese with English abstract).

Wang, Y.T., Ye, H.S., Ye, A.W., Sun, Y., Li, Y.G., and Zhang, C.Q., 2010, Zircon SHRIM P U-Pb ages and their significances of the Wenyu and Niangniangshan granitic plutons in the Xiaoqinling area, central China: Chinese Journal of Geology, v. 45, p. 167–180 (in Chinese with English abstract).

White, W.H., Bookstrom, A.A., Kamilli, R.J., Ganster, M.W., Smith, R.P., Ranta, D.E., and Steininger, R.C., 1981, Character and origin of Climax-type molybdenum deposits, *in* Skinner, B.J., ed., Economic Geology 75th Anniversary Volume: USA, The Economic Geology Publishing Company, p. 270–316.

Wu Y. B., Zheng Y. F., Zhao Z. F., Cong B., Liu X. M. and Wu F. Y., 2006, U–Pb, Hf and O isotope evidence for two episodes of fluid-assisted zircon growth in marble-hosted eclogites from the Dabie orogen: Geochimica et Cosmochimica Acta, v. 70, p. 3743–3761.

Wu, P., 2012, Issues related to gold exploration breakthrough in the Xiaoqinling gold district, Geology of Shaanxi, v. 30, p. 104–105 (in Chinese).

Wu, X.G., Xu, J.H., Wei, H., Lin, L.H., Zhang, G.R., Hui, D.F., Dong, H.F., 2012, A study of fluid inclusions of Dongtongyu gold deposit in Xiaoqinling area, Mineral Deposits, v. 31, p. 195–206 (in Chinese with English abstract).

Xie, Y.H., Fan, H.R., Wang, Y.L., 1998, $CO_2$-$H_2O$ inclusions and their prospecting significance from granites in Xiaoqinling area, Henan province: Acta Petrologica Sinica, v. 14, p. 542–548 (in Chinese with English abstract).

Xu, Q.D., Zhong, Z.Q., Zhou, H.W., Yang, F.C., and Tang, X.C., 1998, $^{40}Ar/^{39}Ar$ dating of the Xiaoqinling Aarea in Henan Province: Geological Review, v. 44, p. 323−327 (in Chinese with English abstract).

Xu, J.H., Xie, Y.L., Liu, J.M., and Zhu, H.P., 2004., Trace elements in fluid inclusions of Wenyu–Dongchuang gold deposits in the Xiaoqinling area, China: Geology and Prospecting, v. 4, p. 1–6 (in Chinese with English abstract).

Xue, L.W., Chai, S.G., Zhu, J.W., and Li, M.L., 2004, Study on accompanying tellurium resources in Xiaoqinling gold deposit: Conservation and Utilization of Mineral Resources, p. 42–45 (in Chinese with English abstract).

Yang, T., Zhu, L.M., Wang, F., Gong, H.J., and Lu, R.K., 2013, Geochemistry, petrogenesis and tectonic implications of granitic plutons at the Liziyuan orogenic goldfield in the Western Qinling Orogen, central China: Geological Magazine, v. 150, p. 50–71.

Yang, Z.M., Zhang, W.M., Wu, Y.L., Liu, S.L., Wang, Z.G., Xu, G.N., Liu, Z.H., Yang, T.P., Song, Y.L., Ma, Y., Deng, H.L., and Yan, J.S., 1995, Prospecting report of the Dahu gold deposit, Lingbao County, Henan Province: Luoyang, No.1 Geological Team of BGMR of Henan province (in Chinese, internal report).

Yardley, B.W.D.,Banks, D.A.,Bottrell, S.H., and Diamond, L.W., 1993, Post-metamorphic gold–quartz veins from N.W. Italy: the composition and origin of the ore fluid: Mineralogical Magazine, v. 57, p. 407–422.

Ye, H.S., Mao, J.W., Li, Y.F., Guo, B.J., Zhang, C.Q., Liu, J., Yan, Q.R., and Liu, G.Y., 2008, SHRIMP zircon U-Pb and molybdenite Re-Os datings of the superlarge donggou porphyry molybdenum deposit in the East Qinling, China, and its geological implications: Acta Geologica Sinica-English edition, v. 82, p. 134-145.

Zeng, Q.D., McCuaig, T.C., Hart, C.J.R., Jourdan, F., Muhling, J., and Bagas, L., 2012,

Structural and geochronological studies on the Liba goldfield of the West Qinling Orogen, Central China: Mineralium Deposita, v. 47, p. 799–819.

Zhang, B.R., Luo, T.C., Gao, S, et al., 1994, Geochemical study of the lithosphere, tectonism and metallogenesis in the Qinling-Dabashan region: Wuhan, China, Press of China University of Geoscience, 446 p (in Chinese)

Zhang, C.L., Wang, T., and Wang, X.X., 2008, Origin and tectonic setting of the early Mesozoic granitoids in Qinling orogenic belt: Geological Journal of China Universities, v. 14, p. 304–316 (in Chinese with English abstract).

Zhang, G.W., Zhang, B.R., Yuan, X.C., and Xiao, Q.H., 2001, Qinling orogenic belt and continental dynamics: Beijing, Science Press, 855 p (in Chinese).

Zhang, H.F., Goldstein, S.L., Zhou, X.H., Sun, M., and Cai, Y., 2009, Comprehensive refertilization of lithospheric mantle beneath the North China Craton: further Os–Sr–Nd isotopic constraints: Journal of Geological Society, v. 166, p. 249–259.

Zhang, J.J., Zheng, Y.D., and Liu, S.W., 2003, Mesozoic tectonic evolution and ore-deposits formation in the gold mine field of Xiaoqinling: Chinese Journal of Geology, v. 38, p. 74–84 (in Chinese with English abstract).

Zhang, Y.H., Mao, J.W., Jian, W., and Li, Z.Y., 2010, Present status of research on molybdenum deposit in eastern Qinling and the problems remained: Global Geology, v. 29, p. 188-202 (in Chinese with English abstract).

Zhang, Y.H., Mao, J.W., Yu, M.X., and Li, Z.Y., 2012, Mo-bearing quartz vein by acid leaching: evidence from Dahu-Qinnan mine in northern belt of Xiaoqinling gold province, central China: Journal of Jilin University (Earth Science), v. 42, p. 1011–1025 (in Chinese with English abstract).

Zhang, Z.Q., Zhang, G.W., Liu, D.Y., Wang, Z.Q., Tang, S.H., and Wang, J.H., 2006. Isotopic geochronology and geochemistry of ophiolites, granites and detrital sedimentary rocks from the Qinling orogeny: Beijing, Geological Publishing House, 348 p (in Chinese).

Zhao, T.P., Zhai, M.G., Xia, B., Li, H.M., Zhang, Y.Z., and Wan, Y.S., 2004, Zircon U-Pb SHRIMP dating for the volcanic rocks of the Xiong'er Group: Constraints on the initial formation age of the cover of the North China Craton: Chinese Science Bulletin, v. 49, p. 2495–2502 (in Chinese).

Zhao, H.J., Mao, J.W., Ye, H.S., Xie, G.Q., and Yang, Z.X., 2010, Geochronology and geochemistry of the alkaline granite porphyry and diabase dikes in Huanglongpu area of Shanxi Province: Petrogenesis and implications for tectonic environment: Geology of China, v. 37, p. 12−27 (in Chinese with English abstract).

Zhao, H.X., Jiang, S.Y., and Frimmel, H.E., 2011a, A rare Bi-Pb tellurosulfide, $PbBi_4Te_4S_3$, from the Wenyu gold deposit in the Xiaoqinling gold province, China: Canadian Mineralogist, v. 49, p. 1297–1304.

Zhao, H.X., Frimmel, H.E., Jiang, S.H., and Dai, B.Z., 2011b, LA-ICP-MS trace element analysis of pyrite from the Xiaoqinling gold district, China: Implications for ore genesis: Ore Geology Reviews, v. 43, p. 142–153.

Zhao, H.X., Jiang, S.H., Frimmel, H.E., Dai, B.Z., and Ma, L., 2012, Geochemistry, geochronology and Sr–Nd–Hf isotopes of two Mesozoic granitoids in the Xiaoqinling gold district: Implication for large-scale lithospheric thinning in the North China Craton: Chemical Geology, v. 294-295, p. 173–189.

Zheng, J.P., Sun M., Zhou M.F., and Robinson P., 2005, Trace elemental and PGE geochemical constraints of Mesozoic and Cenozoic peridotitic xenoliths on lithosphere evolution of the North China Craton: Geochimica et Cosmochimica Acta, v. 69, p. 3401–3418.

Zhou, H.W., Zhong, Z.Q., Ling, W.L., Zhong, G.L., and Xu, Q.D., 1998, Sm-Nd isochron for the amphibolites within Taihua complex from Xiao Qinling area, Western Henan and its geological implications: Geochimica, v. 27, p. 367–372 (in Chinese with English abstract).

Zhu, H.J., Yang, B.S., Li, Y.H., Qian, D.F. and Li Y.T., 1989, Two rare minerals—rucklidgeite and native tellurium occurring in Xiqoqinling gold field: Acta Mineralogical Sinica, v. 9, p. 37–41 (in Chinese with English abstract).

Zhu, L.M., Zhang, G.W., Chen, Y.j., Ding, Z.J., Guo, B., Wang, F., and Lee, B., 2011, Zircon U-Pb ages and geochemistry of the Wenquan Mo-bearing granitioids in West Qinling, China: Constraints on the geodynamic setting for the newly discovered Wenquan Mo deposit: Ore Geology Reviews, v. 39, p. 46–62.

# Appendix

TABLE A1. Element concentrations (ppm) in quartz-hosted individual fluid inclusions from the Dahu deposit

| Sample Name | FIA | FI No. | Salinity (wt.% ) | Li | B | Na | K | Mn | Fe | Cu | Zn | Rb | Sr | Mo | Ag | Te | Cs | Ba | Au | Pb | Bi |
|---|---|---|---|---|---|---|---|---|---|---|---|---|---|---|---|---|---|---|---|---|---|
| **DH-505-8** | **A1** | L5 | 7.5 | <25 | 266 | 24369 | 9002 | <15 | <176* | <6.0 | <13* | 110 | 23 | <1.8* | <1.3* | <8.7* | 32 | <2.3 | <2.0 | 11 | <0.3 |
| | | L51 | 8.2 | <8.0* | 360 | 25999 | 10578 | <5.0 | <57 | 56 | <4.2 | 84 | 14 | <0.4 | <0.4 | <2.9 | 34 | <0.6 | <0.6 | 3.7 | <0.1 |
| | | L49 | 6.0 | 22 | 234 | 19671 | 6889 | 30 | <76 | <2.6 | <5.4 | 70 | 19 | <0.6 | <0.5* | <3.8 | 22 | <0.9* | <0.8* | <0.2 | <0.1 |
| | | L6 | 5.3 | 17 | 194 | 16735 | 7199 | <3.9 | <44 | <1.3 | <3.2 | 68 | 11 | <0.4 | <0.3 | <2.4 | 17 | <0.5* | <0.5 | 1.1 | <0.1 |
| | Avg. | | 6.8 | 20 | 264 | 21694 | 8417 | 30 | <88 | 56 | <6.5 | 83 | 16 | <0.8 | <0.6 | <4.5 | 26 | <1.1 | <1.0 | 5.1 | <0.2 |
| | SD. | | 1.3 | 3.4 | 71 | 4257 | 1716 | | | | | 20 | 5.3 | | | | 7.9 | | | 5.0 | |
| | **A2** | L13 | 8.0 | 102 | 480 | 27261 | 7361 | <8.0* | <90 | <2.8 | 69 | 56 | 25 | <0.7 | <0.7 | <5.0 | 42 | 4.9 | <1.0 | 3.7 | <0.1 |
| | | L14 | 7.7 | 75 | 369 | 26205 | 6949 | 81 | <100 | <3.2* | 56 | 50 | 49 | <1.0 | <0.8 | <5.4 | 45 | 13 | <1.1 | 24 | <0.1* |
| | Avg. | | 7.9 | 88 | 424 | 26733 | 7155 | 81 | <95 | <3.0 | 63 | 53 | 37 | <0.9 | <0.8 | <5.2 | 43 | 8.8 | <1.1 | 14 | <0.1 |
| | SD. | | 0.2 | 19 | 79 | 747 | 291 | | | | 8.8 | 4.0 | 17 | | | | 2.0 | 5.5 | | 15 | |
| | **A3** | L45 | 9.1 | <23 | 535 | 29785 | 10429 | <14* | <167 | <5.8* | <13* | 88 | 95 | <1.7* | <1.6* | <9.4* | 43 | <2.3 | <1.9 | 19 | <0.3* |
| | | L46 | 8.0 | <14* | 489 | 24951 | 11290 | 158 | <106* | <3.5 | 173 | 58 | 85 | <1.1* | <0.9 | <5.7* | 35 | 44 | <1.2* | <0.3 | <0.2 |
| | | L2 | 8.7 | 235 | 483 | 29048 | 8538 | <6.3 | <70 | <2.4 | <5.1* | 61 | 95 | <0.6* | <0.6 | <3.8 | 60 | <0.9 | <0.8* | 42 | <0.1 |
| | Avg. | | 8.6 | 235 | 502 | 27928 | 10086 | 158 | <114 | <3.9 | 173 | 69 | 91 | <1.1 | <1.0 | <6.3 | 46 | 44 | <1.3 | 31 | <0.2 |
| | SD. | | 0.6 | | 28 | 2604 | 1407 | | | | | 16 | 5.7 | | | | 13 | | | 16 | |
| | **A4** | L11 | 4.3 | 24 | 175 | 14250 | 4267 | <4.2* | <47 | <1.5 | <3.6 | 39 | 8.0 | <0.3 | <0.4 | <2.5 | 11 | <0.6 | <0.5 | 0.7 | <0.1 |
| | | L12 | 6.0 | 38 | 178 | 21049 | 4545 | 18 | <58 | <1.8 | <4.3 | 42 | 6.7 | <0.5 | <0.5 | <3.2 | 12 | <0.7 | <0.7* | <0.1 | <0.1 |
| | Avg. | | 5.1 | 31 | 177 | 17649 | 4406 | 18 | <53 | <1.7 | <4.0 | 41 | 7.3 | <0.4 | <0.5 | <2.9 | 11.5 | <0.7 | <0.6 | 0.7 | <0.1 |
| | SD. | | 1.3 | 10 | 1.8 | 4808 | 197 | | | | | 2.0 | 0.9 | | | | 0.1 | | | | |
| | **A5** | L7 | 6.5 | 32 | 221 | 21382 | 7392 | 7.5 | <44 | 7.4 | <3.1 | 58 | 40 | <0.4 | <0.3 | <2.2 | 21 | <0.6 | <0.5 | 3.1 | <0.1 |
| | | L8 | 5.1 | 24 | 173 | 16519 | 6295 | 8.7 | <41 | <1.4 | <3.1 | 64 | 12 | <0.4 | <0.3* | <2.2 | 14 | 1.1 | <0.5 | 1.1 | <0.1 |
| | | L10 | 5.3 | <8.0 | 157 | 17576 | 5769 | 13 | <55 | <1.8 | <3.8 | 49 | 8.5 | <0.4 | <0.4 | <2.9 | 13 | <0.6 | <0.6 | <0.1 | <0.1 |
| | | L9 | 5.0 | 22 | 159 | 15948 | 6196 | <4.6 | <51 | <1.7 | <3.8 | 66 | 9.4 | <0.4 | <0.4 | <2.8 | 12 | <0.6 | <0.6 | 0.9 | <0.1 |
| | Avg. | | 5.5 | 26 | 177 | 17856 | 6413 | 10 | <48 | 7.4 | <3.5 | 59 | 17 | <0.4 | <0.3 | <2.5 | 15 | 1.1 | <0.6 | 1.7 | <0.1 |
| | SD. | | 0.7 | 5.3 | 30 | 2445 | 691 | 2.7 | | | | 7.4 | 15 | | | | 4.1 | | | 1.2 | |

(Cont.)

| Sample Name | FIA | FI No. | Salinity (wt.% ) | Li | B | Na | K | Mn | Fe | Cu | Zn | Rb | Sr | Mo | Ag | Te | Cs | Ba | Au | Pb | Bi |
|---|---|---|---|---|---|---|---|---|---|---|---|---|---|---|---|---|---|---|---|---|---|
| **DH-505-8** | **A6** | L40 | 5.3 | 19 | 163 | 17473 | 5944 | <6.3 | <71 | <2.5 | <5.2 | 33 | 12 | <0.7 | <0.6 | <3.9 | 9.2 | <1.0* | <0.8 | <0.2 | <0.1 |
| | | L39 | 5.1 | 38 | 164 | 16713 | 5965 | <8.7 | <97 | 4.8 | <7.0 | 63 | 2.7 | <1.0 | <0.9 | <5.1* | 15 | <1.2 | <1.1 | 2.4 | <0.1 |
| | | L41 | 4.4 | 19 | 159 | 14450 | 5131 | <3.8* | <43 | <1.5 | <3.1 | 36 | 8.7 | <0.4 | <0.4 | <2.4 | 10 | <0.5 | <0.5 | <0.1 | <0.1 |
| | | L42 | 4.6 | <10 | 137 | 14349 | 6507 | <6.3* | <70 | <2.4 | <5.1 | 35 | 10 | <0.7 | <0.6 | <3.7 | 8.9 | <0.8 | <0.8 | 0.5 | <0.1 |
| | Avg. | | 4.9 | 25 | 156 | 15746 | 5887 | <6.3 | <70 | 4.8 | <5.1 | 42 | 8.3 | <0.7 | <0.6 | <3.8 | 11 | <0.9 | <0.8 | 1.4 | <0.1 |
| | SD. | | 0.4 | 11 | 13 | 1586 | 567 | | | | | 14 | 4.0 | | | | 3.0 | | | 1.3 | |
| | **A7** | L20 | 5.9 | 16 | 235 | 20223 | 4813 | 6.9 | <45 | <1.4 | <3.3 | 41 | 9.1 | <0.4 | <0.4 | <2.4 | 17 | 1.2 | <0.5 | 1.0 | <0.1 |
| | | L19 | 6.4 | 47 | 259 | 21824 | 6640 | 23 | <61 | <2.1* | <4.4* | 49 | 13 | <0.5 | <0.5 | <3.4 | 15 | <0.7 | <0.7 | 2.8 | <0.1 |
| | | L17 | 6.4 | 52 | 183 | 21205 | 6554 | <4.9 | <54 | <1.7 | <3.8 | 58 | 4.1 | <0.5 | <0.5 | <2.9 | 13 | <0.7 | <0.6 | 2.6 | <0.1 |
| | | L18 | 8.2 | 28 | 256 | 27045 | 8799 | 7.1 | <48 | <1.6 | 15 | 66 | 14 | <0.4 | <0.4 | <2.6 | 15 | <0.6 | <0.5 | 1.7 | <0.1 |
| | | L16 | 6.4 | 22 | 187 | 21363 | 6286 | <5.5 | <62 | <2.1 | <4.4 | 55 | 10 | <0.7 | <0.6 | <3.4 | 17 | 2.0 | <0.7 | <0.1 | <0.1 |
| | | L15 | 5.9 | 19 | 179 | 19612 | 5853 | 18 | <50 | <1.6 | <3.4 | 55 | 10 | <0.5 | <0.5 | <2.7 | 13 | 0.7 | <0.6 | 1.1 | <0.1 |
| | Avg. | | 6.5 | 30 | 217 | 21879 | 6491 | 14 | <53 | <1.8 | 15 | 54 | 10 | <0.5 | <0.5 | <2.9 | 15 | 1.3 | <0.6 | 1.8 | <0.1 |
| | SD. | | 0.9 | 15 | 38 | 2657 | 1313 | 7.8 | | | | 8.3 | 3.5 | | | | 1.8 | 0.7 | | 0.8 | |
| | **A8** | La3 | 5.0 | <14 | 173 | 14667 | 8374 | <8.3* | <92* | 333024 | <6.5* | 34 | 9.1 | <0.8 | 1166 | <4.7 | 10 | <1.3* | <1.0 | 28 | <0.1 |
| | | La1 | 4.6 | <12 | 169 | 11976 | 10543 | <7.2* | <79 | 123608 | <5.6 | 37 | 26 | <0.6* | 408 | <4.3 | 9.2 | <1.0* | <0.9 | 14 | <0.1 |
| | | La2 | 5.3 | 29 | 160 | 14957 | 10224 | 40 | <71 | 117504 | <4.9 | 33 | 8.8 | <0.6 | 314 | <3.7 | 11 | 3.0 | <0.8 | 5.4 | <0.1 |
| | Avg. | | 5.0 | 29 | 167 | 13867 | 9714 | 40 | <81 | 191379 | <5.7 | 35 | 15 | <0.7 | 629 | <4.2 | 10 | 3.0 | <0.9 | 16 | <0.1 |
| | SD. | | 0.4 | | 7 | 1644 | 1171 | | | 122706 | | 2.1 | 10 | | 467 | | 0.9 | | | 11 | |
| | **A9** | L28 | 5.3 | 40 | 141 | 17966 | 5106 | <3.0 | <33 | <1.1 | <2.3 | 36 | 10 | <0.3 | <0.3 | <1.8 | 11 | <0.4 | 1.5 | <0.1 | <0.1 |
| | | L27 | 5.0 | <10 | 144 | 16947 | 4497 | <6.2 | <71 | <2.3 | <4.8 | 31 | 13 | <0.7 | <0.7 | <3.7 | 10 | <0.9 | <0.9 | <0.2 | <0.1 |
| | | L26 | 5.9 | 21 | 203 | 20088 | 5042 | 15 | <47 | <1.6 | <3.2* | 35 | 12 | <0.4 | <0.4* | <2.5 | 14 | <0.6 | <0.6 | 5.6 | <0.1 |
| | | L23 | 6.2 | 22 | 191 | 21142 | 5525 | 23 | <64 | <2.2 | <4.5 | 39 | 13 | <0.6 | <0.6 | <3.4 | 18 | <0.9 | <0.8 | 0.5 | <0.1 |
| | Avg. | | 5.6 | 28 | 169 | 19036 | 5042 | 19 | <51 | <1.8 | <3.7 | 35 | 12 | <0.5 | <0.5 | <2.9 | 13 | <0.7 | 1.5 | 3.0 | <0.1 |
| | SD. | | 0.5 | 11 | 32 | 1919 | 422 | 5.8 | | | | 3.6 | 1.5 | | | | 3.5 | | | 3.6 | |

(Cont.)

| Sample Name | FIA | FI No. | Salinity (wt.% ) | Li | B | Na | K | Mn | Fe | Cu | Zn | Rb | Sr | Mo | Ag | Te | Cs | Ba | Au | Pb | Bi |
|---|---|---|---|---|---|---|---|---|---|---|---|---|---|---|---|---|---|---|---|---|---|
| **DH-505-8** | **A10** | L37 | 4.8 | 21 | 150 | 15353 | 6004 | <5.3 | <57* | <1.9 | <4.0 | 32 | 10 | <0.4* | <0.5 | <3.0 | 11 | <0.6 | <0.7 | 0.4 | <0.1 |
| | | L38 | 5.1 | <11 | 138 | 16558 | 6228 | <7.0* | <77 | <2.6 | <5.1 | 29 | 10 | <0.6 | <0.6 | <4.0 | 11 | <1.0 | <0.9 | 0.4 | <0.1 |
| | | L22 | 4.3 | <12 | 172 | 11986 | 8117 | <7.1 | <80* | <2.9 | <5.7* | 30 | 8.9 | <0.7* | <0.7* | <4.5* | 10 | 3.2 | <1.0* | <0.19 | <0.1 |
| | Avg. | | 4.7 | 21 | 153 | 14632 | 6783 | <6.5 | <71 | <2.5 | <4.9 | 30 | 10 | <0.6 | <0.6 | <3.8 | 11 | 3.2 | <0.9 | 0.4 | <0.1 |
| | SD. | | 0.4 | | 18 | 2370 | 1160 | | | | | 1.5 | 0.7 | | | | 0.7 | | | 0.0 | |
| | **A11** | L33 | 5.9 | 72 | 251 | 21121 | 3286 | <2.9 | <33 | <1.1 | <2.2 | 21 | 4.2 | <0.3 | <0.3 | <1.8 | 9.1 | <0.5 | <0.4 | <0.1 | <0.1 |
| | **A12** | L31 | 6.5 | <10 | 169 | 22913 | 4787 | 24 | <64* | <2.0 | <4.1 | 34 | 9.1 | <0.5 | <0.6 | <3.3 | 13 | 2.8 | <0.8 | 1.2 | <0.1 |
| | **A13** | L4 | 5.7 | <20 | 357 | 19377 | 5047 | <12 | <139 | <4.5* | <10* | 36 | 21 | <1.3 | <1.2 | <7.3 | 27 | <1.9 | <1.6 | <0.3 | <0.2 |
| | **A14** | L43 | 5.5 | 23 | 164 | 18603 | 5227 | 8.6 | <45 | <1.5 | <3.2 | 46 | 11 | <0.4 | <0.4 | <2.5 | 14 | 0.9 | <0.5 | 1.0 | <0.1 |
| | **A15** | L47 | 5.1 | 74 | 145 | 17100 | 5307 | <8.3 | <95 | <3.4 | <6.8 | 41 | 13 | <0.9* | <0.8* | <5.3 | 11 | <1.2* | <1.1 | <0.2* | <0.1 |
| **470-F7-13A** | **B1** | L29 | 9.4 | 34 | 101 | 33044 | 6961 | 44 | <77 | <2.4 | 17 | 25 | 22 | <0.6 | <0.6 | <3.4 | 6.7 | 2.5 | <0.4 | 12 | <0.1 |
| | | L26 | 8.5 | 26 | 101 | 27432 | 10283 | <5.0 | <45 | 179 | 11 | 34 | 31 | <0.3 | <0.4* | <2.0 | 4.8 | 3.9 | <0.3 | 22 | <0.1* |
| | | L27 | 8.7 | 21 | 72 | 30351 | 6322 | <6.4 | <57 | <1.8 | 15 | 22 | 21 | <0.4 | <0.5 | <2.5 | 3.6 | 1.6 | <0.3 | 17 | <0.1 |
| | | L23 | 11 | 43 | 244 | 34666 | 15910 | <8.6 | <74* | <2.2 | 10 | 33 | 56 | <0.4 | <0.5 | <3.3 | 3.8 | 1.2 | <0.4 | 35 | <0.1 |
| | Avg. | | 9.5 | 31 | 130 | 31373 | 9869 | 44 | <63 | 179 | 13 | 28 | 33 | <0.4 | <0.5 | <2.8 | 4.7 | 2.3 | <0.4 | 22 | <0.1 |
| | SD. | | 1.2 | 9.6 | 77 | 3173 | 4386 | | | | 3.1 | 5.7 | 16 | | | | 1.4 | 1.2 | | 9.8 | |
| | **B2** | L4 | 8.5 | 52 | 456 | 26888 | 11208 | <6.0 | <53 | <1.6 | 31 | 55 | 27 | <0.3 | <0.4 | <2.3 | 11 | 1.2 | <0.3 | 31 | <0.1 |
| | | L16 | 8.8 | 44 | 433 | 27492 | 12254 | <15 | <138 | <4.1 | 24 | 52 | 26 | <1.0 | <1.0 | <6.0 | 11 | 5.9 | <0.8 | 25 | <0.2 |
| | | L14 | 9.1 | 45 | 404 | 27556 | 14220 | <14 | <123 | <3.5 | 29 | 51 | 13 | <0.9 | <0.9 | <5.3 | 13 | <1.5 | <0.7 | 29 | <0.2 |
| | | L15 | 9.9 | 47 | 406 | 31497 | 12603 | <17 | <151 | <4.6 | 35 | 51 | 18 | <0.6 | <1.2 | <6.7 | 12 | 4.4 | <0.8 | 32 | <0.2 |
| | | L6 | 9.4 | 32 | 722 | 30927 | 10561 | <9.7 | <86 | <2.6 | 115 | 50 | 56 | <0.5 | <0.7 | <3.8 | 17 | 6.2 | <0.5 | 38 | <0.1 |
| | | L7 | 9.6 | 35 | 977 | 31545 | 10513 | 19 | <63 | <1.9 | 81 | 56 | 86 | <0.4 | <0.5 | <2.7 | 20 | 8.3 | <0.3 | 47 | <0.1 |
| | | L17 | 10 | 51 | 293 | 32569 | 13723 | <7.9 | <73 | <2.1 | 46 | 35 | 41 | <0.5 | <0.6 | <3.0 | 6.3 | 1.1 | <0.4 | 71 | <0.1 |
| | Avg. | | 9.4 | 44 | 527 | 29782 | 12155 | 19 | <98 | <2.9 | 52 | 50 | 38 | <0.6 | <0.8 | <4.3 | 13 | 4.5 | <0.5 | 39 | <0.1 |
| | SD. | | 0.6 | 7.5 | 238 | 2370 | 1476 | | | | 34 | 6.8 | 25 | | | | 4.5 | 2.9 | | 16 | |
| | **B3** | L21 | 7.7 | 38 | 149 | 24203 | 10355 | 24 | <60 | <1.9 | 21 | 36 | 20 | <0.3 | <0.4 | <2.6 | 7.8 | 3.1 | <0.3 | 19 | <0.1* |

(Cont.)

| Sample Name | FIA | FI No. | Salinity (wt%) | Li | B | Na | K | Mn | Fe | Cu | Zn | Rb | Sr | Mo | Ag | Te | Cs | Ba | Au | Pb | Bi |
|---|---|---|---|---|---|---|---|---|---|---|---|---|---|---|---|---|---|---|---|---|---|
| **470-F7-13D** | **C1** | L1 | 11 | 50 | 380 | 33475 | 16998 | <5.7 | <51 | <1.3 | 85 | 55 | 64 | <0.3 | <0.4 | <2.1 | 6.4 | 3.1 | <0.3 | 118 | <0.1 |
| | | L2 | 11 | 39 | 371 | 33989 | 13248 | <3.7 | <34 | <0.9 | 35 | 55 | 88 | <0.2 | <0.3 | <1.4 | 7.1 | 17 | <0.2* | 63 | <0.1 |
| | | L31 | 11 | 46 | 386 | 36542 | 12720 | 33 | <66 | <1.7 | 28 | 52 | 103 | <0.3 | <0.5 | <3.0 | 7.0 | 14 | <0.4* | 53 | <0.1 |
| | | L3 | 11 | 47 | 437 | 33942 | 15268 | <5.8 | <52 | <1.4* | 99 | 53 | 67 | <0.2 | <0.4* | <2.3 | 7.0 | 1.4 | <0.3 | 119 | <0.1 |
| | | L4 | 11 | 47 | 303 | 33302 | 14416 | <6.3 | <56 | <1.6 | 52 | 48 | 58 | <0.4 | <0.5 | <2.4 | 5.6 | 4.0 | <0.3 | 100 | <0.1 |
| | | L5 | 11 | 51 | 342 | 35659 | 15159 | 17 | <66 | <1.7 | 47 | 47 | 58 | <0.4 | <0.5 | <2.7 | 5.6 | 8.1 | <0.4 | 89 | <0.1 |
| | Avg. | | 11 | 47 | 370 | 34485 | 14635 | 25 | | | 58 | 52 | 73 | | | | 6.5 | 7.9 | | 90 | |
| | SD. | | 0.3 | 4.1 | 45 | 1309 | 1543 | 12 | | | 28 | 3.4 | 18 | | | | 0.7 | 6.3 | | 28 | |
| | **C2** | L10 | 11 | 49 | 384 | 36044 | 12631 | 29 | <49* | <1.3 | 43 | 66 | 57 | <0.3 | <0.4 | <2.1 | 12 | 1.5 | <0.3 | 256 | <0.1 |
| | | L32 | 11 | 50 | 369 | 36953 | 13895 | 29 | <45 | <1.2 | 51 | 75 | 83 | <0.2 | <0.3 | <2.0 | 9.8 | 12 | <0.2 | 157 | <0.1 |
| | | L8 | 10 | 33 | 342 | 31792 | 10094 | <4.9* | 104 | <1.1* | 32 | 60 | 65 | <0.2 | <0.3 | <1.8 | 8.9 | 22 | <0.2* | 164 | <0.1 |
| | | L9 | 9 | 37 | 281 | 28892 | 11948 | <5.2* | <46 | <1.1 | 29 | 49 | 100 | <0.3 | <0.3 | <2.0 | 5.3 | 4.5 | <0.3 | 36 | <0.1 |
| | | L33 | 9 | 39 | 308 | 27467 | 10223 | <4.8* | <43 | <1.1 | 25 | 49 | 79 | <0.3 | <0.3 | <1.9 | 5.3 | 9.0 | <0.2 | 47 | <0.1 |
| | | L6 | 11 | 51 | 319 | 35201 | 14064 | <3.4* | <31* | 6.4 | 57 | 46 | 77 | <0.2* | <0.2* | <1.3 | 5.3 | 12 | <0.2 | 142 | <0.1 |
| | | L7 | 10 | 47 | 356 | 31351 | 13855 | 26 | <70 | <1.8 | 37 | 63 | 69 | <0.5 | <0.6 | <3.0 | 6.7 | 6.0 | <0.4 | 40 | <0.1 |
| | Avg. | | 10 | 44 | 337 | 32528 | 12387 | 28 | 104 | 6.4 | 39 | 58 | 76 | | | | 7.6 | 9.5 | | 120 | |
| | SD. | | 1.1 | 7.4 | 36 | 3648 | 1705 | 1 | | | 12 | 11 | 14 | | | | 2.6 | 6.7 | | 83 | |
| | **C3** | L21 | 11 | 45 | 370 | 35711 | 14133 | <5.0 | <45 | <1.0 | 43 | 48 | 69 | <0.3 | <03 | <2.0 | 5.3 | 6.4 | <0.3 | 110 | <0.1 |
| | | L24 | 11 | 55 | 379 | 35807 | 15843 | <5.3* | <46 | <1.1 | 36 | 48 | 57 | <0.3 | <0.3 | <2.0 | 5.6 | 5.0 | <0.3 | 94 | <0.1 |
| | | L19 | 11 | 50 | 321 | 33834 | 14516 | <7.7 | <68 | <1.7 | 59 | 45 | 59 | <0.4 | <0.6 | <2.9 | 6.1 | 6.1 | <0.4 | 105 | <0.1 |
| | | L20 | 11 | 44 | 309 | 33638 | 13845 | <4.3 | <38 | <1.0* | 56 | 41 | 61 | <0.2 | <0.3 | <1.7 | 5.0 | 5.2 | <0.2 | 114 | <0.1 |
| | | L23 | 11 | 53 | 328 | 34266 | 16590 | 34 | <117 | <2.9 | 55 | 55 | 60 | <0.5 | <0.8 | <5.1 | 6.2 | 8.5 | <0.7 | 99 | <0.1 |
| | Avg. | | 11 | 49 | 341 | 34651 | 14985 | 34 | | | 50 | 47 | 61 | | | | 5.6 | 6.3 | | 104 | |
| | SD. | | 0.3 | 4.9 | 31 | 1037 | 1179 | | | | 9.8 | 5.3 | 4.8 | | | | 0.5 | 1.4 | | 8.0 | |

(Cont.)

| Sample Name | FIA | FI No. | Salinity (wt%) | Li | B | Na | K | Mn | Fe | Cu | Zn | Rb | Sr | Mo | Ag | Te | Cs | Ba | Au | Pb | Bi |
|---|---|---|---|---|---|---|---|---|---|---|---|---|---|---|---|---|---|---|---|---|---|
| **470-F7-13D** | **C4** | L12 | 12 | 45 | 234 | 37556 | 13805 | <6.4 | <58 | <1.5 | 32 | 50 | 44 | <0.4 | <0.4* | <2.5 | 8.0 | <0.7 | <0.3 | 49 | <0.1 |
| | | L13 | 12 | 52 | 304 | 37237 | 16221 | <9.1* | <82 | <1.9 | 35 | 58 | 56 | <0.3* | <0.6 | <3.4 | 5.9 | <0.9 | <0.5 | 159 | <0.1 |
| | | L14 | 11 | 52 | 325 | 36841 | 13148 | <7.5 | <69 | <1.7 | 40 | 44 | 41 | <0.3 | <0.5 | <2.8 | 4.9 | 2.2 | <0.4 | 100 | <0.1 |
| | Avg. | | 12 | 49 | 288 | 37211 | 14391 | | | | 35 | 51 | 47 | | | | 6.3 | 2.2 | | 103 | |
| | SD. | | 0.3 | 3.9 | 48 | 358 | 1618 | | | | 4.0 | 7.3 | 8.2 | | | | 1.6 | | | 55 | |
| | **C5** | L25 | 10 | 41 | 314 | 33877 | 12501 | <6.3* | <57* | <1.4 | 47 | 67 | 73 | <0.3 | <0.4 | <2.4 | 8.1 | 8.2 | <0.3 | 126 | <0.1 |
| | | L26 | 11 | 56 | 328 | 35645 | 13308 | 23 | <71 | <1.7 | 57 | 60 | 72 | <0.4 | <0.5 | <3.1 | 5.8 | 3.1 | <0.4 | 75 | <0.1 |
| | Avg. | | 11 | 49 | 321 | 34761 | 12905 | 23 | | | 52 | 64 | 72 | | | | 7.0 | 5.7 | | 100 | |
| | SD. | | 0.4 | 10 | 9.4 | 1250 | 570 | | | | 7.1 | 4.8 | 0.1 | | | | 1.6 | 3.6 | | 37 | |
| | **C6** | L11 | 11 | 57 | 339 | 34265 | 16592 | <3.6 | <32* | <0.8 | 38 | 50 | 60 | <0.1 | <0.2* | <1.4 | 5.4 | 6.7 | <0.2 | 88 | <0.1 |

*Calculated element concentrations are above the detection limit originally, but these values have errors >50% and without visible peak in the time-resolved ICP-MS signals, and therefore are considered as artifacts. Abbreviations: FIA = fluid inclusion assemblages, FI No. = fluid inclusions numbers, Avg. = average, SD = standard deviations.